MULTI-SCALE SELF-ASSEMBLY OF NANOENERGETIC MATERIALS UTILIZING FUNCTIONALIZED GRAPHENE

A dissertation presented to the Faculty of the Graduate School
University of Missouri
In Partial Fulfillment
Of the requirements of the Degree
Doctor of Philosophy in Biological Engineering

By
ANQI WANG

Dissertation Supervisor
Dr. Shubhra Gangopadhyay
Dr. Matthew R. Maschmann
Dr. Jacob A. McFarland

MAY 2020

The undersigned, appointed by the Dean of the Graduated School, have examined the dissertation entitled

MULTI-SCALE SELF-ASSEMBLY OF NANOENERGETIC
MATERIALS UTILIZING FUNCTIONALIZED GRAPHENE

Presented by Anqi Wang

A candidate for the degree of Doctor of Philosophy

And hereby certify that in their opinion it is worthy of acceptance

Dr. Shubhra Gangopadhyay (Co-Advisor)
Department of Biomedical, Biological and Chemical Engineering
Department of Electrical and Computer Engineering

Dr. Matthew Maschmann (Co-Advisor)
Department of Biomedical, Biological and Chemical Engineering
Department of Mechanical and Aerospace Engineering

Dr. Jacob McFarland (Co-Advisor)
Department of Mechanical and Aerospace Engineering

Dr. Sheila Grant
Department of Biomedical, Biological and Chemical Engineering

Dr. Zheng Yan
Department of Biomedical, Biological and Chemical Engineering
Department of Mechanical and Aerospace Engineering

ACKNOWLEDGEMENTS

It would not be possible for me to finish this dissertation without the guidance and help from all the people who contributed their assistance and expertise to the research of this project and their care to me.

First, I would like to thank my primary advisors, Dr. Shubhra and Keshab Gangopadhyay, for accepting me as a PhD student in their research group, bringing me to a new world of science and gave me all-around guidance in my studies, research and life. During my PhD years in this research group, their research profession, academic integrity, scientific insight and energetic working attitude taught me a lot. They provided me an outstanding environment of research where I can work both independently and collaboratively. They set a role model for me in research, work, and, more importantly, code of conduct in my future life. Although they are usually not physically in town, they still gave me numerous suggestions in science, research methods and daily life via phone or Internet. Every single time I was facing a problem in my research, their suggestions always hit the nail on the head and solved my confusion. Under the guidance of Dr. Shubhra and Dr. Keshab Gangopadhyay, I have matured as a scientist, an engineer, a problem-solver, and most importantly, as a good person. I cannot be more grateful for their mentorship.

I would like to thank my co-advisors, Dr. Matthew Maschmann and Dr. Jacob McFarland, for guiding me like their own graduate students. Since Dr. Shubhra is usually not physically in town, Dr. Maschmann and Dr. Jacob are always the professors I recalled when I figured out some problems or new ideas and wanted to have a talk with. It is my privilege to work with two such splendid young professor from mechanical engineering, which is a completely new field for me. They brought me into a new world more than just

materials and chemistry. It made me so excited to be involved in cross-field in the frontier of material science, physics, chemistry and mechanical engineering. I not only learned about the science and ideas I never noticed before, but also experienced the different research tools, methodologies, as well as concepts and communications in a different research direction. They gave me extremely significant guidance in both my research and my life. I feel highly fortunate to have had Dr. Matthew Maschmann and Dr. Jacob McFarland as my co-advisors.

I would like to express my gratitude to my committee members, Dr. Shiela Grant and Dr. Yan Zheng for their efforts in providing helpful feedback for all my research.

I would like to thank all my colleagues, and friends, in the Gangopadhyay research group, the Maschmann research group and the McFarland research group. Thank you all for your critical support and for making my PhD years so memorable. I would like to acknowledge Dr. Joseph Mathai, Dr. Charles Darr and Dr. Syed Barizuddin for their significant help during my research. I would like to thank Dr. Rajagopalan Thiruvengadathan for always giving me advices through Internet. I would like to thank Dr. Sangho Bok for giving me a lot of suggestions in experiment and research. I would like to thank Dr. Clay Staley for inspiring me to come to this new world of research. I would like to thank Mr. Naadaa Zakiyyan, Dr. Biyan Chen, Mr. Brandon Smith, Mr. Matthew Riehn, Mr. Andrew Countryman and Mr. Calvin Young for the research time we spent and the discussions we had together. My research would not have been possible without your support.

I would also like to thank the funding agencies and collaborating groups that have supported and helped my research. These include: The Air Force Office of Scientific

Research, The Army Research Office, Dr. Michael Zachariah's research group from University of Maryland / University of California, Riverside.

I would like to express my highest gratitude to my family and friends for their love and support. Most importantly I need to thank my parents, Mr. Xichun Wang and Ms. Caiying Wang, for giving me birth, providing me with every opportunity during my growth and the possibility to success. There is simply no way for me to fully quantify your love and contribution to me, and how much I appreciate and feel grateful to you. I would like to thank my parents-in-law, Mr. Yonghua Zhao and Mrs. Yuping Yan, for embracing me as a son and for their meticulous care and support during my years in the United States. Last but new least, I would like to especially thank Yan Zhao, my newlywed wife, for standing by and always support me in nearly the past decade with extreme patience and concern. I will not be able to accomplish anything, including this work, without any of you.

TABLE OF CONTENTS

LIST OF FIGURES

LIST OF TABLES

ABBREVIATIONS

DLS	Dynamic light scattering
DSC	Differential scanning calorimetry
EDS	Energy-dispersive X-ray spectroscopy
FTIR	Fourier-transform infrared spectroscopy
MS	Mass spectrometry
SEM	Scanning electron microscopy
TEM	Transmission electron microscopy
TGA	Thermogravimetric analysis
XRD	X-ray diffraction
ESD	Electrostatic discharge
GO	Graphene oxide
FG	Fluorinated graphene
FGO	Fluorinated graphene oxide
rGO	Reduced graphene oxide
F-rGO	Fluorinated reduced graphene oxide
I-rGO	Iodinated reduced graphene oxide
DMF	N,N-Dimethylformamide
IPA	Isopropanol / Isopropyl alcohol
PC	Propylene carbonate
THF	Tetrahydrofuran

ER	Equivalence ratio
NP	Nanoparticle

ABSTRACT

The work described here-in focuses on the synthesis and characterization of novel nanoenergetic materials and is driven by overcoming the disadvantages of traditional nanoenergetic composites, improving the energetic performance as well as discovering the science boundary of nanoenergetic materials. Micro-scale and macro-scale structured energetic composites were synthesized via self-assembly process between Al nanoparticles, metal oxide nanoparticles and functionalized graphene.

A novel gelation process of reduced graphene oxide was developed and utilized for self-assembling Al and Bi_2O_3 into macroscale structures with enhanced energetic performance and handling safety. The process successfully reduced graphene oxide sheets into rGO, forming a 3D structure with high porosity, controllable density, size, shape and chemical composition. The phase separation between Al and Bi_2O_3 was minimized, and the energetic reactivity of both nanoparticles was retained. Therefore, the final product rGO/Al/Bi_2O_3 exhibited 25% increase in energetic release during equilibrium reaction. A more than 100% increase in combustion rate was observed due to the unique self-confining structure. The conductive rGO scaffold offered the product a better safety for handling by increasing the ignition threshold to electrostatic discharge by 4 orders.

Halogenated graphene was also adopted as the additive for self-assembly with Al and Bi_2O_3 nanoparticles for micro-scale energetic composites. A fluorine, oxygen co-functionalized graphene (FGO) was synthesized via a gas – solid XeF_2 – GO reaction. The stability of this material upon storage time, temperature and dispersing was examined, confirming both stable and unstable fluorine groups contained in its structure. After mixing with Al and Bi_2O_3 nanoparticles, the FGO/Al/Bi_2O_3 showed a 60% enhancement in energy

release and an all-solid-state reaction between Al and Bi_2O_3 as the fluorine significantly weakened the alumina shell protecting Al core.

Iodinated reduced graphene oxide (I-rGO) was also prepared to fabricate micro-scale self-assembled I-rGO/Al/Bi_2O_3. The I-rGO was synthesized by graphene oxide paper and hydroiodic acid, containing both chemically bonded single iodine atoms and intercalated polyiodide clusters between graphene layers. The loss of iodine contents, especially polyiodide clusters, from the structure upon heating, solvent effect and exfoliation was examined. After self-assembly with Al and Bi_2O_3 nanoparticles, the released iodine weakened the alumina shell by forming Al-O-I bond on it, reducing the reaction temperature and enhancing the energy release significantly. The conductive I-rGO also increased the threshold to electrostatic discharge of final I-rGO/Al/Bi_2O_3 by 4 orders, ensuring the safety during handling the material in large quantity.

Chapter 1

Introduction

1.1. Introduction to nanoenergetic materials

Human beings have been using energetic material for more than one thousand years. No later than the 9th century, ancient Chinese alchemists discovered black powder, which was initially expected to be an elixir, but turned out to be a ubiquitous energetic material. [1] This prototype of energetic material was composed of fuel (charcoal and carbon) and oxidizer (sulfur and potassium nitrate KNO_3). During the energetic reaction of black powder shown as equation 1.1,

$$2KNO_3(s) + S(s) + 3C(s) \rightarrow K_2S\,(s) + N_2(g) + 3CO_2(g) \qquad (1.1)$$

The black powder reaction releases a significant theoretical energy of 2217 J/g along with the formation of a large amount of gas, generating significant heat and pressure.

Along with the discovery of materials and development of science, people learned much more about energetic materials and the reaction mechanisms of these materials. Energetic materials are defined as a material that stores a high amount of chemical energy, which can be released into heat or pressure during its chemical reaction. [2] Energetic materials are now mostly categorized into three different types, explosives, pyrotechnics, and propellants. [3] Energetic materials have been widely used in both military, industrial and civil fields, such as weapons, space, construction and demolition industries, mining, and fireworks. [2-5] Energetic materials have vastly attracted researchers' and engineers' interest in the past decades to improve its energetic performance and broaden its application in different fields. Researchers have been targeting engineered energetic materials for the best combination of higher performance but enhanced insensitivity to external shock and thermal insults. [2]

Energetic materials can consist of different elements and formulas. [5, 6] One of the major classes of energetic materials is a heterogeneous mixture of reductive fuel with organic or inorganic oxidizer, which is known as thermite material. These materials produce self-propagating exothermic reactions with adiabatic flame temperatures in excess of 3000 K. [7-9] Various elements can be utilized as the fuel in thermite composites, including boron [10, 11], silicon [12], magnesium [13], and aluminum [8, 14]. Among all different fuel elements, aluminum attracted most researchers' attention because of its high energy release of 31 kJ / g during oxidation reaction as shown in equation 1.2 [15],

$$4Al(s) + 3O_2(g) \rightarrow 2Al_2O_3(s) \qquad \Delta H = -3351.4\ kJ/mol \qquad (1.2)$$

Al is also abundant in earth [16] and good stability in atmosphere, when passivated [17]. Different kinds of oxidizers can be coupled with aluminum to trigger the energetic reaction. The most commonly used oxidizer is metal oxide, such as CuO [18, 19], Fe_2O_3 [20, 21], Bi_2O_3 [22, 23], and MoO_3 [24, 25]. Halogen oxidizers, especially iodine oxide [26, 27] and fluorine-rich polymers, such as polytetrafluoroethylene (PTFE / Teflon) [28, 29], THV [30], PVDF [31], can also be adopted as the oxidizer in nanothermite composite.

Researchers have identified multiple parameters that alter the energetic performance of the synthesized thermite material, including equivalence ratio [19, 32, 33], bulk packing density [34, 35], morphology and arrangement of fuel and oxidizer [8, 36, 37]. Additionally, researchers found that the size of fuel and oxidizer particles dramatically changed the energetic behavior of thermite material. [38-40] Thermite material consists of nano-sized fuel and oxidizer particles, named nanothermites, exhibited significantly enhanced energetic performance such as reduced ignition temperature [40, 41], lowered activation energy [42], and much higher combustion propagation velocity [38, 43], as shown in Figure 1.1. Compared to traditional thermite consisted of particles in micron or even larger size, nanothermite exhibited its outstanding reactivity due to its unique surface effect of nanoparticles. [44] The significantly increased surface-to-volume ratio enables the reaction to take place in much more interfacial contact area and decreased diffusion length between constituents, leading to its extremely high reaction speed. [45] Energetic nanocomposites further enhanced the capability to tune one or more physical, chemical, or mechanical attributes of nanoenergetic materials and enabled the design and applications of microscale multifunctional combustion systems [6, 39], including applications in MEMS [3] and microchips [46].

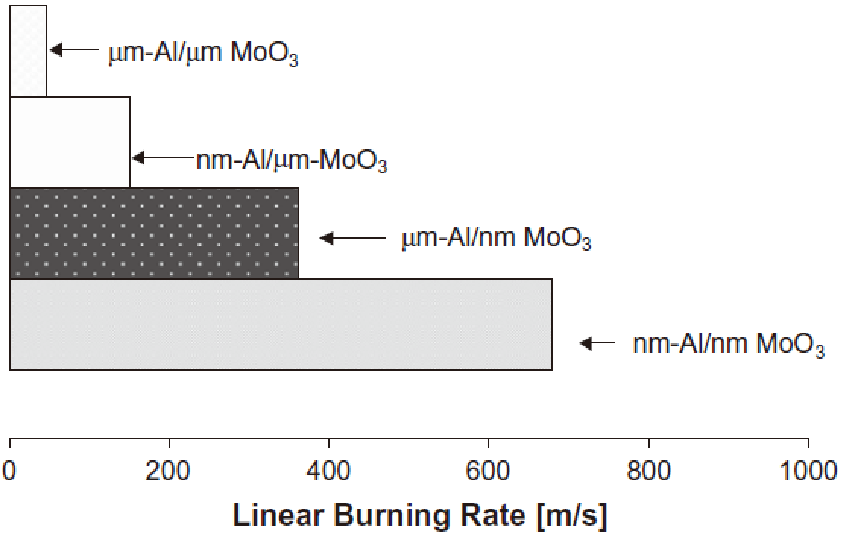

Figure 1.1 Linear combustion rate of Al/MoO_3 thermite with different particle sizes. Reprinted from Weismiller et al. [38] with permission of Elsevier.

However, despite the promising attributes of nanosized thermite material, there are also significant challenges to address prior to their application. For instance, the theoretical exothermic enthalpy change of Al/Bi_2O_3 nanothermite is 2115 J/g [28], as shown in equation 1.3,

$$2Al(s) + Bi_2O_3(s) \rightarrow Al_2O_3(s) + 2Bi(s) \quad \Delta H = -1101.8\ kJ/mol \qquad (1.3)$$

while the real energy release was always found to be much lower, only around 700 ~ 800 J/g measured by DSC-TGA due to some limitations of traditional nanothermite system. [47] Generally, there are four major disadvantages that prevent the further improvement and wider application prospects of nanothermite, including phase separation between fuel and oxidizer nanoparticles, reactive sintering of Al nanoparticles, lack of scalability, and the spontaneously formed, inert alumina shell on the surface of Al nanoparticles.

Phase separation

The fuels and oxidizer used in thermites need to be well mixed to maximize their contact area and reaction rate. Traditionally, physical processing methods, such as ultrasonic mixing and arrested ball milling, produce nanothermites with a random distribution of oxidizer and fuel particles. [24, 48] The unstructured nature of mixing forms composites with unreliable and irreproducible combustion behavior. The optimum interfacial contact is realizable only if all the components are homogeneously mixed without any phase separation. [49]

Reactive sintering

Due to the phase separation discussed above, reactive sintering is considered to happen in the agglomerations of Al nanoparticles (NPs). During combustion, which is considered to be a rapid heating process, a reactive sintering mechanism involving condensed phase reaction occurs. [50] The fast sintering process results in the loss of nanoscale features of Al nanoparticles in a comparable time scale to the combustion reaction, as shown in Figure 1.2. [51] This loss of nanoscale features can significantly decrease the reaction rate between fuel and oxidizer due to the loss of reactive surface area, explaining why some nanoscale thermite materials don't show much better performance than microscale thermite materials in some experiments. [38]

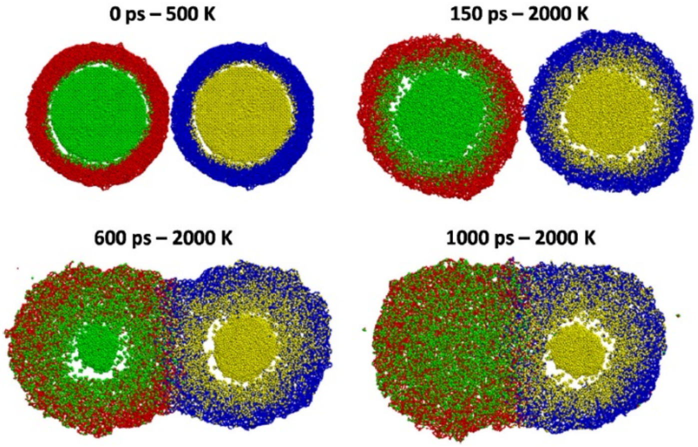

Figure 1.2 Reactive sintering causes neighboring Al nanoparticles to lose their nano-sized nature during rapid heating. Reprinted from Chakraborty et al. [51] with permission from Elsevier.

Lack of scalability

Scaling the nanothermite materials to macroscale safely without a significant loss of performance remains a challenge due to some practical difficulties. Nanothermites are generally sensitive to electrostatic discharge (ESD), impact, and friction, which complicates the scalable production of nanothermite materials to commercially relevant quantities. [52, 53] Traditional methods of creating macroscale structures involves forming nanothermites into pellets under high pressure, which is dangerous and results in reduced reaction kinetics. [23, 34, 40, 54] Chemical synthesis routes to form nanothermite materials in microstructures or macrostructures have required chemical surfactants such as PVP [55, 56] or will cause severe phase separation between fuel and oxidizer [57], both of which may reduce the energy release severely.

The spontaneously formed, inert alumina shell

Al nanoparticle is pyrophoric in ambient atmosphere. It has an amorphous inert Al_2O_3 passivation shell on the surface which protects the Al core from reacting with air. This normally 2-4 nm-thick Al_2O_3 shell, as shown in TEM pictures in Figure 1.3 [58], prevents the direct contact between active Al core and the external oxidizer. For micron size Al nanoparticles, the alumina shell may account for very low percentage of the total weight. However, for Al nanoparticles around or smaller than 100 nm, the Al_2O_3 shell may take more than 20% of total weight, which is a considerable large part of the particle. In normal nanothermites consist of Al nanoparticles and metal oxides, this layer of alumina shell, however, does not participate in the reaction release. This feature, on the positive side, provides a safe handling during synthesis; while on the negative side, sets a barrier to the direct rapid reaction and the heat sink during increasing temperature when energetic reaction needs to be realized.

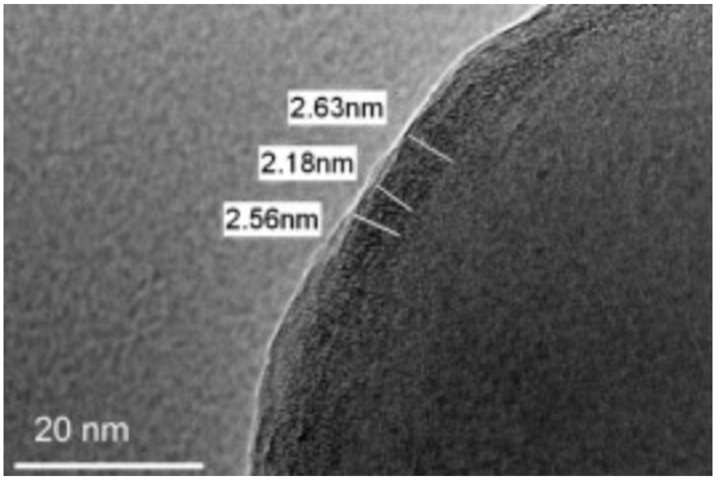

Figure 1.3 TEM picture of Al nanoparticles with a roughly 2.5-nm-thick alumina shell. Reprinted from Gesner et al. [58] with permission from Elsevier.

The existence of Al_2O_3 also makes the mechanism of nanothermite reaction complex. To initiate the reaction between Al and oxidizer, diffusion of Al core or oxidizer ion must happen through the alumina shell, or the shell is decomposed, phase changed or broken and direct contact between Al and oxidizer is enabled. In rapid-heating reaction, which is considered to be the real condition in nanothermite combustion, some changes must occur on the Al_2O_3 shell. Generally, there are two different proposed mechanisms for the combustion of nanothermites. Some researchers hypothesize the Al diffusion outward of the alumina shell, along with the occurrence of defection and phase change of alumina shell [59-61], while some other researchers agree with the melt-dispersion reaction mechanism in which the rapid increase of temperature led to the melting of Al that generates enough pressure to completely shatter the alumina shell and disperse small Al clusters. [62-64] The two mechanisms are depicted in Figure 1.4. There is currently no conclusion for combustion mechanisms of Al-based nanothermite, but it is certain that the presence of alumina shell decreases the reactivity of Al NPs and limits the energetic performance.

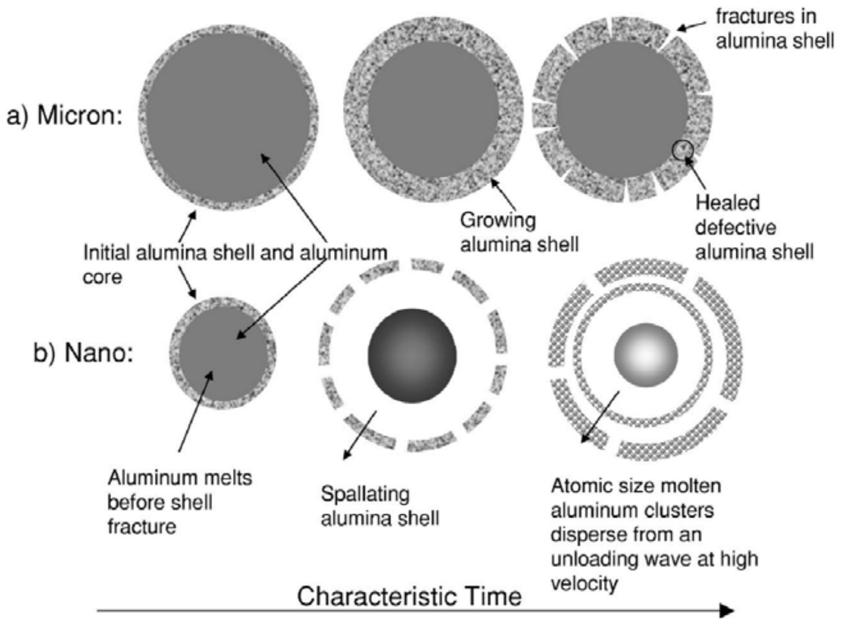

Figure 1.4 Schematic representations of the two major combustion mechanisms during the oxidation. Reprinted from Levitas et al. [65] with permission from AIP publication.

To overcome the disadvantages of conventional nanothermite system mentioned above, researchers have tried multiple synthesis methods and various composites to improve the performance of nanothermite material. However, these solutions mostly targeted one of those four problems and not capable to solve multiple of them at the same time. For example, surfactants, which can improve the dispersion of nanoparticles in solvents, such as PVP [55, 56], octadecyl-amine [66] and DNA [67] were applied to assist the dispersion of nanoparticles and reduce the phase separation. These extra molecules also prevented the direct surface contact between fuel and oxidizer nanoparticles and thus reduce the reaction rate. Fluoropolymers [29, 30] and iodine oxides / hydroxides [68] were considered to be promising oxidizers as halogen can etch the inert alumina shell prior to the main reaction with the Al core, leading to more complete energetic reactions. However, these materials still require solutions for phase separation and electrostatic sensitivity due to its poor electrical conductivity. Therefore, a need exists for synthesis mechanisms to realize ordered, safe, scalable and energetic Al-based nanoenergetic material.

1.2. Introduction to graphene and graphene oxide

Graphene, a flat monolayer of carbon atoms, has attracted significant attention in materials science since its discovery in 2004. [69, 70] Its unique two-dimensional honeycomb lattice [71] and perfect all sp^2-hybridized layered carbon structure [72] result in its distinctive physical and chemical characteristics, including an extremely high electrical conductivity along the direction of the lattice [73-75] and unique quantum Hall effect [76], mechanical properties such as its ultimate Young’s modulus (stiffness) of 1 TPa and tensile strength of 130 GPa [77], and optical properties such as its unexpectedly high opacity [78]. More importantly, the properties of graphene can be engineered by functionalizing graphene sheets with different chemical species depending on the synthesis method [79]. Additionally, the considerably high specific surface area of graphene [80, 81] and functionalized graphene [82] allows it to easily form composites with numerous different materials such as nanoparticles [83, 84] and polymers [85] with a high material loading. Therefore, these different functionalized graphene and graphene composites can be used for various applications such as reaction catalysis [86], hydrogen storage [87], fuels in energetic systems [88, 89] sensors [90], and electrical devices such as transistors, electrodes, and supercapacitors [91, 92].

Graphene oxide (GO) is a type of functionalized graphene usually synthesized from the oxidation of graphite powder using strong inorganic oxidizers such as $KMnO_4$ / H_2SO_4 and $KClO_4$ / HNO_3. [93] The graphite is first intercalated by acid ions, forming graphite intercalation compounds [94], and is then oxidized by the main oxidation agent, which supports final exfoliation of thin GO layers in solutions [95]. Compared to graphene, GO has many more defects and an abundance of oxygen functional groups, leading to higher surface energy [96], reactivity [97, 98], and much better dispersity in polar or protic suspension agents [99, 100], which has led to its use in many applications [97] as a standalone material [101, 102] or composites with other materials [103, 104]. Additionally, GO is used widely as the precursor for producing reduced graphene oxide (rGO) [105, 106] and alternative variants of functionalized graphene [107-109]. GO has also been found to be a good template for self-assembly with polymers and nanoparticles due to its capability of surface modification, considerably high surface area (>3000 m^2/g), high dispersity and abundant surface charge in dispersions (ζ potential ~ -30 mV in water). [110-112]

1.3. Previous work of self-assembled GO/Al/Bi_2O_3

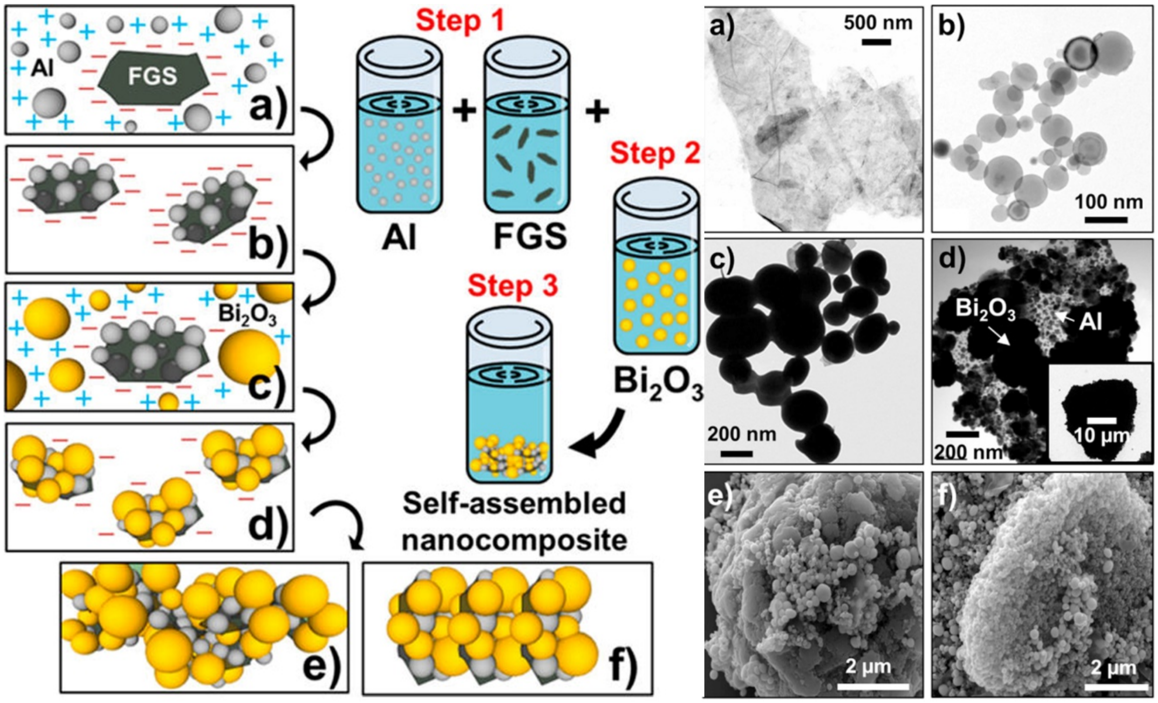

Figure 1.5 Self-assembly process (left), TEM (a-d) and SEM (e, f) pictures of the of GO/Al/Bi_2O_3. Reprinted with permission from [47]. Copyright 2014 American Chemical Society.

Earlier research in our group by Rajagopalan Thiruvengadathan et al. revealed that GO could serve as a template for self-assembly with Al and Bi_2O_3 nanoparticles. [47] The self-assembly process was driven by the electrostatic attraction, confirmed by zeta potential measurements, in which GO showed strong negative charge, while Al and Bi_2O_3 nanoparticles showed strong positive charge. As shown in Figure 1.5A, an ultra-dense, highly reactive GO/Al/Bi_2O_3 structure formed after the self-assembly. An ordered structure was formed as observed under electron microscope, as shown Figure 1.5 (right). The phase separation between Al and Bi_2O_3 nanoparticles was mitigated through the process to significantly shorten the diffusion length of the nanoparticles during. Therefore, the energetic properties were significantly enhanced compared to traditional randomly mixed Al/Bi_2O_3. The energy release increased by 92%, the peak pressure during combustion increased by 230%, the pressurization rate increased by 430% and the linear burning rate increased by 35%. [113] Therefore, self-assembly of energetic composites with the assistance of functionalized graphene holds significantly potential in dealing with the problems and improving the energetic performance of nanoenergetic materials.

1.4. Motivation of the project

The goal of this research is use graphene to synthesize different nanoenergetic structures from microscale to macroscale. Reaction mechanisms are also investigated to gain a better understanding on the driving physics of combustion for use in optimized energetic material design. Chemically functionalizing graphene with different elements allows surface property engineering to better support self-assembly with Al nanoparticles and oxidizers. The structure of the target nanoenergetic materials can also be well-controlled based on the structure of functionalized graphene and the self-assembly process. By utilizing functionalized graphene as additive in nanoenergetic material, the main disadvantages of traditional Al-based nanothermite systems can be overcome, and the energetic performance of the produced material can be improved.

1.5. Characterization methods

The advancement of nanomaterials over the past decade has been enabled by advancements in characterization methods. In this research, multiple characterization methods were used to evaluate the structure and energetic performance of all nanoenergetic composites prepared with functionalized graphene. Each method used will be briefly introduced below.

Fourier-Transform infrared Spectroscopy / Attenuated Total Reflectance (FTIR/ATR)

Fourier-transform infrared spectroscopy (FTIR) is one of the most important methods to determine the functional groups in materials. The vibrational energy states of chemical bonds are quantized; therefore, molecules absorb IR radiation at specific frequencies, which excites the chemical bond. The vibration of chemical bonds can be estimated by Born-Oppenheimer and harmonic approximations. Treating chemical bond vibrations as harmonic oscillation he wavenumber of the absorbance can be calculated by equation $\upsilon = \frac{1}{2\pi\mathrm{c}}\sqrt{\frac{\mathrm{k}}{\mu}} \quad \mu = \frac{\mathrm{m_A m_B}}{\mathrm{m_A + m_B}}$ (*1.4*),

$$\tilde{\upsilon} = \frac{1}{2\pi c}\sqrt{\frac{k}{\mu}} \qquad \mu = \frac{m_A m_B}{m_A + m_B} \qquad (1.4)$$

where *k* is the spring constant of the bond, *c* is the speed of light, and *μ* is the reduced mass of the two-atom system. Therefore, the absorption frequency of each different chemical bond in infrared spectroscopy can be determined. Generally, there are two regions interpreting in a spectrograph, including a functional group region (> 1500 $\mathrm{cm^{-1}}$) and a fingerprint region (< 1500 $\mathrm{cm^{-1}}$), which can be combined to analyze the structure of the material. [114]

Attenuated total reflectance (ATR) is a technique that used frequently in conjunction with infrared spectroscopy, enabling examining the samples directly without further preparation. It utilizes the total internal reflection of a beam of infrared light at the surface of the ATR crystal and the sample, resulting in an evanescent wave propagating into the sample, as shown in Figure 1.6. The beam is then collected when exiting the crystal by a detector. ATR has been widely used due to its accessibility, ease of use and non-destructive nature.

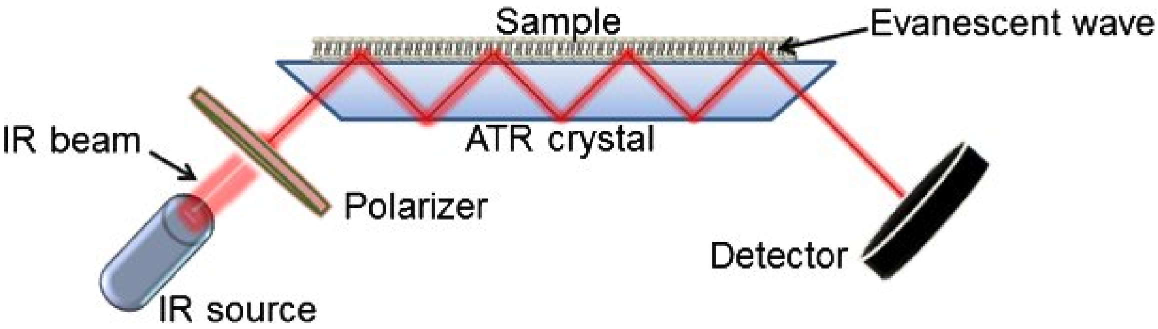

Figure 1.6 Schematic representation of an FTIR-ATR system. Reprinted from [115].

In this research, a Thermo Nicolet 4700 FT-IR Spectrometer was used for FTIR and ATR measurement. Self-standing sheets were measured directly in the instrument, while powdered materials were deposited on Si wafer for measurement. A germanium stage was used for ATR measurement.

Raman spectroscopy

Photons interact with molecules when a beam of light shines onto materials, resulting scattering of light. When the scattering is elastic, it is known as Rayleigh scattering, giving a scattering light at the same wavelength of the light source. When inelastic scattering occurs, the transfer of energy between photons and molecules causes the change of vibration state of molecule, resulting Raman scattering lights, which have two different wavelengths, named Stokes and anti-Stokes scattering and centered on Rayleigh scattering, as shown in Figure 1.7. By detecting the Raman shift of the scattered light, a spectrograph can be obtained for analyzing the structure of the material.

Usually, the molecules which are non-centrosymmetric are both FTIR and Raman active. In the molecules which are centrosymmetric, their different vibration modes show exclusive FTIR or Raman activity. Therefore, Raman and FTIR measurements are usually combined to better understand the composition and chemical bonds of the target material.

In this research, a Renishaw inVia Raman microscope coupling with a 633 nm laser source was used for Raman spectroscopy. Samples were placed or deposited on Si wafer for measurement.

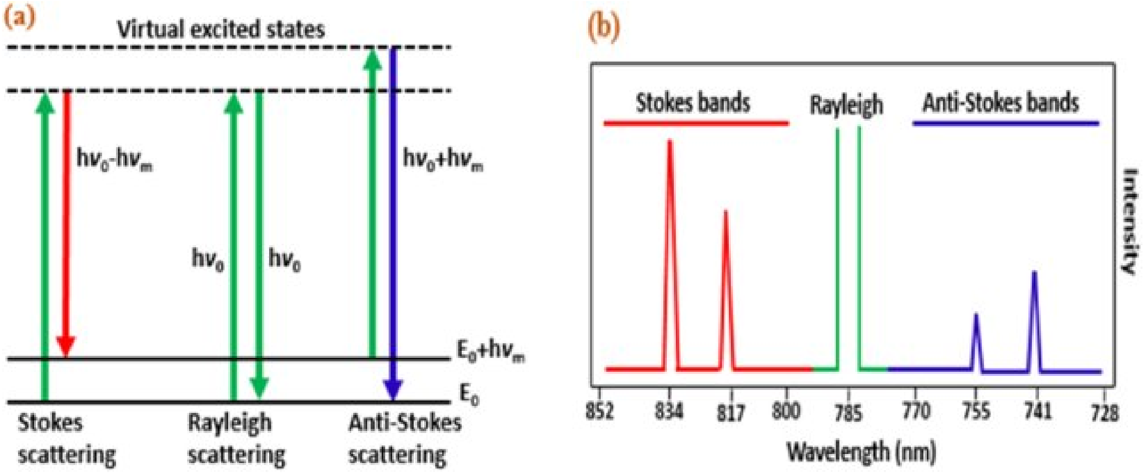

Figure 1.7 Schemes of Raman scattering, ν_0 indicates the laser frequency (a) and an illustrative diagram of the resulted Raman spectrum (b). Reprinted from Lohumi et al. [116] with permission from Elsevier.

X-ray diffraction (XRD)

X-ray diffraction (XRD) is useful for understanding the crystal structure of materials, following the Bragg's law shown in equation $n\lambda$=2$dsin\theta$ (*1.5*),

$$n\lambda = 2dsin\theta \quad (1.5)$$

where *n* is a positive integer, λ is the wavelength of the incident wave, *d* is the interplanar distance and θ is the glancing angle.

In this research, XRD measurement was carried out by using a Rigaku Ultima IV powder X-ray diffractometer operated at 44 kV and 44 mA using a copper X-ray radiation (λ =1.5438 Å). Samples were scanned from 10° to 80° (2θ) with a step size of 0.02° and at the scanning speed of 2°/min.

Scanning Electron Microscopy – Energy-Dispersive X-ray Spectroscopy (SEM-EDS)

Scanning electron microscopy (SEM) uses electrons instead of photons to observe the surface of materials. Due to the extremely short de Broglie wavelength of high-speed electrons, SEM is an invaluable tool to find out the surface morphology of nanomaterials. An X-ray detector can be coupled with the SEM and obtain the energy-dispersive X-ray spectroscopy (EDS) of the observed material. The incident electron beam from the SEM excited electrons within the sample to an excited energy state. Upon relaxing to a reduced energy state, the sample emits a photon in the X-ray spectrum whose energy level is characteristic of the electronic energy states of the host atom. The detector gathers the emission from the excited atoms, showing the elemental composition and even distribution mapping in the target material.

In this research, a FEI Quanta 600 FEG ESEM coupled with a Bruker Quantax 200 Silicon Drift Detector with Xflash 6 for X-ray energy dispersive spectroscopy was used for SEM images, elemental analysis and mapping.

Zeta Potential

When nanoparticles are dispersed in suspension media and form colloidal dispersions, due to the surface effect, an electrical double layer usually formed interfacial between nanoparticles and the fluid. [117] Zeta potential is the measure of potential at the slipping plane. In other words, it is the potential difference between the dispersion material and the stationary layer of fluid attached to the material, concluded as Stern model, [118] shown in Figure 1.8. Zeta potential is usually a good indicator to judge the stability behavior of a colloid. A high zeta potential number (usually > 30), either positive or negative, indicates strong surface electrical charge and interaction between particle and the fluid, leading to a stable dispersion, and vice versa.

In this research, the zeta potential of nanoparticles dispersions is measured by a Delsa Nano Potential and Submicron Particle Size Analyzer.

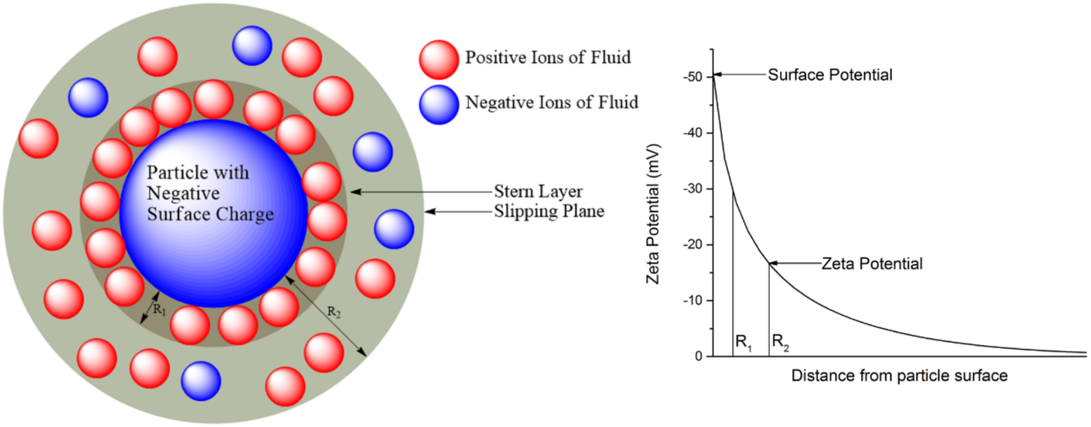

Figure 1.8 Diagram of the model of zeta potential and stern potential theory.

Dynamic Light Scattering (DLS)

As discussed in Raman spectrum, Rayleigh scattering occurs when light hits small particles. In dispersions, nanoparticles move and collide randomly, known as Brownian motion, causing the phase change of scattering light. In a system with multiple nanoparticles, the Brownian motion of different particles caused the change of final intensity of scattering light. The speed of movement depends on the size of the particles, so does the intensity change of scattering light. By analyzing the light signal dynamically, the distribution of particle sizes can be found.

In this research, the zeta potential of nanoparticles dispersions is measured by a Delsa Nano Potential and Submicron Particle Size Analyzer.

Differential Scanning Calorimetry – Thermogravimetric Analysis (DSC-TGA)

Materials undergo physical and chemical changes when heated. Thermogravimetric analysis (TGA) reveals the change of material mass when heated to a specific temperature, indicating the loss of mass due to decomposition. Differential scanning calorimetry (DSC) measures heat into and out of a material. This information is associated with physical processes such as phase change, or chemical processes such as exothermal / endothermal chemical reactions. DSC is one of the most important research tools in the field of energetic material since it reveals the energy release of the material during energetic reaction.

In this research, the DSC-TGA analysis was carried out by a TA instrument SDT 600. The samples were heated from room temperature to target temperature (800 or 1200 °C) under the protection of Argon at 200 mL·min^{-1}.

Combustion linear propagation speed measurement

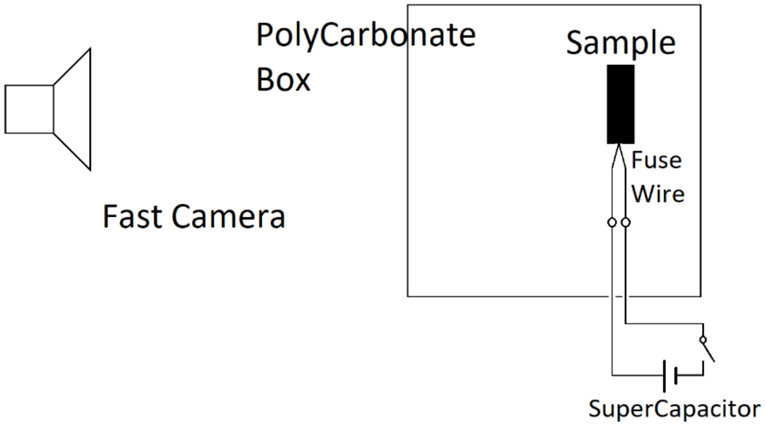

Figure 1.9 Top view of the custom-built setup for combustion linear propagation speed test.

The rapid and self-standing combustion is a nature of energetic material. Linear propagation speed is one of the most important indicators of the reactivity of energetic materials.

In this research, the speed of linear propagation was captured by a Phantom fast camera. The frame speed was set at 100,000 fps, so the time difference between neighboring frames was 10 μs.

Electrostatic Discharge (ESD)

Nanoenergetic materials are sensitive to electrical static discharge (ESD). Therefore, a system was built to measure the safety ESD threshold of the produced material. In this research, ESD sensitivity test was carried out by using a system from Electro-Tech Systems (ETS) Inc (Model 931), which is consisted of a 300 – 20,000 pF capacitor bank charged in a range from 100 V to 26 kV. Samples filled were placed within an electrically grounded stainless-steel well surrounded by a plastic ring. The discharging tip was placed about ~1mm above the sample.

1.6. References

[1] J. Kelly, *Gunpowder: Alchemy, Bombards, and Pyrotechnics: The History of the Explosive that Changed the World*. Basic Books, 2004.

[2] A. K. Sikder and N. Sikder, "A review of advanced high performance, insensitive and thermally stable energetic materials emerging for military and space applications," *Journal of Hazardous Materials,* vol. 112, no. 1, pp. 1-15, 2004/08/09/ 2004.

[3] C. Rossi, K. Zhang, D. Esteve, P. Alphonse, P. Tailhades, and C. Vahlas, "Nanoenergetic materials for MEMS: A review," (in English), *Journal of Microelectromechanical Systems,* Article vol. 16, no. 4, pp. 919-931, Aug 2007.

[4] L. H. Blair, A. Colakel, R. M. Vrcelj, I. Sinclair, and S. J. Coles, "Metal–organic fireworks: MOFs as integrated structural scaffolds for pyrotechnic materials," *Chemical Communications,* 10.1039/C5CC04174K vol. 51, no. 61, pp. 12185-12188, 2015.

[5] P. F. Pagoria, G. S. Lee, A. R. Mitchell, and R. D. Schmidt, "A review of energetic materials synthesis," *Thermochimica Acta,* vol. 384, no. 1, pp. 187-204, 2002/02/25/ 2002.

[6] D. M. Badgujar, M. B. Talawar, S. N. Asthana, and P. P. Mahulikar, "Advances in science and technology of modern energetic materials: an overview," (in eng), *J Hazard Mater,* vol. 151, no. 2-3, pp. 289-305, Mar 1 2008.

[7] L. L. Wang, Z. A. Munir, and Y. M. Maximov, "Thermite reactions: their utilization in the synthesis and processing of materials," *Journal of Materials Science,* vol. 28, no. 14, pp. 3693-3708, 1993/07/01 1993.

[8] K. J. Blobaum, M. E. Reiss, J. M. Plitzko, and T. P. Weihs, "Deposition and characterization of a self-propagating CuOx/Al thermite reaction in a multilayer foil geometry," *Journal of Applied Physics,* vol. 94, no. 5, pp. 2915-2922, 2003.

[9] S. H. Fischer and M. C. Grubelich, "Theoretical energy release of thermites, intermetallics, and combustible metals," United States 1998-06-01 1998, Available: https://www.osti.gov/servlets/purl/658208.

[10] T. Liu, X. Chen, H. Xu, A. Han, M. Ye, and G. Pan, "Preparation and Properties of Boron-Based Nano-B/NiO Thermite," *Propellants, Explosives, Pyrotechnics,* vol. 40, no. 6, pp. 873-879, 2015/12/01 2015.

[11] B. J. Bellott, W. Noh, R. G. Nuzzo, and G. S. Girolami, "Nanoenergetic materials: boron nanoparticles from the pyrolysis of decaborane and their functionalisation," *Chemical Communications,* 10.1039/B902371B no. 22, pp. 3214-3215, 2009.

[12] C. R. Becker *et al.*, "Galvanic Porous Silicon Composites for High-Velocity Nanoenergetics," *Nano Letters,* vol. 11, no. 2, pp. 803-807, 2011/02/09 2011.

[13] X. Zhou *et al.*, "Highly Exothermic and Superhydrophobic Mg/Fluorocarbon Core/Shell Nanoenergetic Arrays," *ACS Applied Materials & Interfaces,* vol. 6, no. 13, pp. 10497-10505, 2014/07/09 2014.

[14] Q. S. Meng, S. P. Chen, J. F. Zhao, H. Zhang, H. X. Zhang, and Z. A. Munir, "Microstructure and mechanical properties of multilayer-lined composite pipes prepared by SHS centrifugal-thermite process," *Materials Science and Engineering: A*, vol. 456, no. 1, pp. 332-336, 2007/05/15/ 2007.

[15] S. R. Ghanta and K. Muralidharan, "Chemical synthesis of aluminum nanoparticles," *Journal of Nanoparticle Research,* vol. 15, no. 6, p. 1715, 2013/05/23 2013.

[16] S. Bhattacharya, A. K. Agarwal, T. Rajagopalan, and V. K. Patel, *Nano-Energetic Materials* (Energy, Environment, and Sustainability). Springer, Singapore, 2019.

[17] P. Dupiano, D. Stamatis, and E. L. Dreizin, "Hydrogen production by reacting water with mechanically milled composite aluminum-metal oxide powders," (in English), *International Journal of Hydrogen Energy,* Article vol. 36, no. 8, pp. 4781-4791, Apr 2011.

[18] S. Apperson *et al.*, "Generation of fast propagating combustion and shock waves with copper oxide/aluminum nanothermite composites," *Applied Physics Letters,* vol. 91, no. 24, p. 243109, 2007.

[19] R. Shende *et al.*, "Nanoenergetic composites of CuO nanorods, nanowires, and Al-nanoparticles," (in English), *Propellants Explosives Pyrotechnics,* Article vol. 33, no. 2, pp. 122-130, Apr 2008.

[20] K. B. Plantier, M. L. Pantoya, and A. E. Gash, "Combustion wave speeds of nanocomposite Al/Fe2O3: the effects of Fe2O3 particle synthesis technique," *Combustion and Flame,* vol. 140, no. 4, pp. 299-309, Mar 2005.

[21] T. M. Tillotson, A. E. Gash, R. L. Simpson, L. W. Hrubesh, J. H. Satcher, and J. F. Poco, "Nanostructured energetic materials using sol-gel methodologies," (in English), *Journal of Non-Crystalline Solids,* Article; Proceedings Paper vol. 285, no. 1-3, pp. 338-345, Jun 2001.

[22] C. S. Staley, C. J. Morris, R. Thiruvengadathan, S. J. Apperson, K. Gangopadhyay, and S. Gangopadhyay, "Silicon-based bridge wire micro-chip initiators for bismuth oxide–aluminum nanothermite," *Journal of Micromechanics and Microengineering,* vol. 21, no. 11, p. 115015, 2011.

[23] C. S. Staley *et al.*, "Effect of Nitrocellulose Gasifying Binder on Thrust Performance and High-g Launch Tolerance of Miniaturized Nanothermite

Thrusters," *Propellants, Explosives, Pyrotechnics,* vol. 39, no. 3, pp. 374-382, 2014.

[24] S. M. Umbrajkar, S. Seshadri, M. Schoenitz, V. K. Hoffmann, and E. L. Dreizin, "Aluminum-rich Al-MoO3 nanocomposite powders prepared by arrested reactive milling," *Journal of Propulsion and Power,* vol. 24, no. 2, pp. 192-198, Mar-Apr 2008.

[25] N. Zakiyyan *et al.*, "Combustion of aluminum nanoparticles and exfoliated 2D molybdenum trioxide composites," *Combustion and Flame,* vol. 187, pp. 1-10, 2018/01/01/ 2018.

[26] B. K. Little *et al.*, "Chemical dynamics of nano-aluminum/iodine (V) oxide," *Journal of Physics: Conference Series,* vol. 500, no. 5, p. 052025, 2014/05/07 2014.

[27] B. R. Clark and M. L. Pantoya, "The aluminium and iodine pentoxide reaction for the destruction of spore forming bacteria," *Physical Chemistry Chemical Physics,* 10.1039/C0CP00473A vol. 12, no. 39, pp. 12653-12657, 2010.

[28] L. Glavier *et al.*, "Nanoenergetics as pressure generator for nontoxic impact primers: Comparison of Al/Bi2O3, Al/CuO, Al/MoO3 nanothermites and Al/PTFE," *Combustion and Flame,* vol. 162, no. 5, pp. 1813-1820, 2015/05/01/ 2015.

[29] M. L. Pantoya and S. W. Dean, "The influence of alumina passivation on nano-Al/Teflon reactions," *Thermochimica Acta,* vol. 493, no. 1, pp. 109-110, 2009/09/10/ 2009.

[30] H. Wang, M. Rehwoldt, D. J. Kline, T. Wu, P. Wang, and M. R. Zachariah, "Comparison study of the ignition and combustion characteristics of directly-written Al/PVDF, Al/Viton and Al/THV composites," *Combustion and Flame,* vol. 201, pp. 181-186, 2019/03/01/ 2019.

[31] X. Li, P. Guerieri, W. Zhou, C. Huang, and M. R. Zachariah, "Direct Deposit Laminate Nanocomposites with Enhanced Propellent Properties," *ACS Applied Materials & Interfaces,* vol. 7, no. 17, pp. 9103-9109, 2015/05/06 2015.

[32] B. Andrey *et al.*, "Modified Nanoenergetic Composites with Tunable Combustion Characteristics for Propellant Applications," *Propellants, Explosives, Pyrotechnics,* vol. 35, no. 4, pp. 384-394, 2010.

[33] L. Durães, B. F. O. Costa, R. Santos, A. Correia, J. Campos, and A. Portugal, "Fe2O3/aluminum thermite reaction intermediate and final products characterization," *Materials Science and Engineering: A,* vol. 465, no. 1, pp. 199-210, 2007/09/15/ 2007.

[34] S. J. Apperson *et al.*, "Characterization of Nanothermite Material for Solid-Fuel Microthruster Applications," *Journal of Propulsion and Power,* vol. 25, no. 5, pp. 1086-1091, 2009/09/01 2009.

[35] G. M. Dutro, R. A. Yetter, G. A. Risha, and S. F. Son, "The effect of stoichiometry on the combustion behavior of a nanoscale Al/MoO3 thermite," *Proceedings of the Combustion Institute,* vol. 32, no. 2, pp. 1921-1928, 2009/01/01/ 2009.

[36] K. Lee *et al.*, "Divide and Combust: Effect of Morphology of CuO Nanowires on the Combustion Rate of Al Nanoparticle-CuO Nanowire Thermite Composites," *Science of Advanced Materials,* vol. 8, no. 1, pp. 185-189, // 2016.

[37] R. W. J. Bickes, M. C. Grubelich, D. E. Wackerbarth, and J. H. Mohler, "A low-ignition energy, SCB, thermite igniter,"; Sandia National Labs., Albuquerque, NM (United States) SAND-96-0480C; CONF-9607122-1; Other: ON: DE96010546; TRN: AHC29613%%135 United States Other: ON: DE96010546; TRN: AHC29613%%135 OSTI as DE96010546 SNL English, 1996.

[38] M. R. Weismiller, J. Y. Malchi, J. G. Lee, R. A. Yetter, and T. J. Foley, "Effects of fuel and oxidizer particle dimensions on the propagation of aluminum containing thermites," *Proceedings of the Combustion Institute,* vol. 33, pp. 1989-1996, 2011.

[39] D. D. Dlott, "Thinking big (and small) about energetic materials," *Materials Science and Technology,* vol. 22, no. 4, pp. 463-473, 2006/04/01 2006.

[40] P. M. L. and G. J. J., "Combustion Behavior of Highly Energetic Thermites: Nano versus Micron Composites," *Propellants, Explosives, Pyrotechnics,* vol. 30, no. 1, pp. 53-62, 2005.

[41] M. L. Pantoya and J. J. Granier, "Theeffect of slow heating rates on the reaction mechanisms of nano and microncomposite thermite reactions," *Journal of Thermal Analysis and Calorimetry,* vol. 85, no. 1, pp. 37-43, 2006/07/01 2006.

[42] C. E. Aumann, G. L. Skofronick, and J. A. Martin, "Oxidation behavior of aluminum nanopowders," *Journal of Vacuum Science & Technology B: Microelectronics and Nanometer Structures Processing, Measurement, and Phenomena,* vol. 13, no. 3, pp. 1178-1183, 1995/05/01 1995.

[43] V. E. Sanders, B. W. Asay, T. J. Foley, B. C. Tappan, A. N. Pacheco, and S. F. Son, "Reaction Propagation of Four Nanoscale Energetic Composites (Al/MoO3, Al/WO3, Al/CuO, and Bi2O3)," *Journal of Propulsion and Power,* vol. 23, no. 4, pp. 707-714, 2007/07/01 2007.

[44] E. Roduner, "Size matters: why nanomaterials are different," *Chemical Society Reviews,* 10.1039/B502142C vol. 35, no. 7, pp. 583-592, 2006.

[45] D. Sundaram, V. Yang, and R. A. Yetter, "Metal-based nanoenergetic materials: Synthesis, properties, and applications," *Progress in Energy and Combustion Science,* vol. 61, pp. 293-365, 2017/07/01/ 2017.

[46] B. Chen *et al.*, "In Situ Characterization of Photothermal Nanoenergetic Combustion on a Plasmonic Microchip," *ACS Applied Materials & Interfaces,* vol. 10, no. 1, pp. 427-436, 2018/01/10 2018.

[47] R. Thiruvengadathan *et al.*, "A Versatile Self-Assembly Approach toward High Performance Nanoenergetic Composite Using Functionalized Graphene," *Langmuir,* vol. 30, no. 22, pp. 6556-6564, Jun 2014.

[48] J. A. Puszynski, "Processing and characterization of aluminum-based nanothermites," *Journal of Thermal Analysis and Calorimetry,* journal article vol. 96, no. 3, pp. 677-685, June 01 2009.

[49] A. Wang *et al.*, "Reactive nanoenergetic graphene aerogel synthesized by one-step chemical reduction," *Combustion and Flame,* vol. 196, pp. 400-406, 2018/10/01/ 2018.

[50] K. T. Sullivan *et al.*, "Reactive sintering: An important component in the combustion of nanocomposite thermites," *Combustion and Flame,* vol. 159, no. 1, pp. 2-15, Jan 2012.

[51] P. Chakraborty and M. R. Zachariah, "Do nanoenergetic particles remain nano-sized during combustion?," *Combustion and Flame,* vol. 161, no. 5, pp. 1408-1416, May 2014.

[52] M. Comet, B. Siegert, F. Schnell, V. Pichot, F. Ciszek, and D. Spitzer, "Phosphorus-Based Nanothermites: A New Generation of Pyrotechnics Illustrated by the Example of n-CuO/Red P Mixtures," *Propellants, Explosives, Pyrotechnics,* vol. 35, no. 3, pp. 220-225, 2010.

[53] *NATO Standardization Agreement (STANAG) on Explosives, Impact Sensitivity Tests, No. 4489, Ed. 1*, 1999.

[54] C. S. Staley *et al.*, "Fast-Impulse Nanothermite Solid-Propellant Miniaturized Thrusters," *Journal of Propulsion and Power,* vol. 29, no. 6, pp. 1400-1409, 2013/11/01 2013.

[55] J. L. Cheng, H. H. Hng, H. Y. Ng, P. C. Soon, and Y. W. Lee, "Synthesis and characterization of self-assembled nanoenergetic Al-Fe2O3 thermite system," (in English), *Journal of Physics and Chemistry of Solids,* Article vol. 71, no. 2, pp. 90-94, Feb 2010.

[56] J. L. Cheng, H. H. Hng, Y. W. Lee, S. W. Du, and N. N. Thadhani, "Kinetic study of thermal- and impact-initiated reactions in Al–Fe2O3 nanothermite," *Combustion and Flame,* vol. 157, no. 12, pp. 2241-2249, 2010/12/01/ 2010.

[57] H.-S. Seo, J.-K. Kim, J.-W. Kim, H.-S. Kim, and K.-K. Koo, "Thermal behavior of Al/MoO3 xerogel nanocomposites," *J. Ind. Eng. Chem.*, vol. 20, pp. 189–193, 2014.

[58] J. Gesner, M. L. Pantoya, and V. I. Levitas, "Effect of oxide shell growth on nano-aluminum thermite propagation rates," *Combustion and Flame*, vol. 159, no. 11, pp. 3448-3453, 2012/11/01/ 2012.

[59] K. Sullivan and M. Zachariah, "Simultaneous Pressure and Optical Measurements of Nanoaluminum Thermites: Investigating the Reaction Mechanism," *Journal of Propulsion and Power*, vol. 26, no. 3, pp. 467-472, 2010/05/01 2010.

[60] M. A. Trunov, M. Schoenitz, X. Zhu, and E. L. Dreizin, "Effect of polymorphic phase transformations in Al2O3 film on oxidation kinetics of aluminum powders," *Combustion and Flame*, vol. 140, no. 4, pp. 310-318, 2005/03/01/ 2005.

[61] E. L. Dreizin, "Metal-based reactive nanomaterials," *Progress in Energy and Combustion Science*, vol. 35, no. 2, pp. 141-167, 4// 2009.

[62] K. W. Watson, M. L. Pantoya, and V. I. Levitas, "Fast reactions with nano- and micrometer aluminum: A study on oxidation versus fluorination," *Combustion and Flame*, vol. 155, no. 4, pp. 619-634, 2008/12/01/ 2008.

[63] V. I. Levitas, B. W. Asay, S. F. Son, and M. Pantoya, "Melt dispersion mechanism for fast reaction of nanothermites," *Applied Physics Letters*, vol. 89, no. 7, p. 071909, 2006/08/14 2006.

[64] V. I. Levitas, "Burn time of aluminum nanoparticles: Strong effect of the heating rate and melt-dispersion mechanism," *Combustion and Flame*, vol. 156, no. 2, pp. 543-546, Feb 2009.

[65] V. I. Levitas, B. W. Asay, S. F. Son, and M. Pantoya, "Mechanochemical mechanism for fast reaction of metastable intermolecular composites based on dispersion of liquid metal," *Journal of Applied Physics*, vol. 101, no. 8, p. 083524, 2007/04/15 2007.

[66] C. Roy, C. Dubois, P. Lafleur, and P. Brousseau, "The dispersion and polymer coating of ultrafine aluminum powders by the Ziegler Natta reaction," *MRS Proceedings*, vol. 800, p. AA2.5, 2003, Art. no. Aa2.5.

[67] F. Séverac, P. Alphonse, A. Estève, A. Bancaud, and C. Rossi, "High-Energy Al/CuO Nanocomposites Obtained by DNA-Directed Assembly," *Advanced Functional Materials*, vol. 22, no. 2, pp. 323-329, 2012.

[68] T. Wu, X. Wang, P. Y. Zavalij, J. B. DeLisio, H. Wang, and M. R. Zachariah, "Performance of iodine oxides/iodic acids as oxidizers in thermite systems," *Combustion and Flame*, vol. 191, pp. 335-342, 2018/05/01/ 2018.

[69] K. S. Novoselov *et al.*, "Electric field effect in atomically thin carbon films," (in English), *Science,* Article vol. 306, no. 5696, pp. 666-669, Oct 2004.

[70] A. K. Geim and K. S. Novoselov, "The rise of graphene," (in English), *Nature Materials,* Article vol. 6, no. 3, pp. 183-191, Mar 2007.

[71] M. Mecklenburg and B. C. Regan, "Spin and the Honeycomb Lattice: Lessons from Graphene," *Physical Review Letters,* vol. 106, no. 11, p. 116803, 03/16/ 2011.

[72] M. Freitag, "Nanoelectronics goes flat out," *Nature Nanotechnology,* vol. 3, no. 8, pp. 455-457, 2008/08/01 2008.

[73] H. Chen, M. B. Müller, K. J. Gilmore, G. G. Wallace, and D. Li, "Mechanically Strong, Electrically Conductive, and Biocompatible Graphene Paper," *Advanced Materials,* vol. 20, no. 18, pp. 3557-3561, 2008.

[74] Z.-S. Wu *et al.*, "Synthesis of Graphene Sheets with High Electrical Conductivity and Good Thermal Stability by Hydrogen Arc Discharge Exfoliation," *ACS Nano,* vol. 3, no. 2, pp. 411-417, 2009/02/24 2009.

[75] J.-H. Chen, C. Jang, S. Xiao, M. Ishigami, and M. S. Fuhrer, "Intrinsic and extrinsic performance limits of graphene devices on SiO2," *Nature Nanotechnology,* vol. 3, no. 4, pp. 206-209, 2008/04/01 2008.

[76] C. L. Kane and E. J. Mele, "Quantum Spin Hall Effect in Graphene," *Physical Review Letters,* vol. 95, no. 22, p. 226801, 11/23/ 2005.

[77] C. Lee, X. Wei, J. W. Kysar, and J. Hone, "Measurement of the Elastic Properties and Intrinsic Strength of Monolayer Graphene," *Science,* vol. 321, no. 5887, pp. 385-388, 2008.

[78] R. R. Nair *et al.*, "Fine structure constant defines visual transparency of graphene," (in English), *Science,* Article vol. 320, no. 5881, pp. 1308-1308, Jun 2008.

[79] T. Kuila, S. Bose, A. K. Mishra, P. Khanra, N. H. Kim, and J. H. Lee, "Chemical functionalization of graphene and its applications," *Progress in Materials Science,* vol. 57, no. 7, pp. 1061-1105, 2012/09/01/ 2012.

[80] M. J. McAllister *et al.*, "Single Sheet Functionalized Graphene by Oxidation and Thermal Expansion of Graphite," *Chemistry of Materials,* vol. 19, no. 18, pp. 4396-4404, 2007/09/01 2007.

[81] I. A. Baburin, A. Klechikov, G. Mercier, A. Talyzin, and G. Seifert, "Hydrogen adsorption by perforated graphene," *International Journal of Hydrogen Energy,* vol. 40, no. 20, pp. 6594-6599, 2015/06/01/ 2015.

[82] V. H. Luan *et al.*, "Synthesis of a highly conductive and large surface area graphene oxide hydrogel and its use in a supercapacitor," *Journal of Materials Chemistry A*, 10.1039/C2TA00444E vol. 1, no. 2, pp. 208-211, 2013.

[83] R. Muszynski, B. Seger, and P. V. Kamat, "Decorating Graphene Sheets with Gold Nanoparticles," *The Journal of Physical Chemistry C,* vol. 112, no. 14, pp. 5263-5266, 2008/04/01 2008.

[84] Y. Si and E. T. Samulski, "Exfoliated Graphene Separated by Platinum Nanoparticles," *Chemistry of Materials,* vol. 20, no. 21, pp. 6792-6797, 2008/11/11 2008.

[85] X. Ji, Y. Xu, W. Zhang, L. Cui, and J. Liu, "Review of functionalization, structure and properties of graphene/polymer composite fibers," *Composites Part A: Applied Science and Manufacturing,* vol. 87, pp. 29-45, 2016/08/01/ 2016.

[86] B. Garg, T. Bisht, and Y.-C. Ling, "Graphene-based nanomaterials as heterogeneous acid catalysts: a comprehensive perspective," (in eng), *Molecules (Basel, Switzerland),* vol. 19, no. 9, pp. 14582-14614, 2014.

[87] G. K. Dimitrakakis, E. Tylianakis, and G. E. Froudakis, "Pillared Graphene: A New 3-D Network Nanostructure for Enhanced Hydrogen Storage," *Nano Letters,* vol. 8, no. 10, pp. 3166-3170, 2008/10/08 2008.

[88] H. J. Yoon, D. H. Jun, J. H. Yang, Z. Zhou, S. S. Yang, and M. M.-C. Cheng, "Carbon dioxide gas sensor using a graphene sheet," *Sensors and Actuators B: Chemical,* vol. 157, no. 1, pp. 310-313, 2011/09/20/ 2011.

[89] S. Deng *et al.*, "Reduced Graphene Oxide Conjugated Cu2O Nanowire Mesocrystals for High-Performance NO2 Gas Sensor," *Journal of the American Chemical Society,* vol. 134, no. 10, pp. 4905-4917, 2012/03/14 2012.

[90] X. Zhou *et al.*, "Dopamine fluorescent sensors based on polypyrrole/graphene quantum dots core/shell hybrids," *Biosensors and Bioelectronics,* vol. 64, pp. 404-410, 2015/02/15/ 2015.

[91] X. Zhou, Q. Chen, A. Wang, J. Xu, S. Wu, and J. Shen, "Bamboo-like Composites of V2O5/Polyindole and Activated Carbon Cloth as Electrodes for All-Solid-State Flexible Asymmetric Supercapacitors," *ACS Applied Materials & Interfaces,* vol. 8, no. 6, pp. 3776-3783, 2016/02/17 2016.

[92] Y. Wang *et al.*, "Supercapacitor Devices Based on Graphene Materials," *The Journal of Physical Chemistry C,* vol. 113, no. 30, pp. 13103-13107, 2009/07/30 2009.

[93] H. L. Poh, F. Šaněk, A. Ambrosi, G. Zhao, Z. Sofer, and M. Pumera, "Graphenes prepared by Staudenmaier, Hofmann and Hummers methods with consequent

thermal exfoliation exhibit very different electrochemical properties," *Nanoscale,* 10.1039/C2NR30490B vol. 4, no. 11, pp. 3515-3522, 2012.

[94] A. M. Dimiev, S. M. Bachilo, R. Saito, and J. M. Tour, "Reversible Formation of Ammonium Persulfate/Sulfuric Acid Graphite Intercalation Compounds and Their Peculiar Raman Spectra," *ACS Nano*, vol. 6, no. 9, pp. 7842-7849, 2012/09/25 2012.

[95] A. M. Dimiev and J. M. Tour, "Mechanism of Graphene Oxide Formation," (in English), *Acs Nano,* Article vol. 8, no. 3, pp. 3060-3068, Mar 2014.

[96] S. Wang, Y. Zhang, N. Abidi, and L. Cabrales, "Wettability and Surface Free Energy of Graphene Films," *Langmuir,* vol. 25, no. 18, pp. 11078-11081, 2009/09/15 2009.

[97] D. R. Dreyer, S. Park, C. W. Bielawski, and R. S. Ruoff, "The chemistry of graphene oxide," (in English), *Chemical Society Reviews,* Review vol. 39, no. 1, pp. 228-240, 2010.

[98] V. Georgakilas *et al.*, "Noncovalent Functionalization of Graphene and Graphene Oxide for Energy Materials, Biosensing, Catalytic, and Biomedical Applications," *Chemical Reviews,* vol. 116, no. 9, pp. 5464-5519, 2016/05/11 2016.

[99] J. I. Paredes, S. Villar-Rodil, A. Martinez-Alonso, and J. M. D. Tascon, "Graphene oxide dispersions in organic solvents," (in English), *Langmuir,* Article vol. 24, no. 19, pp. 10560-10564, Oct 2008.

[100] D. Konios, M. M. Stylianakis, E. Stratakis, and E. Kymakis, "Dispersion behaviour of graphene oxide and reduced graphene oxide," *Journal of Colloid and Interface Science*, vol. 430, pp. 108-112, 2014/09/15/ 2014.

[101] J. Liu, L. Cui, and D. Losic, "Graphene and graphene oxide as new nanocarriers for drug delivery applications," *Acta Biomaterialia,* vol. 9, no. 12, pp. 9243-9257, 2013/12/01/ 2013.

[102] K. Huang, G. Liu, Y. Lou, Z. Dong, J. Shen, and W. Jin, "A Graphene Oxide Membrane with Highly Selective Molecular Separation of Aqueous Organic Solution," *Angewandte Chemie International Edition,* vol. 53, no. 27, pp. 6929-6932, 2014.

[103] Y. Xu, W. Hong, H. Bai, C. Li, and G. Shi, "Strong and ductile poly(vinyl alcohol)/graphene oxide composite films with a layered structure," *Carbon,* vol. 47, no. 15, pp. 3538-3543, 2009/12/01/ 2009.

[104] M. Liu, C. Chen, J. Hu, X. Wu, and X. Wang, "Synthesis of Magnetite/Graphene Oxide Composite and Application for Cobalt(II) Removal," *The Journal of Physical Chemistry C,* vol. 115, no. 51, pp. 25234-25240, 2011/12/29 2011.

[105] O. C. Compton and S. T. Nguyen, "Graphene Oxide, Highly Reduced Graphene Oxide, and Graphene: Versatile Building Blocks for Carbon-Based Materials," *Small*, vol. 6, no. 6, pp. 711-723, 2010.

[106] I. K. Moon, J. Lee, R. S. Ruoff, and H. Lee, "Reduced graphene oxide by chemical graphitization," *Nature Communications*, vol. 1, no. 1, p. 73, 2010/09/21 2010.

[107] S. Yang, L. Zhi, K. Tang, X. Feng, J. Maier, and K. Müllen, "Efficient Synthesis of Heteroatom (N or S)-Doped Graphene Based on Ultrathin Graphene Oxide-Porous Silica Sheets for Oxygen Reduction Reactions," *Advanced Functional Materials,* vol. 22, no. 17, pp. 3634-3640, 2012/09/11 2012.

[108] L. K. Putri, B.-J. Ng, W.-J. Ong, H. W. Lee, W. S. Chang, and S.-P. Chai, "Heteroatom Nitrogen- and Boron-Doping as a Facile Strategy to Improve Photocatalytic Activity of Standalone Reduced Graphene Oxide in Hydrogen Evolution," *ACS Applied Materials & Interfaces*, vol. 9, no. 5, pp. 4558-4569, 2017/02/08 2017.

[109] R. Romero-Aburto *et al.*, "Fluorinated Graphene Oxide; a New Multimodal Material for Biological Applications," *Advanced Materials,* vol. 25, no. 39, pp. 5632-5637, 2013/10/01 2013.

[110] J.-J. Shao, W. Lv, and Q.-H. Yang, "Self-Assembly of Graphene Oxide at Interfaces," *Advanced Materials,* vol. 26, no. 32, pp. 5586-5612, 2014/08/01 2014.

[111] D. Zhang, J. Tong, and B. Xia, "Humidity-sensing properties of chemically reduced graphene oxide/polymer nanocomposite film sensor based on layer-by-layer nano self-assembly," *Sensors and Actuators B: Chemical,* vol. 197, pp. 66-72, 2014/07/05/ 2014.

[112] T. Cassagneau and J. H. Fendler, "Preparation and Layer-by-Layer Self-Assembly of Silver Nanoparticles Capped by Graphite Oxide Nanosheets," *The Journal of Physical Chemistry B,* vol. 103, no. 11, pp. 1789-1793, 1999/03/01 1999.

[113] R. Thiruvengadathan *et al.*, "Enhanced Combustion Characteristics of Bismuth Trioxide-Aluminum Nanocomposites Prepared through Graphene Oxide Directed Self-Assembly," *Propellants Explosives Pyrotechnics*, vol. 40, no. 5, pp. 729-734, Oct 2015.

[114] J. G. Smith, *Organic Chemistry*. McGraw-Hill, 2011.

[115] A. Ausili, M. Sánchez, and J. C. Gómez-Fernández, "Attenuated total reflectance infrared spectroscopy: A powerful method for the simultaneous study of structure and spatial orientation of lipids and membrane proteins," *Biomedical Spectroscopy and Imaging*, vol. 4, pp. 159-170, 2015.

[116] S. Lohumi, M. S. Kim, J. Qin, and B.-K. Cho, "Raman imaging from microscopy to macroscopy: Quality and safety control of biological materials," *TrAC Trends in Analytical Chemistry*, vol. 93, pp. 183-198, 2017/08/01/ 2017.

[117] D. C. Grahame, "The Electrical Double Layer and the Theory of Electrocapillarity," *Chemical Reviews*, vol. 41, no. 3, pp. 441-501, 1947/12/01 1947.

[118] O. Stern, "ZUR THEORIE DER ELEKTROLYTISCHEN DOPPELSCHICHT," *Zeitschrift für Elektrochemie und angewandte physikalische Chemie*, vol. 30, no. 21‐22, pp. 508-516, 1924/11/01 1924.

Chapter 2

Self-Assembled rGO/Al/Bi_2O_3 Macroscale Nanoenergetic Gel

2.1. Introduction

As discussed in Chapter 1.1, lack of scalability is one of the key problems that hinders the applications of traditional Al-based nanoenergetic materials. Some physical methods such as mechanical pressing, [1, 2] and 3D printing [3, 4] have been developed to pack nanoenergetic material powder into macroscale structures. However, the reactivity of these produced macroscale structures was found to be significantly decreased compared to the physically mixed loose nanothermite powder. The Al nanoparticles packed in the mechanically pressed pellets were found to be less likely to diffuse as individual particles while sintering during the energetic reaction and losing their nanoscale structure, leading to a decreased energetic performance such as burning rate. [5] 3D printing is able to prepare Al/CuO nanothermite mixtures devices on demand while the flame propagation velocity ranged from only 10 cm/s to 140 m/s, [4, 6] much smaller than the propagation speed over 400 m/s for original nanothermite loose powder. [7] Additionally, safely handling of nanoenergetic materials remain a problem since traditional scaling-up methods including pressing and 3D printing did not improve any stability of nanothermite materials. Considering the extremely high sensitivity of nanothermite to external input including electrostatic discharge, friction and impact, [8-10] it is very dangerous to pack a large amount of nanoenergetic materials into large structures, which significantly limits the application of nanoenergetic material. Therefore, finding a method that can reduce the sensitivity to external stimuli while retaining the energetic properties of nanoenergetic material is a focal point to improve nanoenergetic materials.

Functionalized graphene is a candidate to solve this problem as an additive in nanoenergetic composites. The outstanding mechanical strength, thermal and electrical conductivity can significantly reduce the sensitivity of as-produced nanoenergetic composites to external stimuli. [11] Moreover, the capability of synthesizing graphene macroscale aerogels in an ultralight porous structure can produce a macroscale nanoenergetic structure with very low bulk density, or TMD% (theoretical maximum density percentage). Unlike mechanically packed nanoenergetic materials, packing nanoenergetic particles in a graphene-based macroscale gel does not cause the loss of nano structures or diffusion abilities during reaction.

In recent years, significant research in three-dimensional (3D) graphene macroscale aerogel has been accomplished, with various synthesis routes and products developed. Pure graphene aerogel is one of the lightest materials in the world, giving a density less than 10 $mg \cdot cm^{-3}$ due to its extremely high porosity. [12, 13] Similar to 2D graphene sheets, 3D graphene aerogels also exhibited its outstanding characteristics including compressibility [12], mechanical strength [14], electrical conductivity [15], thermal conductivity [16] and high specific surface area up to 1300 $m^2 \cdot g^{-1}$. [17] Therefore, graphene aerogels have shown its potential applications as electrodes for electrochemical power sources, [14] supercapacitors, [18, 19] and absorbent for organic liquids. [13]

In addition to the applications of graphene aerogel itself, the characteristics of graphene macroscale aerogel made it a promising candidate for being the scaffold for nanomaterial loading to scale it up to macroscale devices having the advantages and properties of nanocomposites composed with the graphene aerogel. Various kinds of hybrid graphene aerogel have been developed and applied in different areas. MoS_2 /

graphene and SnO_2 / graphene hybrid aerogel can be used in ultrasensitive NO_2 sensor. [20, 21] Graphene aerogel – metal – organic framework can be utilized as detector for multiple heavy metal ions. [22] LiS_2 / graphene, SiO_2 graphene and boron / nitrogen doped graphene aerogel are developed as the cathodes of lithium batteries. [23-26]

The synthesis methods for 3D graphene aerogels can be categorized into two different types. One is called template-guided methods, such as chemical vapor deposition (CVD) on the surface of metallic foams to produce macroscale graphene monoliths. [27] The 3D graphene aerogel produced by CVD showed similar advantages like 2D graphene sheets produced by CVD, such as ultrahigh surface area, high electrical conductivity, very few layer numbers and great perfectness. [27, 28] However, the problems behind template – CVD method to produce 3D macroscale graphene is same as the method for producing 2D graphene sheets, which is the problem of scalability. [29] Also, the produced 3D graphene structure was generally brittle under low compression. [30] Therefore, most researchers adopted template-free approaches for scalable synthesis of self-assembled 3D graphene macroscale aerogel. Chemically derived graphene oxide (GO)-based aerogels are the most common 3D graphene macrostructures found in literature due to its simple synthesis process, ease in production of large quantities, as well as the ability to obtain different morphologies and chemical properties by modifying the condition of synthesis. [12, 31-36]

The GO-based aerogels are synthesized by solution-based chemical reaction, during which the exfoliated graphene oxide sheets crosslink with each other either through π-π interaction after reduction [30] or direct chemical cross-linking. [15, 37] Ultrahigh heating process over 1000°C is commonly required in the direct chemical cross-linking process to produce the final product, strongly limiting the application of this method. Therefore, researchers showed higher interest in reduction methods to produce graphene aerogels. Generally, the reduction methods can be classified as hydrothermal / solvothermal method, and chemical reduction method. Hydrothermal / solvothermal methods require dispersing GO in solution, sealed in autoclave and reduced in elevated temperature (150 ~ 200°C) and temperature for a few hours. [30, 38] The process was first discovered in aqueous solution, and then found applicable as well in certain kinds of organic solvents such as N,N-dimethylformamide (DMF) [39], ethylene glycol [40] and propylene carbonate (PC) [18]. Chemical reduction methods employ an extra chemical reducer, such as amine, [38] vitamin C, $NaHSO_3$, Na_2S, [41] L-ascorbic acid, [14] enabling a much lower reaction temperature around or below 100°C in GO aqueous solutions for a shorter reaction time, normally below 10 hours. [12, 14]

Macroscale self-assembled rGO/Al and rGO/Al/MO_x (MO_x refers to metal oxide) is considered to be a promising energetic composite to overcome the disadvantages of traditional nanoenergetic composites. We have recently found that chemically functionalized graphene can be engineered to facilitate directed self-assembly of dense nanoenergetic composite pellets with enhanced energy release by avoiding phase separation and reactive sintering. [42] By contrast, graphene aerogel structure, as discussed above, offers an ultralight porous scaffold [12] that absorbs mechanical energy [43], is thermally conductive [44], and is electrically conductive to optimize ESD safety, [11, 15] facilitate further chemical functionalization, [45] and facilitate 3D printing. [29] Therefore, macroscale self-assembled rGO/Al and rGO/Al/MO_x is an excellent candidate to synthesize scaled nanoenergetic material with enhanced safety and energetic performance.

However, when the previously discovered gelation methods were attempted to synthesize graphene/Al/MO_x gel, neither of them provided the desired energetic properties. Aluminum nanoparticles reacted with water at 95°C, forming Al_2O_3 within only 4 hours, as shown in Figure 2.1. Therefore, any process involving water as suspension agent cannot be adopted as the method to synthesize graphene/Al/Bi_2O_3 macroscale aerogel.

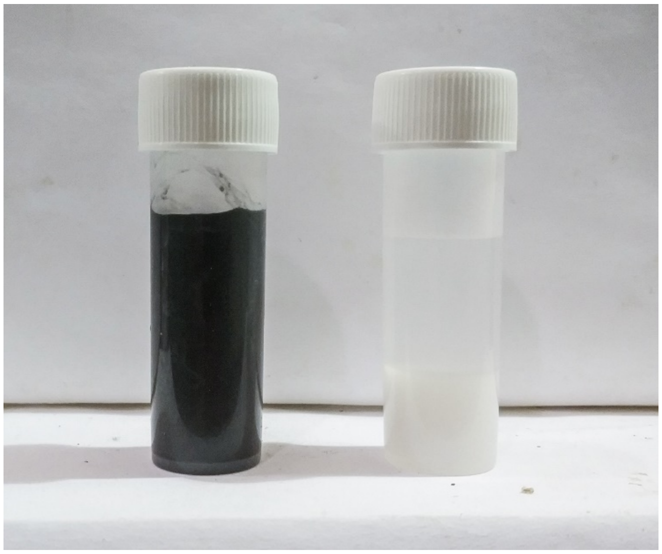

Figure 2.1 Optical pictures of Al NPs in water after mixing (left) and after heating at 95°C for 4 hours.

Therefore, organic suspension agents were next examined. DMF and PC were used to synthesize reduced graphene oxide (rGO)/Al and rGO/Al/Bi_2O_3. An rGO/Al gel was synthesized successfully, while rGO/Al/Bi_2O_3 gel was unsuccessful.

2.2. Synthesis and characterizations of rGO/Al macroscale gel

GO was synthesized by oxidation reaction of graphite using the modified Hummer's method. [42]

Briefly, 46 mL H_2SO_4 (Fisher Scientific Hampton, NH) was added slowly into a beaker with mixture of 1 g graphite nanoplatelets (xGnP H-5, 5 μm average particle size, XG Science, Lansing, MI) and 1 g $NaNO_3$ (Sigma-Aldrich, St Louis, MO) inside under cooling by ice bath and magnetic stirring. After 10 minutes, 6 g of $KMnO_4$ (Sigma-Aldrich, St Louis, MO) was added into the beaker and the solution was stirred for 1 h under 35 ℃. Subsequently, 80 mL of deionized water was added into the beaker dropwise and the water bath was heated to 90°C and maintained for half an hour. Then, 200 mL deionized water was added slowly into the reacting agent. After cooling down to ambient temperature, 6 mL H_2O_2 (Fisher Scientific Hampton, NH) was dropped into the suspension, and the mixture color changed to pale brown. A washing procedure was then employed to remove impurities and purify GO product. The centrifuging and dispersing washing step were carried out until the pH of surfactant reached 6, when all the impurities were removed. The GO was then dispersed into deionized water at a concentration around 5 $mg \cdot mL^{-1}$ and sonicated for 45 minutes to exfoliate the material into flakes. The material was then centrifuged for another 30 minutes at 4000 rpm to remove the unoxidized graphite. The supernatant was then transferred into a glass petri dish and heated in oven at 60 ℃ until the water evaporated. The resulting GO paper was then removed.

To initiate the self-assembly process, a typical amount of 25 mg Al nanoparticle (80 nm diameter, 2.2 nm alumina shell thickness, 79% active, Novacentrix, Austin, TX) and 25 mg as-synthesized GO paper were added to 5 mL propylene carbonate and sonicated to disperse, respectively. The Al and GO suspensions were then mixed and sealed into a 20 mL Teflon-coated autoclave, followed by moving the autoclave into a furnace, heated to 180 ℃ and maintained for 72 hours. After the solvothermal process, the autoclave was cooled in ambient air to room temperature. The organogel produced was then dumped into a beaker filled with isopropyl alcohol (IPA) (Fisher Scientific Hampton, NH) to undergo solvent exchange process, replacing the PC in the gel by IPA. Fresh IPA was exchanged for several times to ensure all the PC trapped in the gel has been removed. Lastly, the organogel was dried in a vacuum oven.at room temperature until the IPA evaporated. Pure rGO gel was also synthesized in the same method using GO dispersion only.

SEM and DSC-TGA were utilized to observe the structure and measure the properties of the synthesized rGO/Al gel.

After the solvothermal process, GO and Al NPs self-assembled into a homogeneous macrostructure in centimeter scale, as shown in Figure 2.2. Both Al and GO could disperse well in PC. After solvothermal process, GO was reduced to rGO and a macroscale rGO/Al gel was formed in the autoclave, as shown in Figure 2.2D. The gel was in the shape of cylinder with its height and diameter both around 1 cm. However, after vacuum drying, the porous structure of the formed rGO/Al gel [18] shrank and the size of the dried gel reduced into only a few millimeters. It resulted from the rapid removal of solvent, causing the soft gel unable to support its structure, which was also damaged by bubble from boiling solvent.

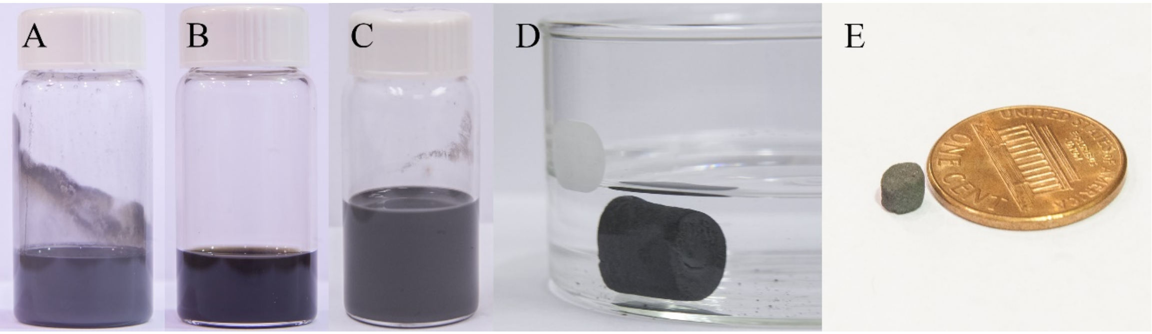

Figure 2.2 Optical pictures of Al NPs suspension in PC (A), GO dispersion in PC (B), GO/Al mixture before (C) and after (D) solvothermal process, and after solvent change and vacuum drying (E).

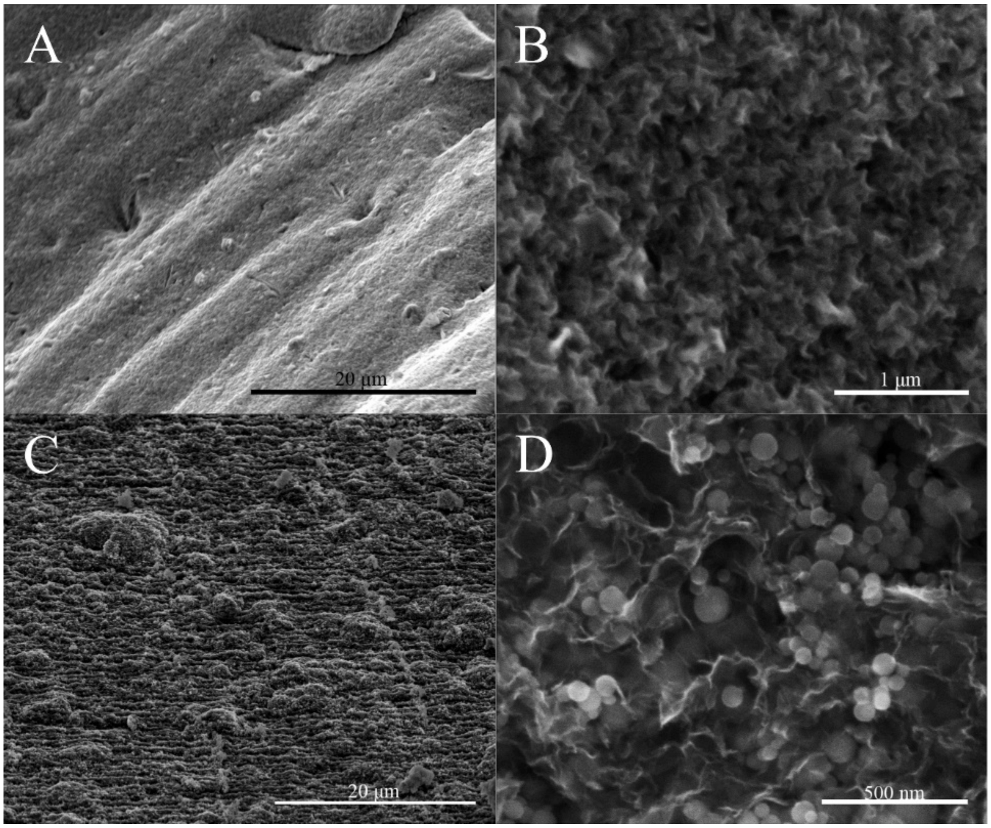

Figure 2.3 SEM images of dried pure rGO gel (A, B) and rGO/Al gel (C, D).

The structure of the formed rGO/Al gel was then confirmed by using SEM. The rGO gel showed a smooth surface in general, as shown in Figure 2.3A. When examining the cross section of the material, a densely packed layer structure of rGO sheets was observed in Figure 2.3C, resulting from the severe shrink during vacuum drying process. However, the porous structure was still preserved after vacuum drying, as shown in Figure 2.3B and Figure 2.3D. The addition of Al NPs into the rGO gel did not change the porous structure of the product.

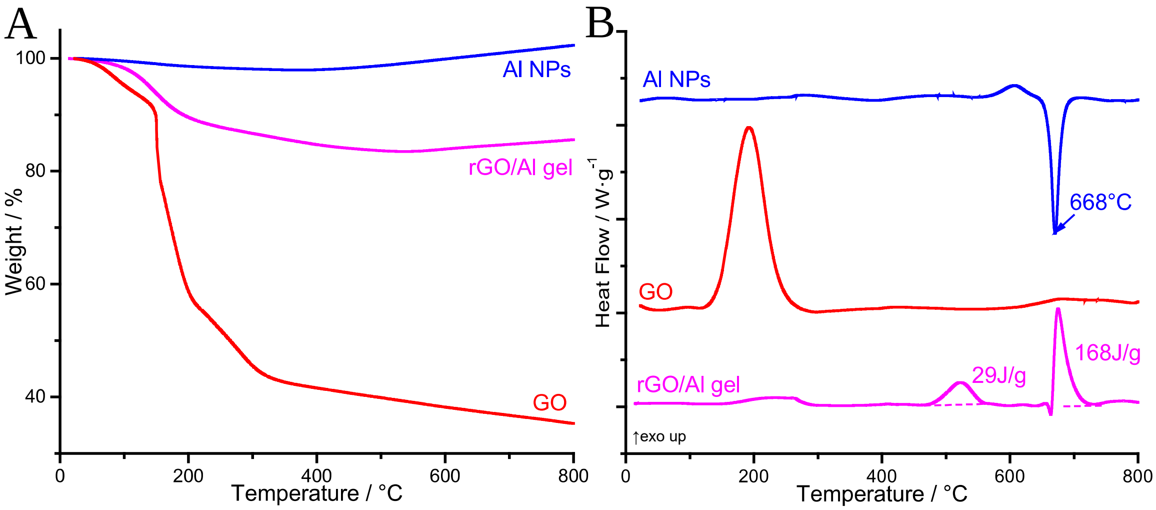

Figure 2.4 TGA (A) and DSC (B) curves of GO, Al NPs and rGO/Al gel.

DSC-TGA analysis was carried out on Al NPs, GO and rGO/Al gel to understand the change of material during the gelation process, as shown in Figure 2.4. No significant weight loss was observed for Al NPs from room temperature to 800°C. It showed a significant endothermic peak in Figure 2.4B at 668°C, indicating the melting of its Al core. As for GO, it is clear that a large weight loss occurred during the exothermic reaction from 130 to 300°C, indicating the thermal decomposition of the oxygen functional groups in GO. After the main decomposition, GO gradually lost additional mass, indicating some further decomposition at higher temperature. rGO also exhibited some mass loss around 200°C, indicating there was still some oxygen functional groups in the structure after reduction process. The DSC result, however, was distinct from that of Al and GO. The exothermic peak at the decomposition temperature was very small compared to GO, indicating the loss of some functional groups during the gelation process. Some extra exothermal peaks were found at higher temperature. The major reaction occurred at 675°C, following a small endothermic peak of Al melting, indicating the occurrence of reaction between rGO and molten Al. The energy release was 168 J/g. A minor energy release of 29 J/g was also found around 520°C, probably attributed to the reaction between diffused Al core and decomposed oxygen functional groups fragments absorbed on the alumina shell of Al NPs.

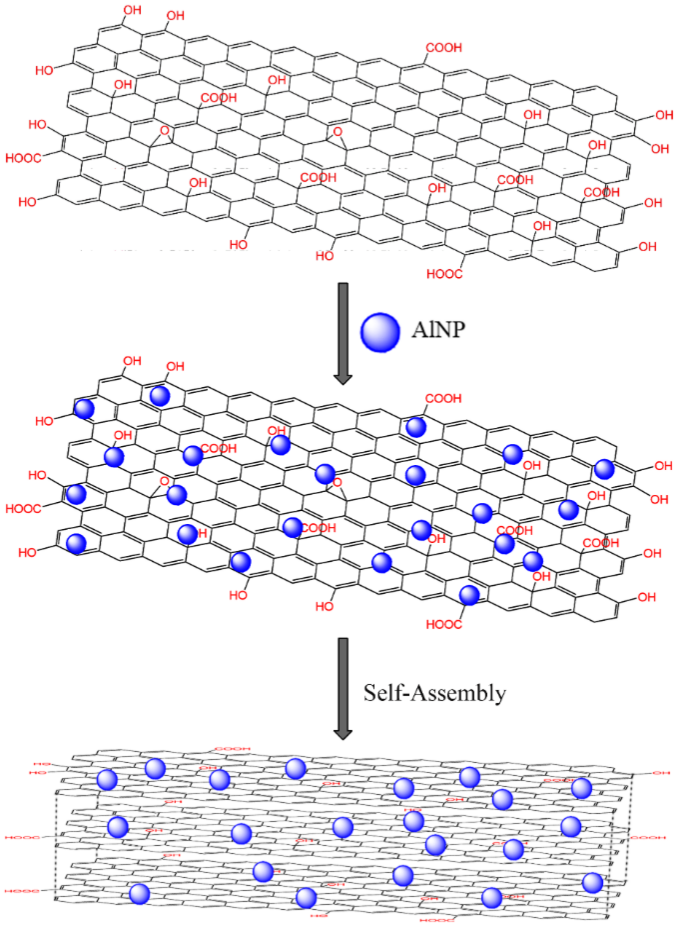

Figure 2.5 Scheme of the reaction mechanism of forming rGO/Al binary organogel during solvothermal process.

Considering the reduction of GO during the solvothermal process, the mechanism of the reaction can be summarized in Figure 2.5. After mixing GO and Al dispersion, a homogeneous mixture was formed. During the solvothermal process, the oxygen functional groups in GO, such as hydroxyl groups, epoxyl groups, and carboxyl groups, were reduced and rGO formed. The as-formed rGO sheets then formed 3D structures due to π-π interaction between layers and grew to macroscale.

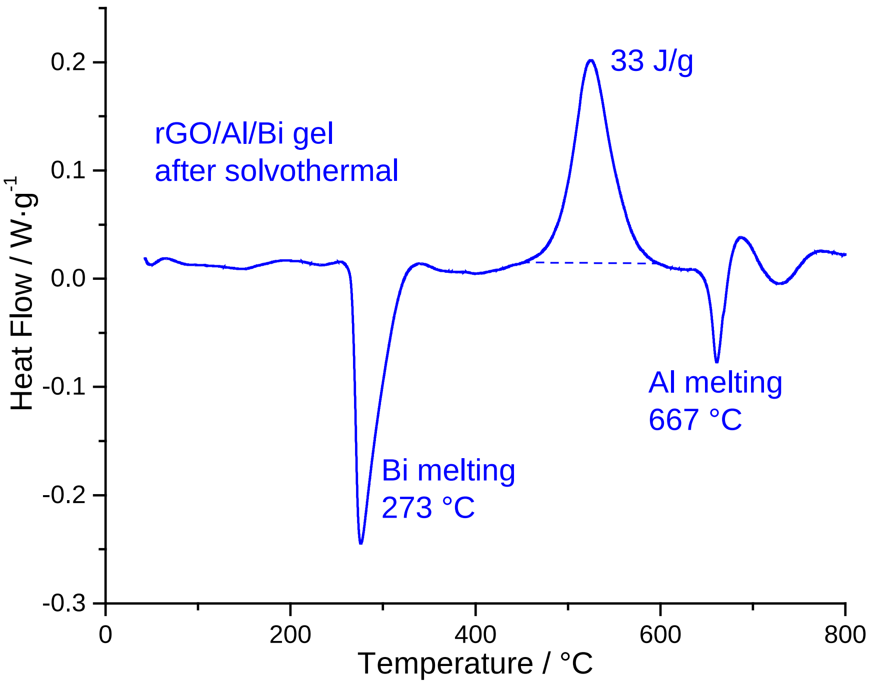

Figure 2.6 DSC curve of rGO/Al/Bi gel formed after solvothermal process of $GO/Al/Bi_2O_3$ mixture.

However, some problems were found during the synthesis and characterization of rGO/Al gel by using solvothermal method. First, the percentage of GO in original GO/Al mixture must be high enough to form the rGO/Al gel. When the concentration of GO was 2.5 g / mL in GO/Al mixture, as discussed above, the minimum mass percentage of GO was 50%. When the concentration of GO was increased to 5 g / mL in GO/Al mixture, the minimum mass percentage slightly increased to 40%. However, further increasing the concentration of GO did not reduce the GO percentage in GO/Al mixture where a gel could form after solvothermal process. Another problem was the poor energetic performance of the as-synthesized rGO/Al structure. The carbon in rGO was applied as the oxidizer, giving a small energy release of only 197 J/g. More importantly, the rGO/Al gel could not be ignited by either torch or fuse wire, indicating that the rGO/Al gel could not be defined as energetic material. Therefore, a secondary oxidizer, such as metal oxide, must be included in the structure. A few tentative experiments were carried out, and it was found that the metal oxide was reduced to simple metal during the solvothermal process. For example, the DSC result of the solvothermal synthesized rGO/Al/Bi gel from GO/Al/Bi_2O_3 mixture is shown in Figure 2.6. No significant exothermal reaction since Bi_2O_3 was reduced to Bi during the synthesis. Similarly, CuO was also reduced to Cu, and the reduction of metal oxide made the final product significantly less energetic.

It is assumed that the reduction of the metal oxide is resulted from the reductive solvent or some reductive organic species generated during the hydrothermal process. For example, DMF contains an aldehyde group, which makes DMF itself a considerably strong organic reducer in elevated temperature. Propylene carbonate itself is not a strong reducer nor containing strong reductive functional groups such as aldehyde or amine groups. However, researchers have found that at elevated temperature, the five-membered ring in propylene carbonate may open, resulting in the occurrence of polymerization or oligomerization after the ring-opening reaction. [46] The molecular after the ring opened, which may contain hydroxyl or aldehyde groups or radicals, can be reductive enough to reduce metal oxide to pure metal under elevated temperature during the solvothermal process.

2.3. Synthesis of rGO/Al/Bi_2O_3 macroscale energetic gel

Therefore, a new synthesis method needs to be developed to obtain the desired rGO/Al/MO_x structure and retain the energetic properties of the synthesized material. Therefore, the two different categories of methods were combined. In the new method, organic solvent (propylene carbonate) was used, while an extra chemical reducer (ethylenediamine) was added to make sure the gel could form in a lower temperature to avoid the reduction of MO_x.

GO was synthesized following the same method described in chapter 2.2.

Table 2.1 Summarization of the amount of different materials in rGO/Al/Bi_2O_3 gel.

GO percentage	Equivalence ratio / ER	GO (mg) / in PC (mL)	Al (mg) / in PC (mL)	Bi_2O_3 (mg) / in PC (mL)
50%	1.6	50 mg / 2.5 mL	9.5 mg / 1.25 mL	40.5 mg / 1.25 mL
25%		30 mg / 1.5 mL	17.1 mg / 0.75 mL	72.9 mg / 0.75 mL
10%		30 mg / 1.5 mL	51.3 mg / 0.75 mL	218.7 mg / 0.75 mL
5%	1.6	30 mg / 1.5 mL	108.3 mg / 0.75 mL	461.7 mg / 0.75 mL
	1.4	30 mg / 1.5 mL	97.1 mg / 0.75 mL	472.9 mg / 0.75 mL
	1.2	30 mg / 1.5 mL	85.3 mg / 0.75 mL	484.7 mg / 0.75 mL
	1.0	30 mg / 1.5 mL	72.9 mg / 0.75 mL	497.1 mg / 0.75 mL
4%	1.4	10 mg / 0.5 mL	40.9 mg / 0.25 mL	199.1 mg / 0.25 mL
3%	1.4	10 mg / 0.5 mL	55.1 mg / 0.25 mL	268.2 mg / 0.25 mL

The synthesis of macroscale rGO/Al/Bi_2O_3 was initiated by dispersing all the three different materials in propylene carbonate (PC). The detailed amount of GO, Al and Bi_2O_3 in PC is summarized in Table 2.1 and the equivalence ratio is calculated by Equation 2.1.

$$\Phi = \frac{[n(fuel)/n(oxidizer)]_{actual}}{[n(fuel)/n(oxidizer)]_{stoichiometry}} \tag{2.1}$$

To initiate the self-assembly process, as-produced GO paper, Al nanoparticles and Bi_2O_3 nanoparticles (200 nm labelled diameter, Sigma-Aldrich, St Louis, MO) were separately dispersed into propylene carbonate and sonicated for 4 hours. Equivalence ratio was calculated by the ratio of fuel / oxidizer over stoichiometric value. After 4 hours of sonication, Al and Bi_2O_3 dispersions were mixed and sonicated for another hour before the addition of GO dispersion. Afterwards, the dispersions were mixed together by vortexing for 10 minutes in a vial and rested for 16 hours. Then 40 μL ethylenediamine was injected to the mixture to initiate gelation, and the vial was moved to a 95 ℃ oven for 8 hours. After the gelling process, the product was cooled in ambient air to room temperature. The organogel was then placed in a beaker filled with tert-butanol to undergo solvent exchange. Lastly, the material was freeze dried under vacuum in a freeze dryer to remove solvent. An extra sample dried under vacuum without being frozen was also synthesized. Optical pictures taken during the process are shown in Figure 2.7.

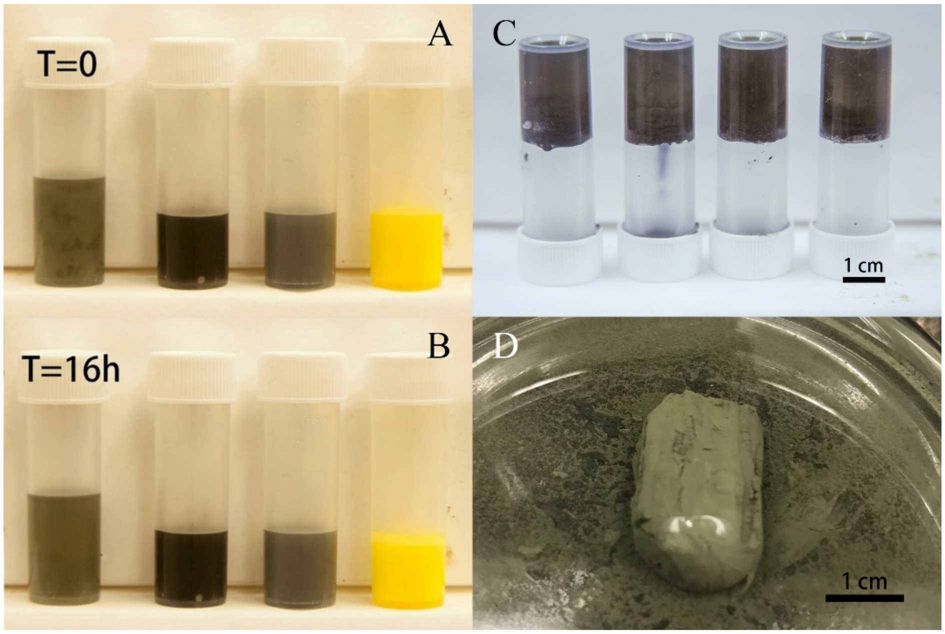

Figure 2.7 Optical pictures of $GO/Al/Bi_2O_3$ mixture in PC and their standalone dispersions right after (A) and 16 hours after (B) sonication, and the formed gel after gelation (C) and during solvent change process (D).

Al/Bi_2O_3 control sample for reference was made in IPA, following the standard process reported in prior work. [47] In a typical process, 400 mg Bi_2O_3 was firstly dispersed in 1.2 mL IPA under sonication for 1 hour. Subsequently, calculated amount of Al NPs (82 mg for Φ = 1.4, 94 mg for Φ = 1.6) was directly scaled and added into the dispersion and sonicated for an extra 4 hours. The Al/Bi_2O_3 slurry was then moved to a bowl-shaped Al foil and dried under vacuum. For the control Al/Bi_2O_3 sample made in PC, calculated amount of Al and Bi_2O_3 (200 mg in total, Φ = 1.4) was weighed and dispersed in PC under sonication for 4 hours respectively. Then the dispersions were mixed and sonicated for one more hour. The mixture was then moved to an aluminum foil bowl and dried under vacuum.

Different measurement methods were applied to understand the structural and energetic properties of the obtained $rGO/Al/Bi_2O_3$ gel, including SEM-EDS, Zeta potential, DLS, XRD, Raman, BET surface area, DSC-TGA, ESD sensitivity and linear combustion propagation test.

2.4. Structural analysis of $rGO/Al/Bi_2O_3$

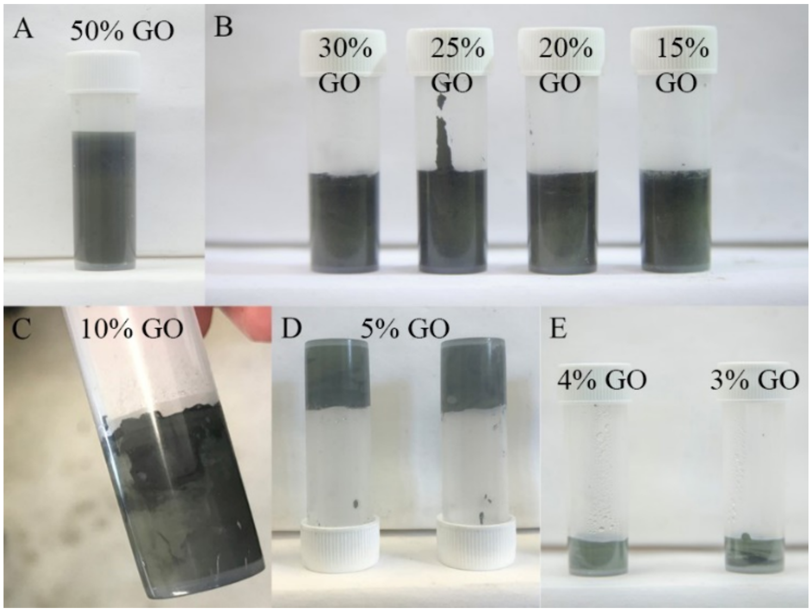

Figure 2.8 Optical Pictures of the formed gels with different GO percentage.

Our gelation method in PC allows for precise control of GO content (Figure 2.8). Maintaining a GO concentration of 10 mg / mL in GO/Al/Bi_2O_3 mixture allowed the formation of final product from containing GO between different mass percentage, from 3% to 50%. More GO provided better structural strength, while less GO contributed less dead mass in the final gel. If not specified, the sample discussed here had a GO mass percentage of 5%.

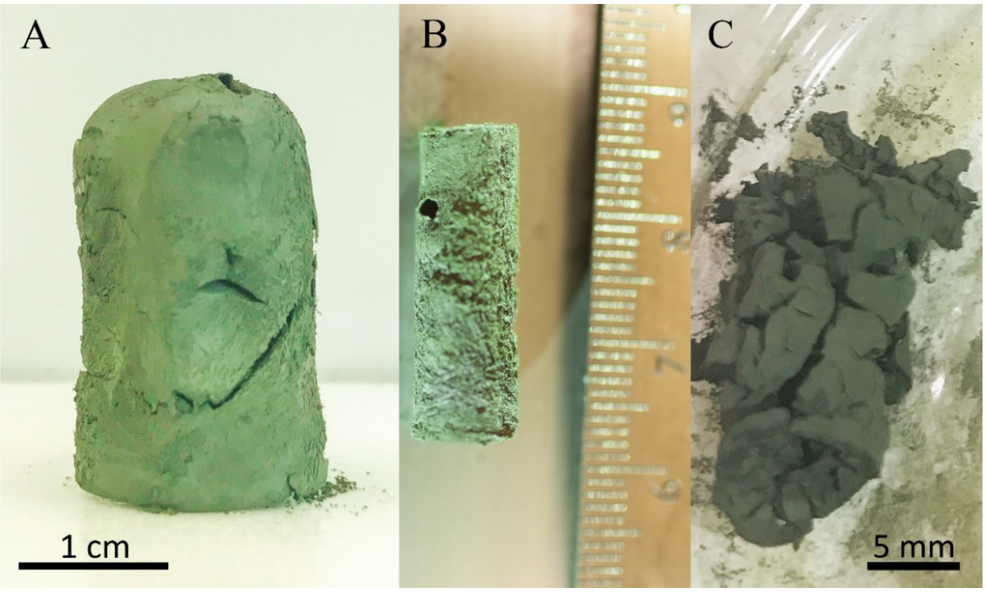

Figure 2.9 Optical picture of freeze dried rGO(5%)/Al/Bi_2O_3 gel formed in vial (A) and glass tube (B, ruler in cm), and vacuum dried gel (C).

The sample size and shape were well-preserved after freeze drying, while the sample being vacuum dried broke during the drying, as shown in Figure 2.9. The fast removal of solvent during vacuum drying without structural support cause the collapse of the gel. Conversely, freeze-drying occurred in a much slower rate and the frozen solvent helped to support the structure during the removal of solvent. Therefore, most samples were freeze dried in this research. The synthesis was similar to a molding process in which the dried gel took the shape of the container. The finished gel was homogeneous in color, indicating well dispersed Al and Bi_2O_3 NPs throughout the structure, indicative of a well-dispersed precursor mixture formed before the onset of gelation process (Figure 2.7). The mass density of the gel varied from 20 to 250 mg / cm^3, depending on the percentage of GO in the reactant. Importantly, phase separation between Al and Bi_2O_3 NPs was minimized, overcoming a significant shortcoming of Al/Bi_2O_3 nanothermite produced by conventional sonication and drying. [48] Uniform dispersion of particles and their stability were confirmed by zeta potential tests (Table 2.2) and dynamic light scattering (DLS) (Figure 2.10), respectively. GO, Al and Bi_2O_3 dispersions all measured high negative surface charge with particle sizes indicative of single or few-particle clusters. Achieving a surface charge of similar polarity for all particles is critical, as agglomeration and settling of the mixed products was avoided. The 16-hours resting procedure played a key role for the well-dispersion of nanoparticles. During the resting process, the repulsion force helped to obtain a homogeneous mixture of exfoliated GO sheets, Al nanoparticles and Bi_2O_3 nanoparticles. During the gelling process, the dispersed GO sheets got reduced and trapped the surrounding nanoparticles locally. It was observed that Bi_2O_3 would agglomerate and precipitate out if the gelling process was initiated immediately after preparing the GO/Al/Bi_2O_3 mixture.

Table 2.2 Zeta potential results for all the precursors in PC.

Material	Zeta Potential
Graphene Oxide	-38.75 ± 2.25 mV
Al NPs	-45.14 ± 3.10 mV
Bi_2O_3	-20.10 ± 0.53 mV

A few hours of resting before the addition of EDA was found critical to the success of the synthesis process. If the EDA was injected into the mixture immediately after the mixing and 10-minute vortexing of GO/Al/Bi_2O_3 mixture, a yellow layer of Bi_2O_3 precipitation was found to occur. No experiment was carried out to determine the structure of the precipitation, but it is hypothesized that the nitrogen in EDA played a role as a ligand for Bi in Bi_2O_3 nanoparticles, [49] leading to the agglomeration and precipitation of Bi_2O_3 nanoparticles from some concentrated area in the mixture. However, when the mixture was rested for a few hours, the Brownian movement of the GO nanosheets and Al, Bi_2O_3 nanoparticles resulted in a homogeneously distribution of all components in the mixture. Therefore, the Bi_2O_3 agglomeration did not precipitate after the addition of EDA. Experiments of samples with different resting time between 4 – 48 hours were carried out. The mixture with resting time between 8 – 48 hours gave the similar energy release, larger than the number given by the 4-hour resting sample, as shown in Table 2.3. Considering the time of experiment, 16 hours was finally chosen as the resting period.

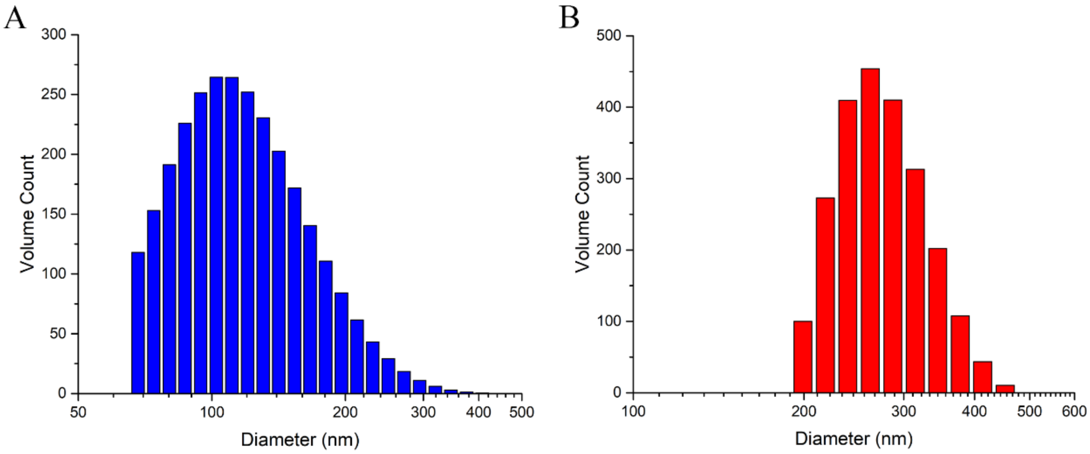

Figure 2.10 DLS results of Al NPs (A) and Bi_2O_3 (B) in PC.

Table 2.3 Energy release of dried GO/Al/Bi_2O_3 mixture in PC with different resting period.

Resting time	4 hours	8 hours	16 hours	32 hours	48 hours
Energy release	681 J/g	733 J/g	734 J/g	728 J/g	731 J/g

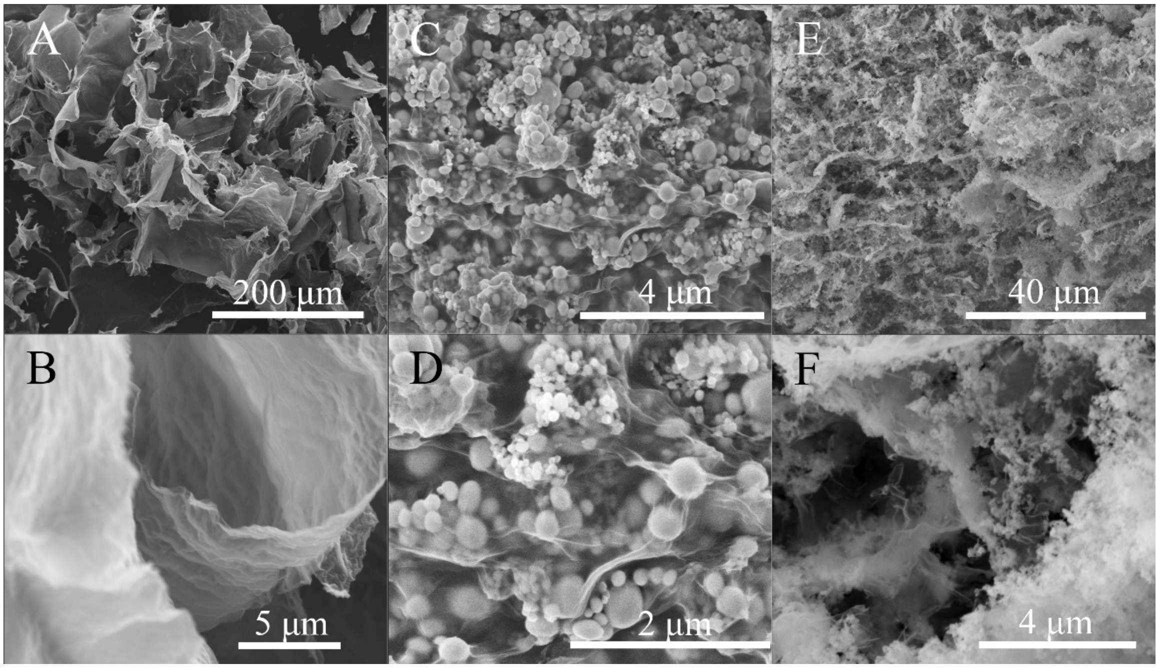

Figure 2.11 SEM images of freeze-dried pure rGO gel (A, B), rGO/Al/Bi2O3 gel before (C, D) and after (E, F) slow heating to 1200 ℃.

SEM images displaying the microstructure of the aerogel before and after slow heating to 1200 °C in argon (within DSC-TGA) are shown in Figure 2.11. The rGO prepared without particle loading showed porosity on the order of tens of microns (Figure 2.11A-B), similar to rGO gels prepared with water. [12] The gelation processes occurred due to the crosslinking and π-π stacking between the reduced GO sheets, producing thin-walled rGO porous scaffolds. [30, 38, 50] rGO structures loaded with nanoscale fuel and oxidizer particles are shown in Figure 2.11C-D. Smaller Al NPs (~80 nm) and larger Bi_2O_3

NPs (~200 nm) could be clearly distinguished individually, wrapped by rGO sheets. Particle agglomeration and phase separation of the NPs was not observed. The homogeneous mixing was also confirmed by EDS mapping (Figure 2.12, Table 2.4).

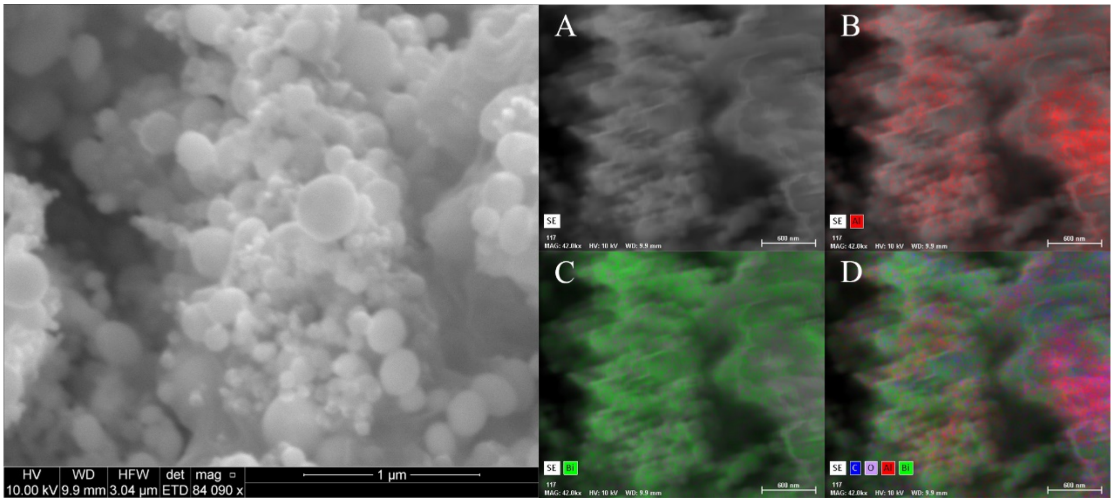

Figure 2.12 EDS mapping of rGO/Al/Bi2O3 macrogel.

Table 2.4 Elemental statistics calculated from EDS of Figure 2.12

Element	Mass percentage	Atom percentage
Carbon	2.63	11.89
Oxygen	8.27	28.12
Aluminum	20.97	42.26
Bismuth	68.13	17.72

Discrete fuel and oxidizer particles are no longer observed after being heated to 1200 ℃. Rather, a porous Al_2O_3 framework intermixed with graphene sheets was produced during the reaction (Figure 2.11E-F). Note that some Bi content evaporated during DSC-TGA heating due to its high vapor pressure when the temperature is above 1000 ℃. [51] EDS mapping (Figure 2.13, Table 2.5) confirms that the atomic percentage of bismuth dropped from 17.72% to 0.08% after slow heating while the relative content of carbon and aluminum were only slightly altered.

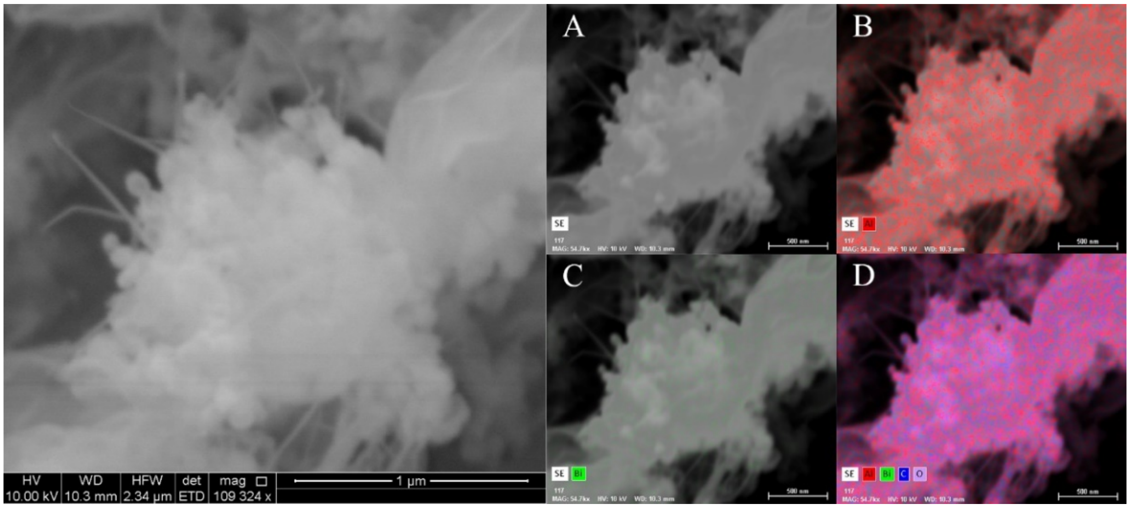

Figure 2.13 EDS mapping of rGO/Al/Bi_2O_3 after slow heating to 1000°C.

Table 2.5 Elemental statistics calculated from EDS of Figure 2.13.

Element	Mass percentage / %	Atom percentage / %
Carbon	6.18	10.12
Oxygen	44.28	54.38
Aluminum	48.64	35.42
Bismuth	0.89	0.08

The occurrence of a high-temperature thermite reaction was confirmed by XRD results (Figure 2.14), which showed the emergence of α-Al_2O_3 produced during the Al-Bi_2O_3 reaction. The specific surface area of the freeze-dried rGO gel without Al and Bi_2O_3 NPs, measured by BET, was 32.49 m^2/g, which is lower than some values reported [17] due to the thick rGO sheets form from stacking, as shown in Figure 2.11C. While the rGO/Al/Bi_2O_3 aerogel was 34.31 m^2/g despite only 5 % GO content (Figure 2.15, Table

2.6). The increased surface area suggests that large-scale particle agglomeration was avoided during the gelation process, as confirmed by SEM.

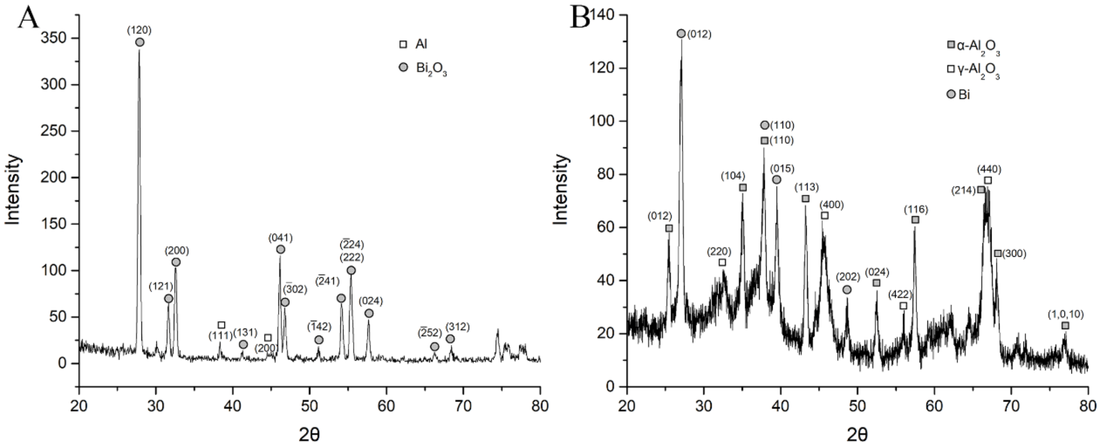

Figure 2.14 XRD pattern of rGO/Al/ Bi_2O_3 before (A) and after (B) slow heating up to 1200°C.

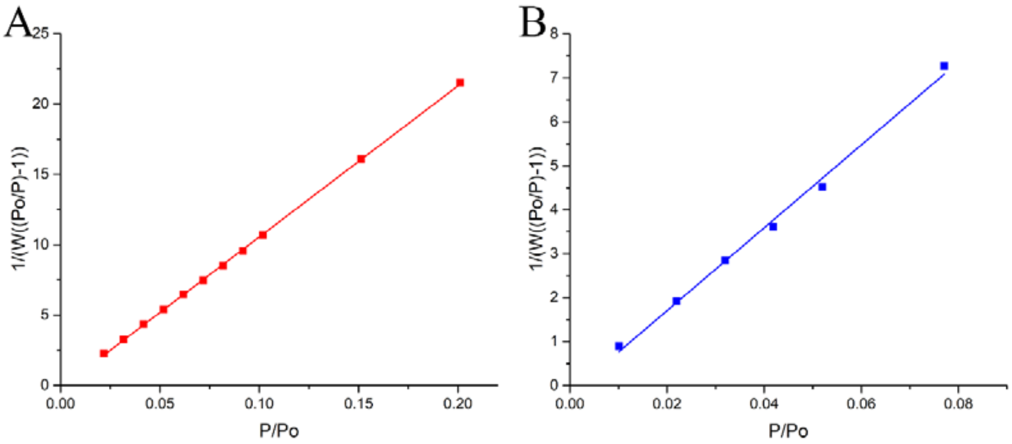

Figure 2.15 BET nitrogen absorption results of pure rGO gel (A) and rGO/Al/ Bi_2O_3 gel (B).

Table 2.6 Specific surface area results measured by BET. The surface area of Bi_2O_3 is provided by manufacture.

Material	Pure rGO gel	Al NPs (80 nm)	Bi_2O_3 NPs	RGO/Al/Bi_2O_3
Surface Area	32.49 m^2/g	25 m^2/g	3.5 m^2/g	34.31 m^2/g

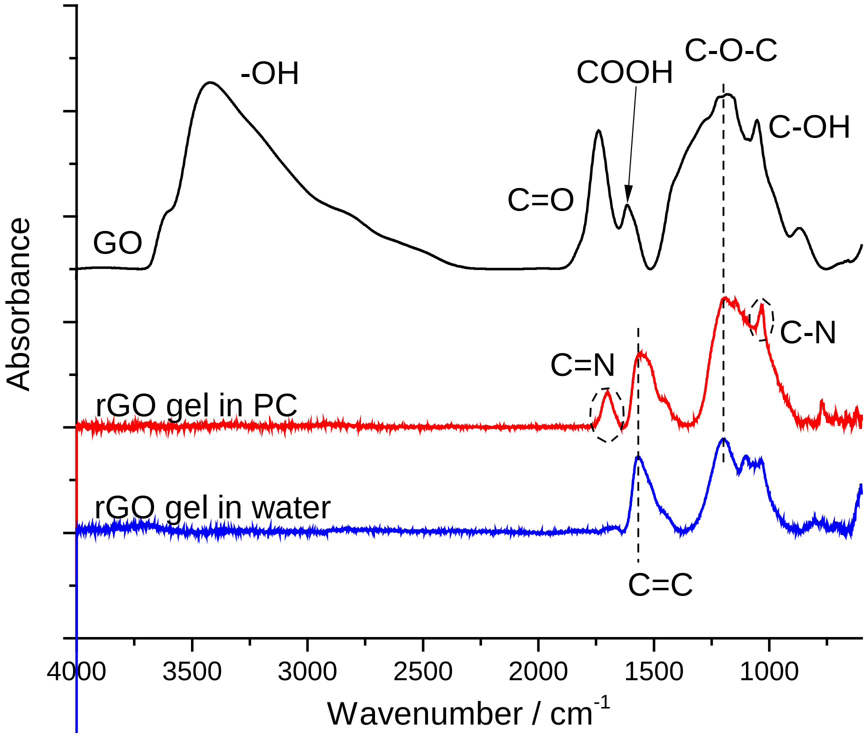

Figure 2.16 FTIR spectra of rGO gels formed in water and PC.

FTIR spectra, shown in Figure 2.16, confirmed that nitrogen functional groups supplied by EDA were responsible for promoting gelation. Peaks assigned to -OH, C=O and -COOH were disappeared, indicating these functional groups were removed after reduction. A peak at 1700 cm^{-1} was present in the gel formed in PC as a result of the carbon-nitrogen double bond. This peak was not present in the gel formed in water. This peak indicated that the C=N bond formed more often in PC than in water, due to the reaction between EDA and the carboxyl group in the basal plane of GO. The peak at 1030 cm^{-1} was resulted from the C-N bond in EDA. The reaction between the C=O group and EDA formed Schiff base in both sides of EDA, connecting the GO sheets. Therefore, EDA acted as both a reducer and a linking agent during the reaction and existed in the final gel. Raman spectrum confirmed the reduction of GO to rGO since the I_D/I_G increased from 1.095 for

GO to 1.239 for rGO gel (Figure 2.17). The gelation process started upon introduction of EDA into the system at room temperature, unlike gelation processes in water that requires heating. For the synthesis in PC, conducting the reaction at 95 °C accelerated the reaction significantly while retaining the chemical reactivity of Al and Bi_2O_3. Considering the negative surface charge for all the well-dispersed GO, Al, and Bi_2O_3 precursors, a homogeneous mixture was formed before the gelation process, as confirmed by images obtained 16 hours of dispersion (Figure 2.7). When EDA was injected into the PC dispersion, the reaction occurred, and the gel formed. The mechanism is shown schematically in Figure 2.18.

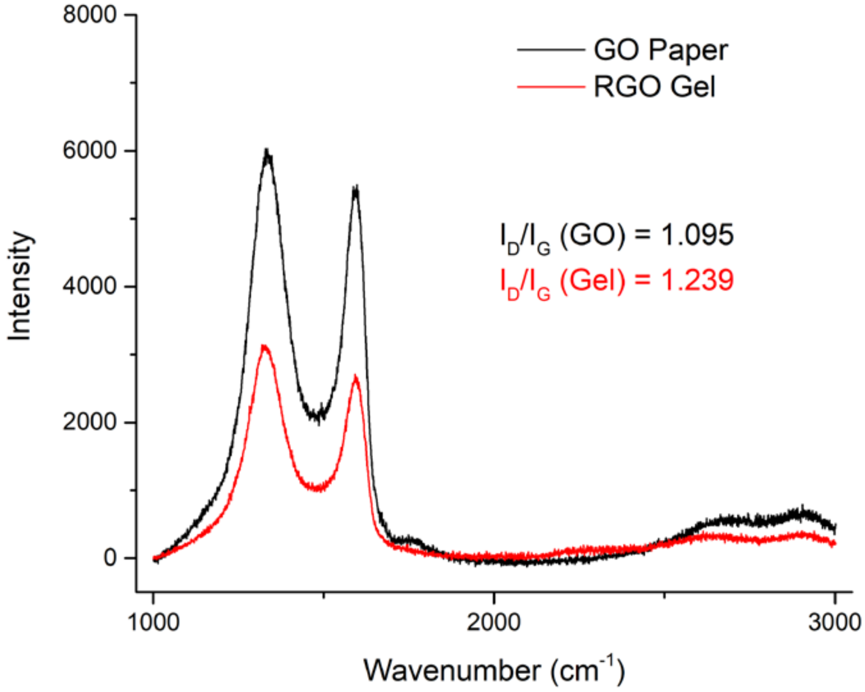

Figure 2.17 Raman spectrum of GO and rGO gel.

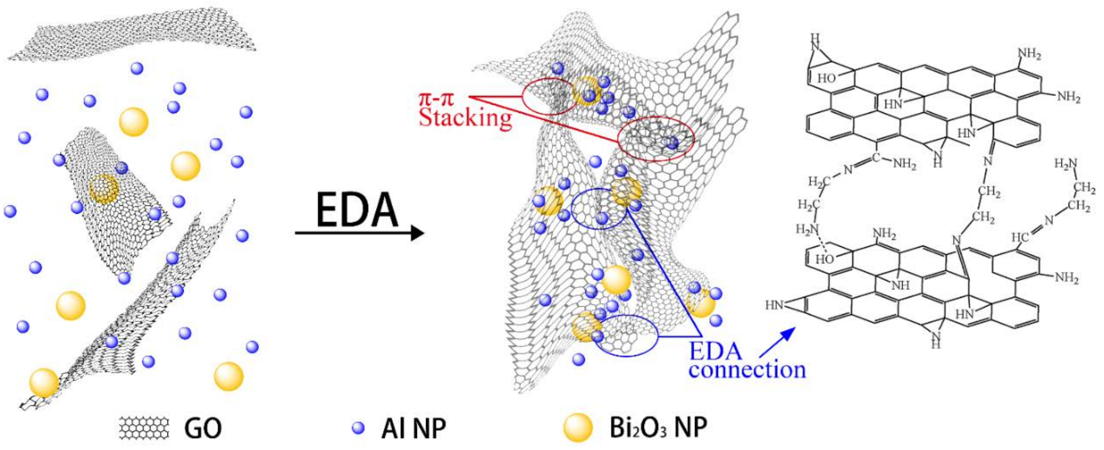

Figure 2.18 Formation mechanism of rGO/Al/Bi_2O_3 gel. EDA refers to ethylenediamine.

2.5. Energetic analysis of rGO/Al/Bi_2O_3

Simultaneous differential scanning calorimetry and thermogravimetric analysis (DSC-TGA) was conducted to examine the energetic properties of the rGO/Al/Bi_2O_3 gel. Two separate control Al/Bi_2O_3 samples (Φ=1.4, without rGO) were prepared using PC in one case and IPA in another. An additional sample was synthesized by drying a dispersion of GO/Al/Bi_2O_3 prior to gelation. Energy release of the samples was quite different and directly related to the composite morphology produced during assembly. Figure 2.19 shows that the Al/Bi_2O_3 control sample made in IPA produced an energy release of 723 J/g. The control sample made in PC showed visible phase separation upon drying, with yellow Bi_2O_3 precipitating to the bottom of the sample. This phase-separated sample produced an energy release of 638 J/g, with about a third of the energy released after the melting of Bi_2O_3 at 817°C, indicating the reaction could not occur well until both Al and Bi_2O_3 melted and freely flew throughout the sample. Introducing GO produced a homogeneous material without phase separation. Considering the negative surface charge of GO, Al and Bi_2O_3, the phase separation between Al and Bi_2O_3 in PC after drying was prevented. The dried GO/Al/Bi_2O_3 mixture that did not undergo gelation produced an energy release of 734 J/g. This energy release was slightly higher than the Al/Bi_2O_3 control sample made in IPA due to the reduced phase separation. The rGO/Al/Bi_2O_3 aerogel produced the highest energy release of 909 J/g, indicating that it possessed the best intermixing between Al and Bi_2O_3 particles among all the samples. As seen from the SEM images, Al and Bi_2O_3 NPs assembled between rGO sheets during the gelation process, enhancing the interfacial contact between fuel and oxidizer particles. However, the vacuum dried gel only provided an energy release of 609 J/g, much smaller than the freeze-dried sample, indicating the dense structure after vacuum drying significantly prevented the reaction between Al and Bi_2O_3 nanoparticles.

Condensed phase reactions between Al and Bi_2O_3 particles produced the greatest energy release for all samples, excluding the phase-separated control sample formed in PC. These reactions occurred prior to Al melting at 665 °C, indicated by an endothermic peak in each curve. Note that liquid-phase Al – Bi_2O_3 reaction [52, 53] accounted for less than 10% of the energy released within the aerogel but was responsible for a greater percentage of the energy released for other compositions. Enhancement of the condensed phase reaction between Al and Bi_2O_3 particles was facilitated by increased interfacial contact and homogeneous mixing. These conditions promoted decreased diffusion lengths between mobile of Al atoms that diffuse through the Al_2O_3 shell. [54] Furthermore, the temperature associated with the peak energy release decreased from 600 °C for the IPA control sample without graphene to approximately 560 °C for the samples self-assembled on RGO. Within the self-assembled rGO composites, Al and Bi_2O_3 NPs are embedded between rGO sheets, reducing the effects of Al NP sintering [48] and enhancing energy release at lower temperatures. rGO/Al/Bi_2O_3 aerogels produced with different equivalence ratios were also analyzed by DSC-TGA and are displayed in Figure 2.20. The sample with an equivalence ratio of 1.4 (fuel rich) showed the highest energy release, which is consistent with self-assembled GO/Al/Bi_2O_3 or Al/MoO_3 nanothermite. [42, 52] Note that the strongest endothermic peak at 665 °C associated with melting of unreacted Al occurred at $\Phi = 1.6$, indicating that the fuel mixture ratio for optimum reaction was exceeded. Energy release increased with equivalence ratios prior to $\Phi = 1.6$.

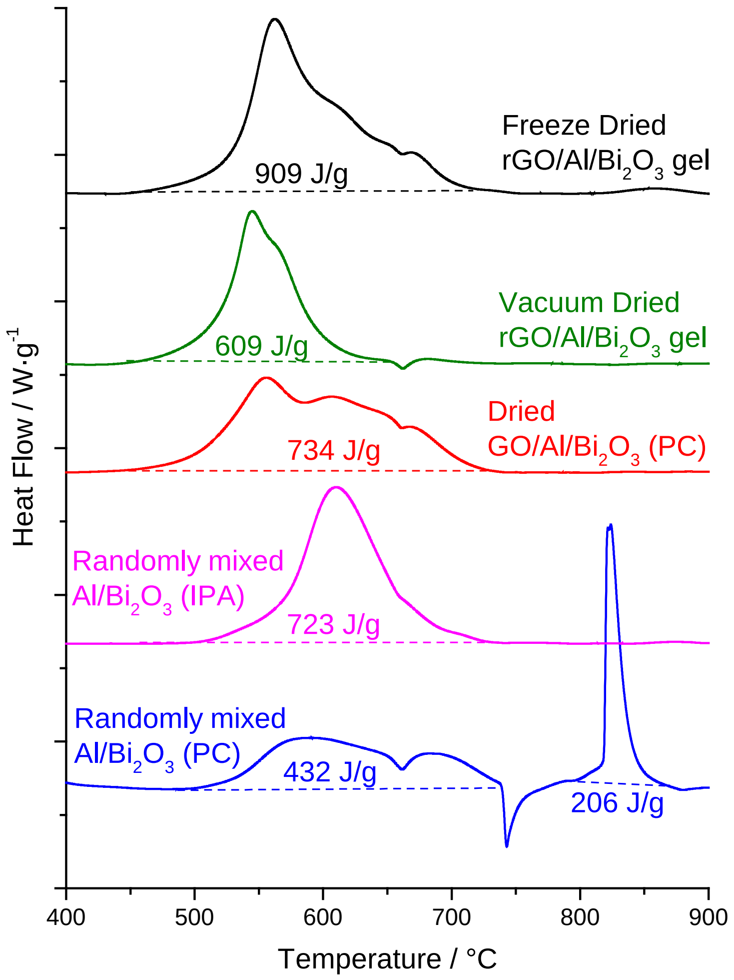

Figure 2.19 DSC curves of Al/Bi_2O_3control samples made in PC and IPA, dried rGO/Al/Bi_2O_3 dispersion before gelation and freeze-dried rGO/Al/Bi_2O_3.

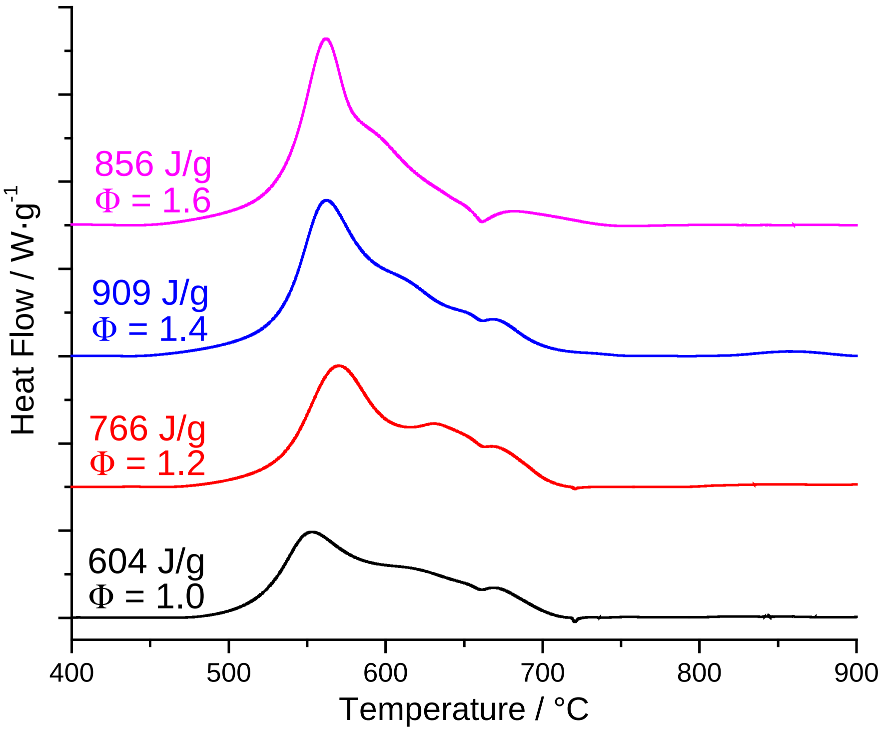

Figure 2.20 DSC curves of freeze-dried rGO/Al/Bi_2O_3 with different equivalence ratios.

The burn rate of the energetic graphene aerogel (5% GO in mass, Φ = 1.4) was examined using a high speed camera in an open burn chamber. [55] Figure 2.21 shows key frames obtained by a high-speed camera imaging at 100,000 fps. The frame at the time of ignition was set to t = 0. The combustion front propagated across the entire 23-mm nanothermite aerogel between the frames obtained at 0.020 – 0.030 ms, translating to a flame propagation speed of 960 ± 190 m/s. The accuracy of the flame speed was limited by the frame acquisition rate of fast camera. This value was much higher than the open burning speed for Al/Bi_2O_3 nanothermite powder as measured by Sanders *et al.*, which gave a maximum 425 m/s open burning rate at Φ = 1.3 among Φ =0.8, 1.0, 1.3, 1.6 and 1.8. [7] An open burn control experiment was also performed using a similar sized and weighed sample of Al/Bi_2O_3 (Φ = 1.4) nanothermite powder made in IPA. The key frames are shown in Figure 2.22. The powder exhibited a flame propagation speed around 460 m/s, which is quite close to the value found by Sanders, but still much lower than the propagation speed of the gel.

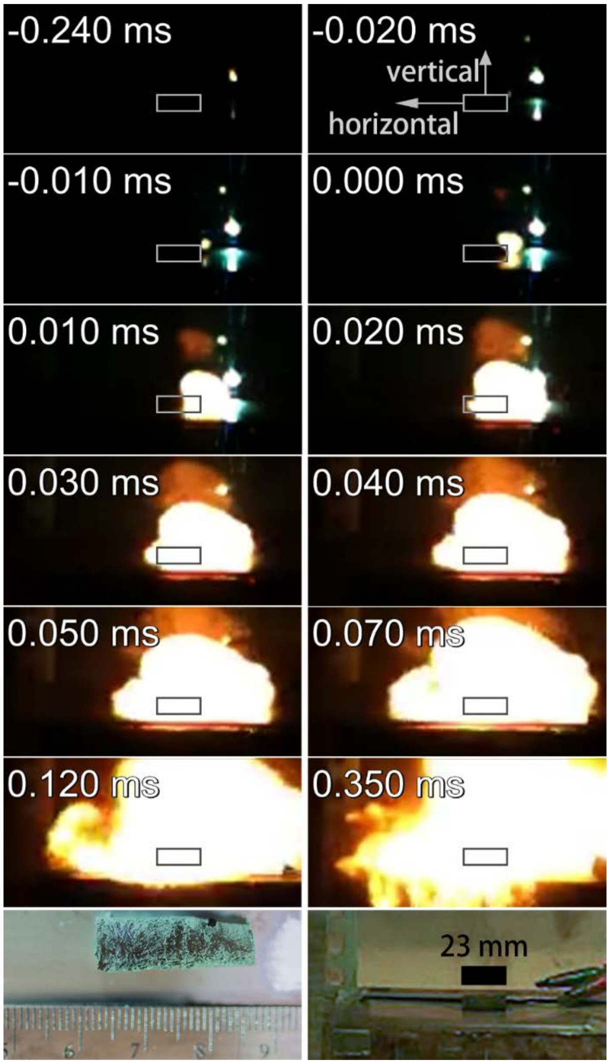

Figure 2.21 High-speed camera frames of the open burn of rGO/Al/Bi_2O_3 nanothermite aerogel, the rectangles in each frame indicates the position of the aerogel.

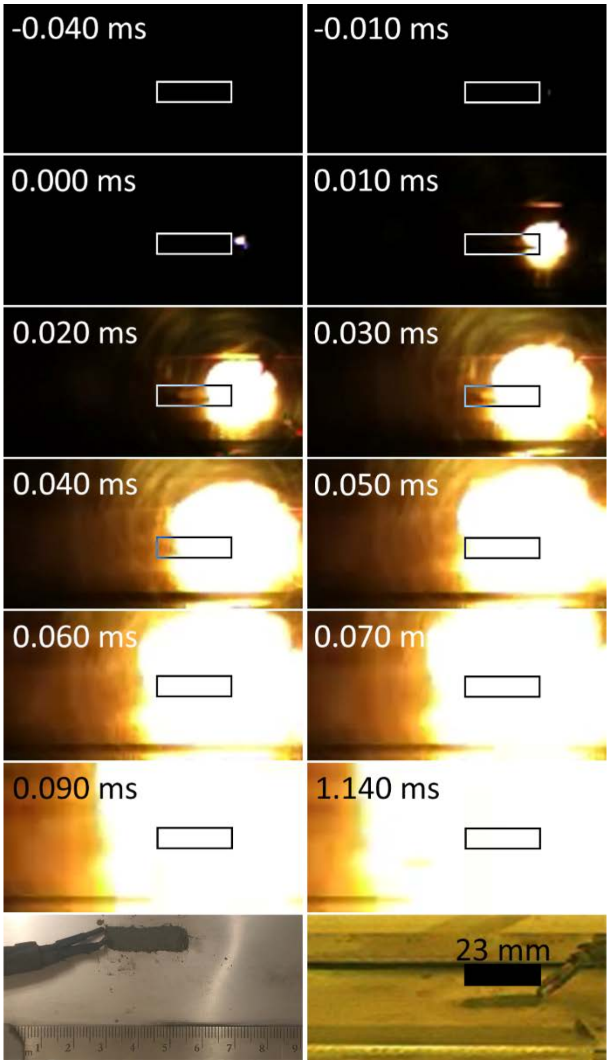

Figure 2.22 Key frames of the open burn of control Al/Bi_2O_3 nanothermite powder made in IPA.

Experiments performed by Plantier et al. [56] suggested that open burns produce flame propagation rates that are approximately one third those produced for confined burn experiments using identical chemical compositions. Open burn experiments allowed the combustion energy and shock wave to propagate out in a 3D space, resulting in a decaying wave similar to a Taylor-Sedov blast wave. [57, 58] Compared to a neat Al/Bi_2O_3 control sample, the greatly enhanced burn rate of the $rGO/Al/Bi_2O_3$ aerogel was likely a result of both enhanced overall energy release and the porosity afforded by the internal aerogel structure. Internal pores allowed the hot combustion products to become entrained behind shock waves propagating through the multiphase material. The propagating gases preheated the material ahead of the initial reaction while shock wave focusing may lead to "hot spot" formation within the rGO scaffold. [59] The porous rGO aerogel itself might lead to a "self-confining reaction" within the rGO scaffold, leading to a mixture of both non-confined and confined burning characteristics. This was evident by the rapid flame propagation down the horizontal axis of the sample (right to left in Figure 4) compared to slower vertical, open air flame propagation, forming a "rectangular" flame shape. However, in the combustion of neat Al/Bi_2O_3 powder, the flame expanded from the ignition point more spherically in all directions, showing no apparent preferential direction. Therefore, the self-confinement of the rGO/Al/Bi_2O_3 led to a more restricted energy release in and along its dimensions and limited the blast ejection of energetic material which likely occurred for the nanothermite powder control case.

Table 2.7 Mass and Atomic percentage of rGO gel.

Element	Mass Percentage	Atom Percentage
Carbon	62.39%	68.25%
Nitrogen	7.29%	6.84%
Oxygen	30.33%	24.91%

The minimum ESD energy threshold for the rGO/Al/Bi_2O_3 gel was 0.89 mJ, measured by electrostatic discharging system including a capacitor charged to a high voltage, a discharging tip and a steel sample holder with samples in a plastic ring. This value is more than 3 orders higher than the value of Al/Bi_2O_3 nanothermite (0.125 μJ) as reported by Puszynski *et al.* [10] It was also found that the EDA chemical reduction of GO to rGO is incomplete, [12] as the C/O ratio was only increased from 1.95 in GO [14] to 2.74 in the pure rGO gel, limiting the electrical conductivity of the composite. Further reduction may result in still greater ESD thresholds.

2.6. Conclusion and future direction

rGO was successfully utilized as the scaffold for rGO/Al/Bi_2O_3 3D macroscale energetic aerogel with superior energy release, flame speed, and ESD sensitivity relative to the neat NP mixture. A novel gelation process in which EDA was added to a PC dispersion to induce gelation and mild chemical reduction was discovered. Particle dispersion was encouraged in PC, while EDA served as a mild gelation and reduction agent that retained the reactivity of the energetic NPs. The achieved rGO/Al/Bi_2O_3 nanoenergetic aerogel obtained by this process exhibited structural homogeneity with well-dispersed particle loading. The aerogel scaffold was of critical importance from applications' perspectives as it confined fuel and oxide NPs in intimate contact, linked to the NPs to discourage sintering, provided an electrically conductive pathway to reduce ESD sensitivity, and provided a mechanism that tends to partially confine flame propagation for enhanced burn rates. It provided a safe way to produce, store and use nanothermite material with designable shape and enhanced energetic performance.

The process was demonstrated using embedded Al and Bi_2O_3 NPs. However, it can be extended to produce aerogels with numerous other types of embedded reactive nanoparticles, nanorods and nanosheets to obtain different nanothermite responses and different structural properties, such as CuO, MoO_3 and Fe_2O_3. The process was also amenable for the gelation that are sensitive to high temperature or water. Different graphene gels with loading of nanoparticles utilized in various fields such as catalysts, electrochemical devices or medical devices can be synthesized using this method.

2.7. Summary

The target of this part of the research is to obtain a self-standing macroscale nanoenergetic structure with improved safety in handling, which was successfully achieved. The difficulties I faced during the research were the design and the optimization of the process. The methods developed and reported by other researchers usually do not meet all requirements of my own research. Therefore, it is important to find out the theory of the reaction and try to develop and optimize a new route based on the theory. There are still some relations in this research that is not cleared. How does the amount ratio of EDA/GO interfere with the mechanical and energetic properties of the final gel product? How important is the porosity in the final gel to the combustion rate of the final gel product? These problems need to be further investigated to build a better comprehension of this method and the macroscale nanoenergetic gel.

2.8. References

[1] D. Stamatis, X. Zhu, M. Schoenitz, E. L. Dreizin, and P. Redner, "Consolidation and mechanical properties of reactive nanocomposite powders," *Powder Technology,* vol. 208, no. 3, pp. 637-642, 2011/04/10/ 2011.

[2] S. J. Apperson *et al.*, "Characterization of Nanothermite Material for Solid-Fuel Microthruster Applications," *Journal of Propulsion and Power,* vol. 25, no. 5, pp. 1086-1091, 2009/09/01 2009.

[3] M. M. Durban, A. M. Golobic, E. V. Bukovsky, A. E. Gash, and K. T. Sullivan, "Development and Characterization of 3D Printable Thermite Component Materials," *Advanced Materials Technologies,* vol. 3, no. 12, p. 1800120, 2018.

[4] K. T. Sullivan *et al.*, "Controlling Material Reactivity Using Architecture," *Advanced Materials,* vol. 28, no. 10, pp. 1934-1939, 2016.

[5] J. A. Hammons, W. Wang, J. Ilavsky, M. L. Pantoya, B. L. Weeks, and M. W. Vaughn, "Small angle X-ray scattering analysis of the effect of cold compaction of Al/MoO3 thermite composites," *Physical Chemistry Chemical Physics,* 10.1039/B711456G vol. 10, no. 1, pp. 193-199, 2008.

[6] J. Shen *et al.*, "Combustion of 3D printed 90 wt% loading reinforced nanothermite," *Combustion and Flame,* vol. 215, pp. 86-92, 2020/05/01/ 2020.

[7] V. E. Sanders, B. W. Asay, T. J. Foley, B. C. Tappan, A. N. Pacheco, and S. F. Son, "Reaction Propagation of Four Nanoscale Energetic Composites (Al/MoO3, Al/WO3, Al/CuO, and Bi2O3)," *Journal of Propulsion and Power,* vol. 23, no. 4, pp. 707-714, 2007/07/01 2007.

[8] *NATO Standardization Agreement (STANAG) on Explosives, Impact Sensitivity Tests, No. 4489, Ed. 1,* 1999.

[9] M. Comet, B. Siegert, F. Schnell, V. Pichot, F. Ciszek, and D. Spitzer, "Phosphorus-Based Nanothermites: A New Generation of Pyrotechnics Illustrated by the Example of n-CuO/Red P Mixtures," *Propellants, Explosives, Pyrotechnics,* vol. 35, no. 3, pp. 220-225, 2010.

[10] J. A. Puszynski, C. J. Bulian, and J. J. Swiatkiewicz, "Processing and Ignition Characteristics of Aluminum-Bismuth Trioxide Nanothermite System," *Journal of Propulsion and Power,* vol. 23, no. 4, pp. 698-706, 2007/07/01 2007.

[11] A. K. Geim and K. S. Novoselov, "The rise of graphene," (in English), *Nature Materials,* Article vol. 6, no. 3, pp. 183-191, Mar 2007.

[12] H. Hu, Z. Zhao, W. Wan, Y. Gogotsi, and J. Qiu, "Ultralight and Highly Compressible Graphene Aerogels," *Advanced Materials,* vol. 25, no. 15, pp. 2219-2223, 2013.

[13] J. Li *et al.*, "Ultra-light, compressible and fire-resistant graphene aerogel as a highly efficient and recyclable absorbent for organic liquids," *Journal of Materials Chemistry A,* 10.1039/C3TA14725H vol. 2, no. 9, pp. 2934-2941, 2014.

[14] X. Zhang *et al.*, "Mechanically strong and highly conductive graphene aerogel and its use as electrodes for electrochemical power sources," *Journal of Materials Chemistry,* 10.1039/C1JM10239G vol. 21, no. 18, pp. 6494-6497, 2011.

[15] M. A. Worsley, P. J. Pauzauskie, T. Y. Olson, J. Biener, J. H. Satcher, and T. F. Baumann, "Synthesis of Graphene Aerogel with High Electrical Conductivity," *Journal of the American Chemical Society,* vol. 132, no. 40, pp. 14067-14069, 2010/10/13 2010.

[16] P. Lv, X.-W. Tan, K.-H. Yu, R.-L. Zheng, J.-J. Zheng, and W. Wei, "Super-elastic graphene/carbon nanotube aerogel: A novel thermal interface material with highly thermal transport properties," *Carbon,* vol. 99, pp. 222-228, 2016/04/01/ 2016.

[17] M. A. Worsley *et al.*, "Mechanically robust 3D graphene macroassembly with high surface area," *Chemical Communications,* 10.1039/C2CC33979J vol. 48, no. 67, pp. 8428-8430, 2012.

[18] Y. Q. Sun, Q. Wu, and G. Q. Shi, "Supercapacitors based on self-assembled graphene organogel," (in English), *Physical Chemistry Chemical Physics,* Article vol. 13, no. 38, pp. 17249-17254, 2011.

[19] Y. X. Xu, G. Q. Shi, and X. F. Duan, "Self-Assembled Three-Dimensional Graphene Macrostructures: Synthesis and Applications in Supercapacitors," *Accounts of Chemical Research,* vol. 48, no. 6, pp. 1666-1675, Jun 2015.

[20] H. Long *et al.*, "High Surface Area MoS2/Graphene Hybrid Aerogel for Ultrasensitive NO2 Detection," *Advanced Functional Materials,* vol. 26, no. 28, pp. 5158-5165, 2016.

[21] L. Li, S. He, M. Liu, C. Zhang, and W. Chen, "Three-Dimensional Mesoporous Graphene Aerogel-Supported SnO2 Nanocrystals for High-Performance NO2 Gas Sensing at Low Temperature," *Analytical Chemistry,* vol. 87, no. 3, pp. 1638-1645, 2015/02/03 2015.

[22] M. Lu *et al.*, "Graphene Aerogel–Metal–Organic Framework-Based Electrochemical Method for Simultaneous Detection of Multiple Heavy-Metal Ions," *Analytical Chemistry,* vol. 91, no. 1, pp. 888-895, 2019/01/02 2019.

[23] G. Zhou, E. Paek, G. S. Hwang, and A. Manthiram, "High-Performance Lithium-Sulfur Batteries with a Self-Supported, 3D Li2S-Doped Graphene Aerogel Cathodes," *Advanced Energy Materials,* vol. 6, no. 2, p. 1501355, 2016/01/01 2016.

[24] J. Meng, Y. Cao, Y. Suo, Y. Liu, J. Zhang, and X. Zheng, "Facile Fabrication of 3D SiO2@Graphene Aerogel Composites as Anode Material for Lithium Ion Batteries," *Electrochimica Acta*, vol. 176, pp. 1001-1009, 2015/09/10/ 2015.

[25] Y. Xie, Z. Meng, T. Cai, and W.-Q. Han, "Effect of Boron-Doping on the Graphene Aerogel Used as Cathode for the Lithium–Sulfur Battery," *ACS Applied Materials & Interfaces,* vol. 7, no. 45, pp. 25202-25210, 2015/11/18 2015.

[26] B. Wang, W. Al Abdulla, D. Wang, and X. S. Zhao, "A three-dimensional porous LiFePO4 cathode material modified with a nitrogen-doped graphene aerogel for high-power lithium ion batteries," *Energy & Environmental Science,* 10.1039/C4EE03825H vol. 8, no. 3, pp. 869-875, 2015.

[27] Z. Chen, W. Ren, L. Gao, B. Liu, S. Pei, and H.-M. Cheng, "Three-dimensional flexible and conductive interconnected graphene networks grown by chemical vapour deposition," *Nature Materials,* vol. 10, no. 6, pp. 424-428, 2011/06/01 2011.

[28] J.-C. Yoon, J.-S. Lee, S.-I. Kim, K.-H. Kim, and J.-H. Jang, "Three-Dimensional Graphene Nano-Networks with High Quality and Mass Production Capability via Precursor-Assisted Chemical Vapor Deposition," *Scientific Reports,* vol. 3, no. 1, p. 1788, 2013/05/07 2013.

[29] C. Zhu *et al.*, "Highly compressible 3D periodic graphene aerogel microlattices," *Nature Communications,* vol. 6, no. 1, p. 6962, 2015/04/22 2015.

[30] Y. X. Xu, K. X. Sheng, C. Li, and G. Q. Shi, "Self-Assembled Graphene Hydrogel via a One-Step Hydrothermal Process," *Acs Nano,* vol. 4, no. 7, pp. 4324-4330, Jul 2010.

[31] H. Bi *et al.*, "Low Temperature Casting of Graphene with High Compressive Strength," *Advanced Materials,* vol. 24, no. 37, pp. 5124-5129, 2012/09/25 2012.

[32] J. Zhao, W. Ren, and H.-M. Cheng, "Graphene sponge for efficient and repeatable adsorption and desorption of water contaminations," *Journal of Materials Chemistry,* 10.1039/C2JM34128J vol. 22, no. 38, pp. 20197-20202, 2012.

[33] H. Bai, C. Li, X. Wang, and G. Shi, "A pH-sensitive graphene oxide composite hydrogel," *Chemical Communications,* 10.1039/C000051E vol. 46, no. 14, pp. 2376-2378, 2010.

[34] Z. Han, Z. Tang, P. Li, G. Yang, Q. Zheng, and J. Yang, "Ammonia solution strengthened three-dimensional macro-porous graphene aerogel," *Nanoscale,* 10.1039/C3NR00971H vol. 5, no. 12, pp. 5462-5467, 2013.

[35] H.-P. Cong, X.-C. Ren, P. Wang, and S.-H. Yu, "Macroscopic Multifunctional Graphene-Based Hydrogels and Aerogels by a Metal Ion Induced Self-Assembly Process," *ACS Nano,* vol. 6, no. 3, pp. 2693-2703, 2012/03/27 2012.

[36] H. Sun, Z. Xu, and C. Gao, "Multifunctional, Ultra-Flyweight, Synergistically Assembled Carbon Aerogels," *Advanced Materials*, vol. 25, no. 18, pp. 2554-2560, 2013.

[37] M. A. Worsley *et al.*, "High Surface Area, sp2-Cross-Linked Three-Dimensional Graphene Monoliths," *The Journal of Physical Chemistry Letters*, vol. 2, no. 8, pp. 921-925, 2011/04/21 2011.

[38] P. Chen *et al.*, "Hydrothermal synthesis of macroscopic nitrogen-doped graphene hydrogels for ultrafast supercapacitor," *Nano Energy*, vol. 2, no. 2, pp. 249-256, 2013/03/01/ 2013.

[39] H. L. Wang, J. T. Robinson, X. L. Li, and H. J. Dai, "Solvothermal Reduction of Chemically Exfoliated Graphene Sheets," *Journal of the American Chemical Society*, vol. 131, no. 29, pp. 9910-+, Jul 2009.

[40] K. F. Zhou, Y. H. Zhu, X. L. Yang, and C. Z. Li, "One-pot preparation of graphene/Fe3O4 composites by a solvothermal reaction," (in English), *New Journal of Chemistry*, Article vol. 34, no. 12, pp. 2950-2955, 2010.

[41] W. Chen and L. Yan, "In situ self-assembly of mild chemical reduction graphene for three-dimensional architectures," *Nanoscale*, 10.1039/C1NR10355E vol. 3, no. 8, pp. 3132-3137, 2011.

[42] R. Thiruvengadathan *et al.*, "A Versatile Self-Assembly Approach toward High Performance Nanoenergetic Composite Using Functionalized Graphene," *Langmuir*, vol. 30, no. 22, pp. 6556-6564, Jun 2014.

[43] Y. Wu *et al.*, "Three-dimensionally bonded spongy graphene material with super compressive elasticity and near-zero Poisson's ratio," (in English), *Nature Communications*, vol. 6, p. 6141, Jan 2015
2015-01-21 2015.

[44] A. A. Balandin *et al.*, "Superior thermal conductivity of single-layer graphene," (in English), *Nano Letters*, Article vol. 8, no. 3, pp. 902-907, Mar 2008.

[45] Z. Yu, M. McInnis, J. Calderon, S. Seal, L. Zhai, and J. Thomas, "Functionalized graphene aerogel composites for high-performance asymmetric supercapacitors," *Nano Energy*, vol. 11, no. Supplement C, pp. 611-620, 2015/01/01/ 2015.

[46] S. Kéki, J. Török, G. Deák, and M. Zsuga, "Ring-Opening Oligomerization of Propylene Carbonate Initiated by the Bisphenol A/KHCO3 System: A Matrix-Assisted Laser Desorption/Ionization Mass Spectrometric Study of the Oligomers Formed," *Macromolecules*, vol. 34, no. 20, pp. 6850-6857, 2001/09/01 2001.

[47] C. S. Staley, C. J. Morris, R. Thiruvengadathan, S. J. Apperson, K. Gangopadhyay, and S. Gangopadhyay, "Silicon-based bridge wire micro-chip

initiators for bismuth oxide–aluminum nanothermite," *Journal of Micromechanics and Microengineering,* vol. 21, no. 11, p. 115015, 2011.

[48] K. T. Sullivan *et al.*, "Reactive sintering: An important component in the combustion of nanocomposite thermites," *Combustion and Flame,* vol. 159, no. 1, pp. 2-15, Jan 2012.

[49] L. E. Turner, M. G. Davidson, M. D. Jones, H. Ott, V. S. Schulz, and P. J. Wilson, "Bis(bismuth)toluene Inverted-Sandwich Complex Supported by Aminetris(phenoxide) Ligands," *Inorganic Chemistry,* vol. 45, no. 16, pp. 6123-6125, 2006/08/01 2006.

[50] J. Che, L. Shen, and Y. Xiao, "A new approach to fabricate graphene nanosheets in organic medium: combination of reduction and dispersion," *Journal of Materials Chemistry,* 10.1039/B922667B vol. 20, no. 9, pp. 1722-1727, 2010.

[51] W. Gerharz, F. Ullmann, Y. S. Yamamoto, F. T. Campbell, and R. Pfefferkorn, *Ullmann's encyclopedia of inducstrial chemistry, 5th edition*. Weinheim, Federal Republic of Germany ; Deerfield Beach, FL, USA : VCH Publishers, 1985 to Present.

[52] N. Zakiyyan *et al.*, "Combustion of aluminum nanoparticles and exfoliated 2D molybdenum trioxide composites," *Combustion and Flame,* vol. 187, pp. 1-10, 2018/01/01/ 2018.

[53] G. Q. Jian, S. Chowdhury, K. Sullivan, and M. R. Zachariah, "Nanothermite reactions: Is gas phase oxygen generation from the oxygen carrier an essential prerequisite to ignition?," *Combustion and Flame,* vol. 160, no. 2, pp. 432-437, Feb 2013.

[54] A. Rai, K. Park, L. Zhou, and M. R. Zachariah, "Understanding the mechanism of aluminium nanoparticle oxidation," *Combustion Theory and Modelling,* vol. 10, no. 5, pp. 843-859, 2006/10/01 2006.

[55] M. L. Pantoya, V. I. Levitas, J. J. Granier, and J. B. Henderson, "Effect of Bulk Density on Reaction Propagation in Nanothermites and Micron Thermites," *Journal of Propulsion and Power,* vol. 25, no. 2, pp. 465-470, 2009/03/01 2009.

[56] K. B. Plantier, M. L. Pantoya, and A. E. Gash, "Combustion wave speeds of nanocomposite Al/Fe2O3: the effects of Fe2O3 particle synthesis technique," *Combustion and Flame,* vol. 140, no. 4, pp. 299-309, Mar 2005.

[57] G. I. Taylor, "The formation of a blast wave by a very intense explosion I. Theoretical discussion," *Proceedings of the Royal Society of London. Series A. Mathematical and Physical Sciences,* vol. 201, no. 1065, pp. 159-174, 1950.

[58] L. I. Sedov, "Propagation of strong shock waves," *Journal of Applied Mathematics and Mechanics,* vol. 10, pp. 241-250, 1946.

[59] M. R. Baer and J. W. Nunziato, "A two-phase mixture theory for the deflagration-to-detonation transition (ddt) in reactive granular materials," *International Journal of Multiphase Flow*, vol. 12, no. 6, pp. 861-889, 1986/11/01/ 1986.

Chapter 3

Fluorinated Graphene Oxide (FGO) and its Application in Self-Assembled Nanoenergetic Materials

3.1. Introduction

The choices of oxidizers in Al-based nanothermite is diverse. All molecules that can deliver high electronegative elements from themselves to Al fuel, releasing high energy during the reaction can be used as "oxidizer". Those oxidizers, literally, delivering oxygen were mostly commonly used and studied due to its abundance and mature production over hundreds of years. Some other elements, however, can play the same role as oxygen in nanothermite composites, such as halogen elements, which are also highly electronegative. Fluorine is the most electronegative element people have known and has been used in nanoenergetic materials. Different fluorine compounds, including PTFE, THV, PVDF, have already been adopted as the oxidizer in nanothermite composites. [1, 2] Fluorine compounds can react with Al core and release high energy, as shown in equation $2\mathrm{Al}(\mathrm{s}) + 3\mathrm{F}_2(\mathrm{g}) \rightarrow 2\mathrm{AlF}_3(\mathrm{s}) \quad \Delta\mathrm{H} = \text{-}3020.8\ \mathrm{kJ/mol}$ (3.1. Moreover, different from oxygen-based oxidizers, fluorine-containing oxidizers may exothermally react with and etch the alumina shell in a nanothermite composite, as shown in equation $2\mathrm{Al}_2\mathrm{O}_3(\mathrm{s}) + 6\mathrm{F}_2(\mathrm{g}) \rightarrow 4\mathrm{AlF}_3(\mathrm{s}) + 3\mathrm{O}_2(\mathrm{g}) \quad \Delta\mathrm{H} = \text{-}2690.2\ \mathrm{kJ/mol}$ (3.2.

$$2Al(s) + 3F_2(g) \rightarrow 2AlF_3(s) \qquad \Delta H = -3020.8\ kJ/mol \qquad (3.1)$$

$$2Al_2O_3(s) + 6F_2(g) \rightarrow 4AlF_3(s) + 3O_2(g) \qquad \Delta H = -2690.2\ kJ/mol \qquad (3.2)$$

The reaction with Al_2O_3 weakens or removes the shell, allowing access of the Al core to external species and easing the diffusion of Al from the shell. These so-called pre-ignition reactions between the alumina shell and fluorine species have been observed during the decomposition of fluoropolymers such as PTFE and THV. [3, 4] After the shell is removed, the Al core could diffuse out much easier without any barrier and react with the oxidizer easily at a lower temperature than that of traditional nanothermite composites. Please note in equation $2\mathrm{Al(s)} + 3\mathrm{F_2(g)} \rightarrow 2\mathrm{AlF_3(s)} \quad \Delta\mathrm{H} = \text{-}3020.8\ \mathrm{kJ/mol}$ (3.1 and $2\mathrm{Al_2O_3(s)} + 6\mathrm{F_2(g)} \rightarrow 4\mathrm{AlF_3(s)} + 3\mathrm{O_2(g)} \quad \Delta\mathrm{H} = \text{-}2690.2\ \mathrm{kJ/mol}$ (3.2, fluorine gas was referred as the fluorine source. While in real reactions between Al and fluorine compounds, the fluorine sources from the decomposed fragments of the oxidizer, such as fluorine radicals, ions or carbon-fluorine radicals, ions. While fluorine compounds have been brought in the field of nanoenergetics, fluorinated graphene has not.

Functionalization of graphene by chemical groups other than graphene oxide also have grabbed researchers' attention due to its flexibility in realizing application specific characteristics. [5] Halogenated graphene, such as fluorinated graphene, is one of the major branches of graphene functionalization. Following the fluorination of bulk graphite in 1934, [6] exploration of fluorinated carbon-based materials has steadily increased. [7, 8] Fluorographite, [9, 10] which is commonly used as a lubricant, [11] biomolecular sensing agent, [12] and cathode in lithium cell, [13] is prepared by bonding fluorine to sp^2 carbon materials. Fluorine-functionalized polymers, consisting of fluorine atoms bonded to a carbon skeleton, form the basis of commonly used materials such as polytetrafluoroethylene (PTFE). [14-16] More recently, fluorination of carbon nanomaterials such as C_{60}, [17] carbon nanotubes [18-20] and graphene [21, 22] has been demonstrated. Graphene has been widely researched to exploit its high thermal and electrical conductivity, mechanical strength, and unique optical properties, [23, 24] as discussed above. These properties are altered after fluorination due to the strong electronegativity of fluorine. As a result, fluorinated graphene has been applied in high-performance supercapacitors, [25] anode material for lithium-ion batteries, [26] optical limiting devices, [27] and transistors. [28]

Various methods have been developed to obtain fluorinated graphene with different structures and F/C ratios. [29] Gas-solid reactions between F_2 and GO [24], or between XeF_2 and chemical vapor deposition (CVD) graphene [21, 30] generated fluorinated graphene with an F/C ratio approaching unity. Plasma fluorination of graphene and GO using inorganic fluorine compounds such as SF_6, [31], CF_4 [32] or argon/F_2, [33] provided a mild F/C ratio up to 0.3. Other chemical methods such as hydrothermal (F/C up to 0.48) [34, 35] and photochemical fluorination (F/C up to 0.33), [36] or physical exfoliation of fluorographite (F/C up to 1.00) [37, 38] were also employed to obtain fluorinated graphene. Of these techniques, gaseous fluorination provided the highest capacity and controllability for fluorine loading; however, the toxicity of F_2 gas limits its wide application despite its high efficiency and wide capability, [39] and previous investigation of XeF_2 has been limited to CVD graphene, leading to fluorinated graphene without oxygen functional groups, limiting its further applications. [30] Therefore, I tried multiple fluorination method, including hydrothermal fluorination utilizing HF and GO, as well as XeF_2 gas-solid fluorination method on both commercial graphene and GO.

3.2. Synthesis and characterization of hydrothermally produced fluorinated reduced graphene oxide (F-rGO)

GO was synthesized following the method described in chapter 2.2.

To produce fluorinated reduced graphene oxide (F-rGO) through hydrothermal process, 2 mg/mL GO aqueous dispersion and HF were mixed and sealed in a Teflon autoclave, and then reacted in a furnace of 180°C for 30 hours. The autoclave was then cooled down to room temperature. The produced F-rGO gel was then crashed and washed by deionized water repeatedly to remove any remained acid in the structure. The F-rGO powder was finally obtained after drying at 50°C.

F-rGO/Al samples were prepared using the following procedure. Calculated amount of the dried F-rGO and Al NPs were dispersed in IPA for 4 hours, then mixed and sonicated for another hour. After sonication, the mixture was poured onto Al foil and dried under vacuum at room temperature.

rGO gel was also synthesized by hydrothermal process without HF, and then rGO/Al was produced following the same method of F-rGO/Al.

SEM-EDS was used to measure the structural and elemental properties of the produced F-rGO, and DSC-TGA was used to find out the reaction of F-rGO/Al.

Similar to hydrothermal processes without HF in publications, [40] GO was also reduced and formed a hydrogel after the hydrothermal reduction in the presence of HF. The formation of the gel was driven by the π-π interaction of the reduced graphene layers.

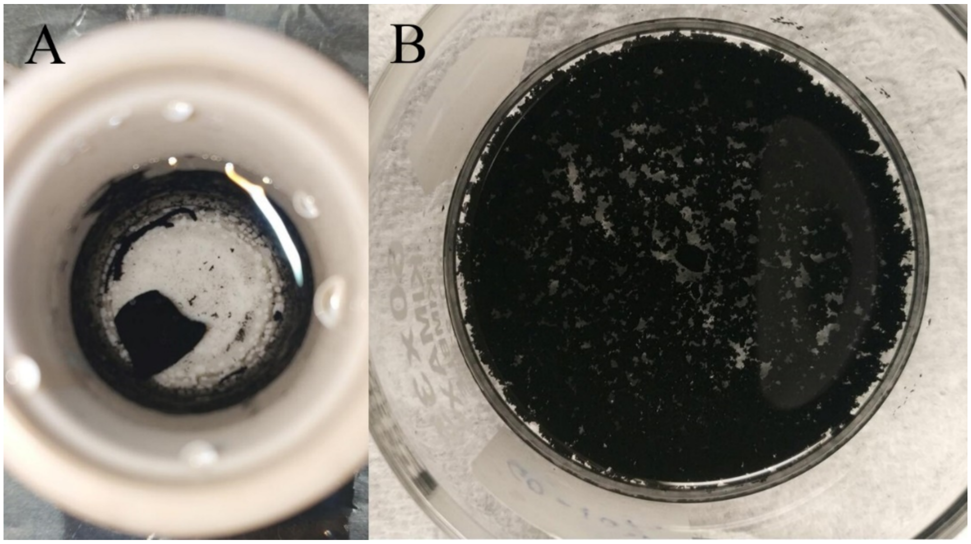

Figure 3.1 Photographs of as-produced F-rGO (A), and the broken pieces of the gel during washing (B).

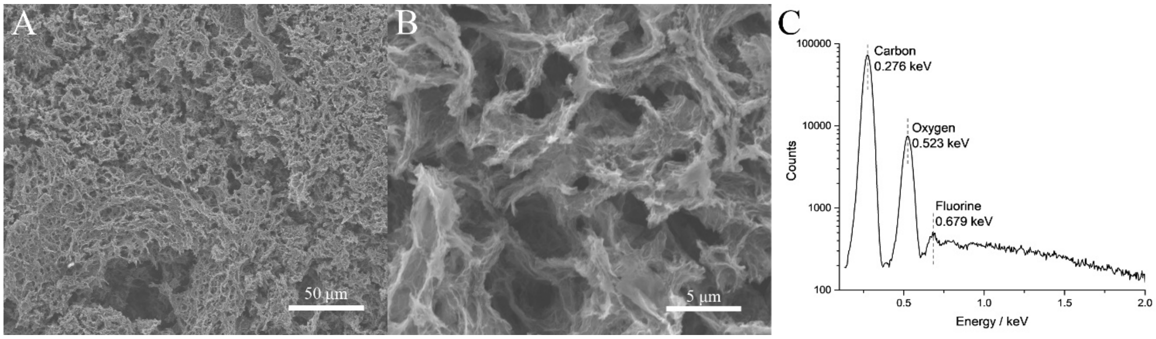

Figure 3.2 SEM pictures (A,B) and EDS spectrum (C) of F-rGO.

SEM-EDS was carried out to investigate the morphology and elemental composition of the produced F-rGO. The F-rGO showed a porous structure in micro scale, due to the interconnections of the reduced graphene layers, which was also observed in solvothermal reduced rGO gels. The EDS spectrum of F-rGO in **Figure *3.2***C confirmed the existence of fluorine in F-rGO. However, the fluorine peak was tiny, and the atomic percentage of fluorine was less than 1% in all samples prepared, typically around 0.2 to 0.3%. The synthesis of F-rGO through HF hydrothermal process was delicate, as reported by Z. Wang et al. [34] A small change in pH or other conditions can result in significantly different fluorine percentage in final content. It is reasonable to assume that the poor fluorination degree of F-rGO was resulted from the precursor graphene oxide we used. As confirmed by the FTIR result in Figure 2.16, the GO we used contained a high amount of carbonyl group and carbolic acid groups, which is a nature of GO produced by Hummer's method, due to the extremely strong oxidizing nature of potassium permanganate. [41] The GO we used was suitable for self-assembling with Al/Bi_2O_3 due to its high surface negative electricity from the abundant carbolic acid groups, [42] and for producing rGO/Al/Bi_2O_3 gel because of the reaction forming Schiff base between the C=O group and EDA. However, when turning to hydrothermal functionalization, the high oxidation state of -COOH and C=O made them difficult to be replaced by or added with other elements. Therefore, the fluorination process between GO and HF here did not produce F-rGO with high fluorine loading.

Table 3.1 A typical element composition of F-rGO.

Element	Mass percentage	Atomic percentage
Carbon	83.42%	87.05%
Oxygen	16.21%	12.70%
Fluorine	0.38%	0.25%

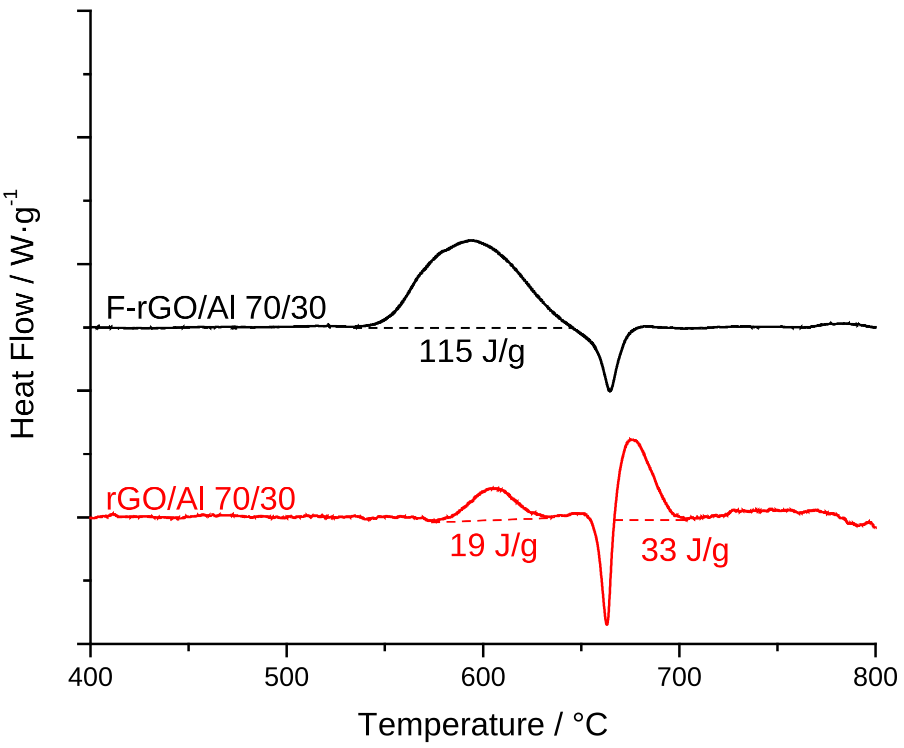

Figure 3.3 DSC results of hydrothermal F-rGO/Al and rGO/Al.

Although the fluorine loading in F-rGO was small, the reaction between F-rGO and Al was still examined, as shown in Figure 3.3. Both F-rGO/Al and rGO/Al were prepared in a mass ratio of 70 – 30. In rGO/Al, a tiny exothermic peak of 19 J/g showed up before the melting of Al due to the reaction between the decomposed fragments (carbon-fluorine composite) from the remained functional groups after solvothermal process. The main reaction occurred after the melting of Al, when the liquid-phase Al core could freely flow out of the shell and react with the surrounding rGO. While in F-rGO/Al, the main reaction occurred before the melting of Al, peaking at 590°C and giving an energy release of 115 J/g. The peak indicates that the shell was weakened by the fluorine content released from F-rGO decomposition, allowing the Al core to diffuse out and react with F-rGO at a lower temperature in prior to melting. However, even with excessive F-rGO, a significant endothermic peak of Al melting still showed up, indicating not the shell of all Al NPs was well weakened. It happened probably because the F-rGO was not well-assembled with Al, resulted from its poor dispersity in IPA after being reduced and fluorinated. [34]

It was reported that the F/C ratio could reached up to 0.48 in publications. However, it requires re-design our synthesis method for GO, which was a mature method and has been used in different projects for long time. The dispersity of F-rGO was also considered as a negative factor for using it for self-assembly with energetic nanoparticles. Therefore, instead of HF hydrothermal fluorination, the direction was turned to use XeF_2 directly fluorinate graphene.

3.3. Synthesis and characterization of XeF_2 fluorinated highly exfoliated commercial graphene (FG)

There has been a lot of research on the directly fluorination by XeF_2 on CVD graphene. Fluorine atoms directly add onto the sp^2 carbon atom, forming F-C (sp^3) structures. [30] However, the complicated production process and high price of high-quality CVD graphene significantly limited further application of the fluorinated CVD graphene. Meanwhile, the commercial graphene produced by thermal exfoliation after chemical intercalation of natural graphite provides a reasonable price and is ideal for bulky production. However, the exfoliated graphene is not a perfect structure as normally seen in CVD graphene. It contains a lot of defects and about 10% of oxygen and nitrogen atoms, as indicated by the manufacturer. In order to bulky produce fluorinated graphene by XeF_2 fluorination, the reaction between XeF_2 and commercially available thermally exfoliated graphene was carried out.

130 mg highly exfoliated commercial graphene (C-750 from XG Science, Lansing, MI) was first compressed to 1/2-inch-diameter pellet by a mechanical tablet press under the pressure of 10k psi. A custom-built pulsed xenon difluoride (XeF_2) reaction system was used for the fluorination of the pressed highly exfoliated commercial graphene pellets. XeF_2 in its vapor phase is pulsed into the reacting chamber until the pressure in the chamber reached 3000mTorr, and the reaction of graphene pellet with XeF_2 was carried out for 10 minutes before the reaction chamber was purged with N_2 to complete one cycle of the pulsed reaction. The reaction finished after 270 pulsed cycles, producing the XeF_2 fluorinated highly exfoliated commercial graphene (FG).

To produce the FG/Al sample for characterization, both Al and the synthesized FG was dispersed in IPA for 4 hours, followed by mixing together and sonicated for one more hour. The mixture was then poured into Al foil bowl and dried under vacuum at room temperature.

FTIR-ATR was used to characterize the functional groups of FG, TGA and MS were used to figure out the decomposition of FG. The reaction between FG and Al was also characterized by DSC-TGA.

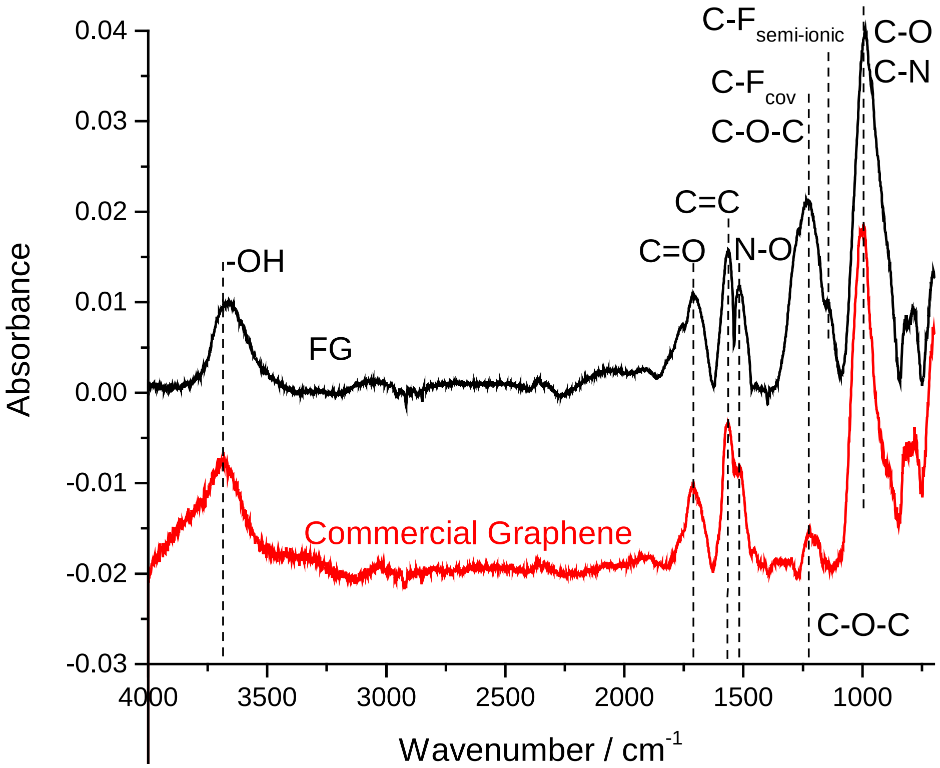

Figure 3.4 FTIR-ATR results of FG and commercial graphene.

FTIR-ATR was first used to find out the change in functional groups in fluorinated graphene. FTIR-ATR was used instead of transmission FTIR because FG tended to agglomerate at the edge of Si wafer when drop-casting was applied. The FTIR-ATR results are shown in Figure 3.4. The ATR signal of the sample was quite weak, giving a poor signal – noise ratio. There are a few peaks in the curve of commercial graphene due to the remained oxygen and nitrogen in this thermally exfoliated graphene, as described by the manufacturer. The major difference in FTIR-ATR between commercial graphene before and after XeF_2 fluorination was the peak around 1220 cm^{-1}. The small peak in the original commercial graphene was at 1220 cm^{-1}, resulted from the C-O-C groups in the material. After fluorination by XeF_2, this peak was significantly enhanced due to the formation of C-F covalent bond, which also has a FTIR peak around 1220 – 1230 cm^{-1}. [29, 39] A shoulder was also found in the curve of the fluorinated graphene at 1140 cm^{-1}, which can be assigned to the semi-ionic C-F bond. [39] Other peaks in commercial graphene, which were assigned to other functional groups such as -OH, C=O and N-O, did not change much after fluorination. Therefore, these functional groups did not react during the XeF_2 process. The main reaction was most likely addition of fluorine to sp^2 carbon of graphene skeleton. Therefore, the FTIR-ATR result confirmed that commercial thermally exfoliated graphene was successfully fluorinated by XeF_2.

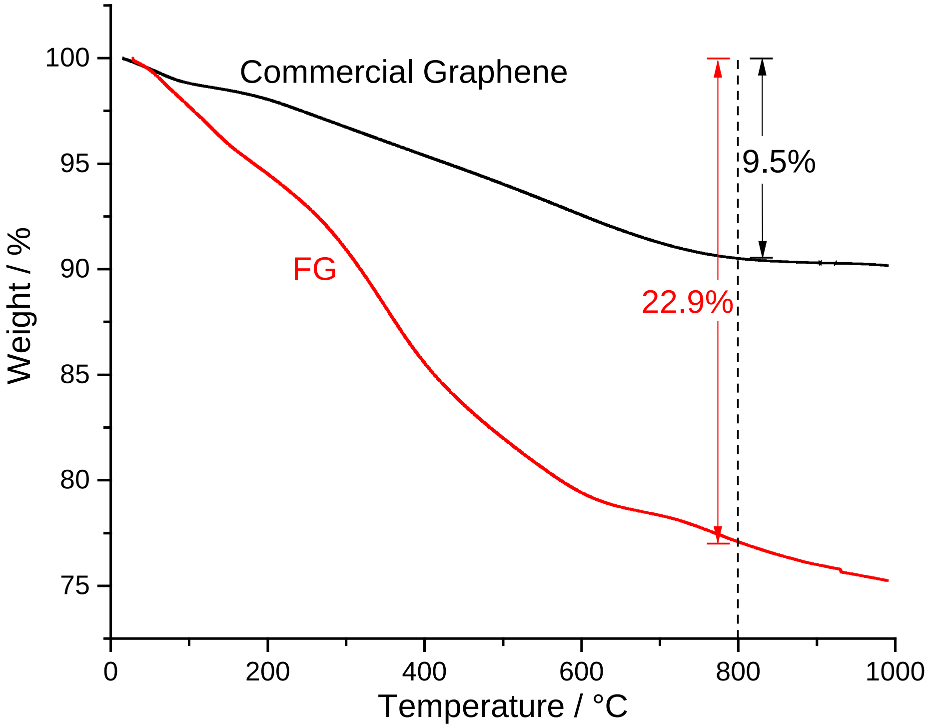

Figure 3.5 TGA results of commercial graphene before and after fluorination.

The occurrence of FG decomposition determines at which temperature the fluorine can be released and react with the Al nanoparticles is critical for utilizing FG in nanothermites. FG showed no sharp weight loss peak but continuously lost weight from room temperature to 1000°C. It showed distinct TGA curve from CVD graphene, which gives no or only very little weight loss, and GO, which usually give a significant weight loss at 200°C. That happened because the material was produced from functionalized graphene but was already reduced during the thermal exfoliation process in its synthesis. Fluorinated graphene showed similar trend but much larger weight loss. When heated to 800°C, the weight loss in FG was 22.9%, much higher than the 9.5% in commercial graphene, which occurred due to the addition of fluorine. There is no such a temperature for a significant weight loss, indicating the fluorine do not exist in the forms of easily decomposing functional group. Therefore, the fluorine was mostly strongly bonded with carbon atoms in the form of either covalent or semi-ionic bonding, which corresponds with the result of ATR.

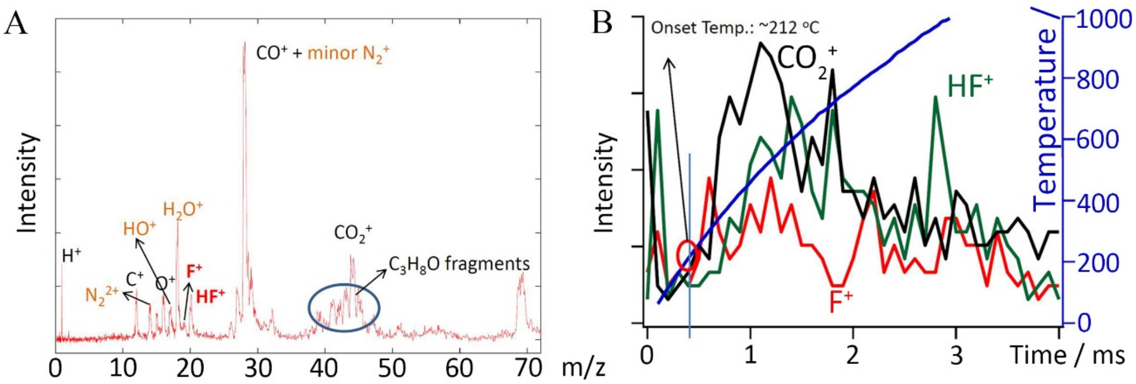

Figure 3.6 Overall mass spectrum (A) and different species with time and temperature (B) of FG.

Mass spectrometry (MS) also confirmed the existence of fluorine in FG, shown in Figure 3.6. The mass spectrometry was couple with a T-jump system as described in publications. [43] Briefly, FG dispersion was coated on the surface of a Pt filament, which was then rapidly heated. The decomposed fragments were collected and tested by mass spectrometry in real time. The peak of F^+ (m/z = 19) and HF^+ (m/z = 20) showed up in the integrated MS plot, confirming the existence of fluorine in the FG and its release during heating process. The signal of the decomposition species appeared in the entire heating stage, indicating the loss of fluorine and carbon fragments after decomposition during the whole temperature range, corresponding with the TGA and ATR results of FG. Therefore, the scheme of the reaction between commercial graphene and XeF_2 is summarized in Figure 3.7. As discussed in ATR results, the main reaction was the addition of fluorine to the sp^2 carbon of the graphene skeleton. The functional groups were not affected.

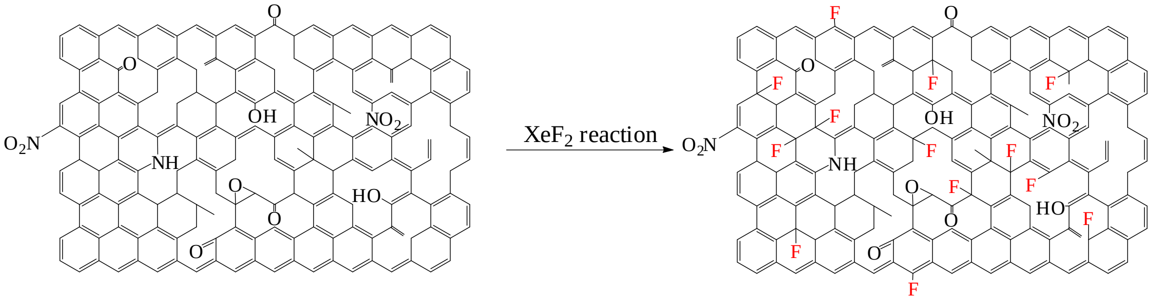

Figure 3.7 Scheme of reaction forming FG.

DSC measurement of commercial graphene/Al and FG/Al (both in the mass ratio of 90-10) were carried out to understand the reaction between the released fluorine from FG and Al NPs, shown in Figure 3.8. Compared to commercial graphene, which only showed a tiny exothermal reaction peak of 12 J/g after the endothermic peak of Al melting, resulted from the reaction between melted Al and the commercial graphene. There was no reaction between Al and commercial graphene before reaching 660°C, indicating the Al had to melt to massively flow out from the alumina shell and react with graphene. While in FG-Al, a significant exothermic reaction of 72 J/g showed up before the melting of Al, peaking at 628°C. The reaction indicated that the shell was weakened due to the existence of fluorine in FG, allowing the Al core to diffuse out of the shell easier before melting. Some Al core remained unreacted when reaching the melting point, which was confirmed by the small endothermal peak at 660°C, following the main exothermal reaction.

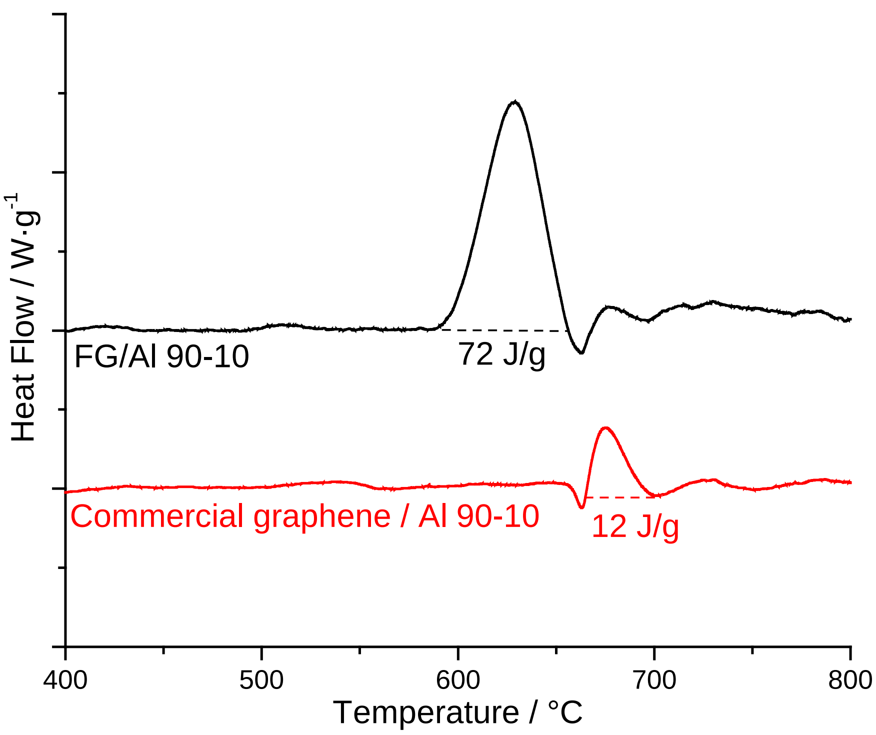

Figure 3.8 DSC results of FG/Al and commercial graphene/Al with mass ratio of 90-10.

It was confirmed that thermally exfoliated commercial graphene was successfully fluorinated by XeF_2, and the fluorine could release and lower the reaction temperature with Al NPs compared to raw commercial graphene. However, the low amount of oxygen in the commercial graphene limited the dispersity of the produced FG, and the melting peak of Al core still existed with only 10% by mass of Al NPs. Therefore, further research of fluorinated commercial graphene was not carried out but focused on the direct XeF_2 fluorination of GO sheets.

3.4. Synthesis of XeF_2 fluorinated graphene oxide

GO was synthesized following the method described in chapter 2.2.

A custom-built pulsed xenon difluoride (XeF_2) reaction system was used for the fluorination of GO paper. XeF_2 in its vapor phase is pulsed into the reacting chamber until the pressure in the chamber reached 3000mTorr, and the reaction of GO paper with XeF_2 was carried out for 10 minutes before the reaction chamber was purged with N_2 to complete one cycle of the pulsed reaction. Two sets of fluorinated GO paper were synthesized under room temperature, one with 130 pulsed cycles corresponding to 1300 minutes of XeF_2 treatment, labeled as FGO-I, and the other with 270 cycles corresponding to 2700 minutes of XeF_2 treatment, labeled as FGO-II. After reaction, the samples were stored in a desiccator at approximately 15% humidity and 25°C before further characterization.

GO/Al and FGO/Al samples were prepared using the following procedure. FGO samples were used immediately after XeF_2 treatment. GO and FGO were first dispersed in isopropanol (IPA, anhydrous grade, Fluka) at a concentration of 2 mg / mL by sonication for 5 hours. Separately, Al nanoparticles (Novacentrix, 80 nm average diameter with 2.2 nm Al_2O_3 shell, 79% reactive) were dispersed in IPA at a concentration of 20 mg / mL for 4 hours. The Al dispersion was then added to the FGO or GO dispersion in pre-determined quantities, and sonication for an additional 4 hours. The mixture was then dried under vacuum.

Al/Bi_2O_3 nanothermite (Al/Bi_2O_3 equivalence ratio = 1.4) was synthesized by 5-hour sonication. Bi_2O_3 nanoparticles (Aldrich, 200 nm) were first sonicated in IPA (400 mg in 1.2 mL) for 1 hour. Thereafter, 82 mg of Al nanoparticles were added directly to the Bi_2O_3/IPA dispersion and sonicated for an additional 4 hours. The dispersion was then dried under vacuum. [42]

The $FGO/Al/Bi_2O_3$ and $GO/Al/Bi_2O_3$ nanothermite composite were prepared by a similar 9-hour sonication process. FGO was dispersed in IPA at a concentration of 2 mg / mL by sonication for 5 hours. Simultaneously, Al /Bi_2O_3 was prepared in IPA using the 5-

hour sonication process described above. The Al/Bi_2O_3 dispersion was then added to the FGO dispersions and sonicated for an additional 4 hours. The mixture was then dried under vacuum. FGO and GO occupied 5% of total mass in the nanothermite composite, and the equivalence ratio between Al and Bi_2O_3 was 1.4 (fuel rich). A control Al/Bi_2O_3 sample was also prepared separately to compare the energy release with the FGO/Al/Bi_2O_3 and GO/Al/Bi_2O_3 sample.

FTIR, SEM-EDS, XRD, DSC-TGA and T-jump mass spectrometry was used for the structural and elemental analysis of FGO, and DSC-TGA was also performed to analyze the energetic reaction between FGO and Al NPs.

3.5. Structural analysis and stability study of FGO

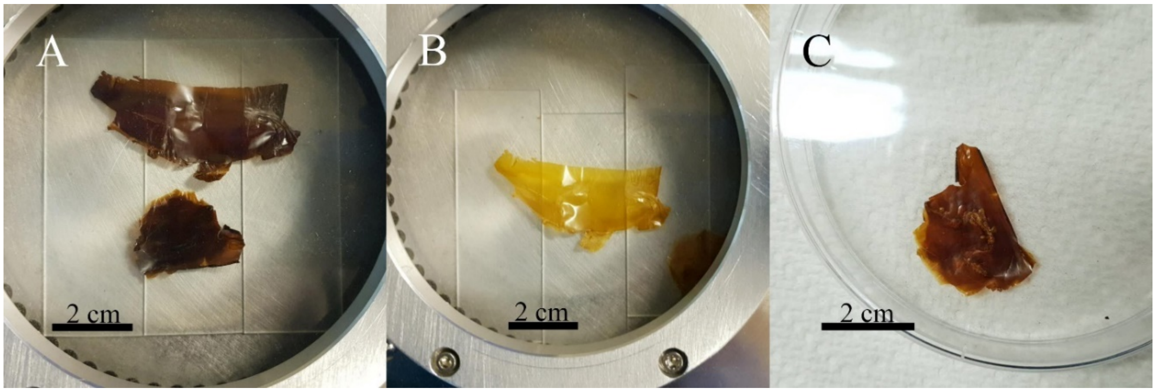

Figure 3.9 Photographs of GO (A) FGO-I right after XeF_2 treatment (B) and after 3 days in desiccator (15% humidity) (C).

GO paper underwent a color change as a result of the XeF_2 fluorination process, as shown in Figure 3.9. The initial GO paper was dark brown (Figure 3.9A). After 1300 minutes of XeF_2 treatment, the FGO paper was a light, translucent yellow (Figure 3.9B), similar to fluorination of GO by F_2. [39] After three days in a desiccator chamber, the FGO paper turned light brown, indicating further composition change (Figure 3.9C). The FGO-II sample (2700 min exposure) showed a similar color change.

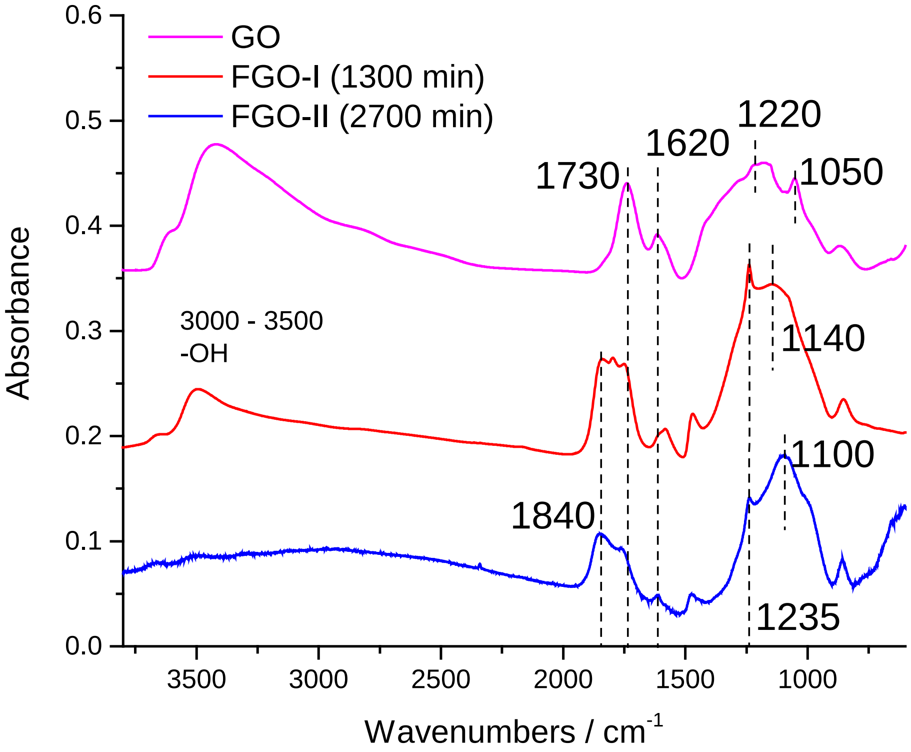

Figure 3.10 FTIR curves of GO, FGO-I (1300 min) and FGO-II (2700 min).

FTIR measurements showed distinct changes in the chemical structure of GO after reaction with XeF_2, as shown in Figure 3.10. The strong peak present in GO located at 3000 – 3700 cm^{-1}, corresponds to the O-H stretching in C-OH groups and -COOH groups, was significantly reduced in FGO-I after reaction with XeF_2 for 1300 minutes, and almost disappeared in FGO-II after 2700 minutes, indicating the replacement of hydroxyl groups by fluoride groups. Previous reports showed that the bonded hydrogen atoms in macromolecules, such as polymers, could be readily substituted by fluorine, [44] and the potential HF product might further catalyze the fluorination reaction. [45] The absorption band at 1730 cm^{-1}, attributed to the C=O stretching in the GO structure, remained similar after XeF_2 treatment, indicating no significant reaction between the carbonyl groups in GO and XeF_2. The asymmetric and symmetric stretching of -COO- in the carboxyl acid groups in GO, shown by the absorption bands at 1620 cm^{-1} and 1420 cm^{-1} respectively, were reduced significantly after reaction. Correspondingly, an extra absorption band appeared at 1840 cm^{-1}, representing the C=O stretching in acyl fluoride (F-C=O), produced by the substitution of -OH groups in carboxyl acid by fluorine atoms. The absorption bands for stretching of the C-O bond in C-O-C and C-OH groups at 1220 cm^{-1} and 1050 - 1060 cm^{-1} were also diminished. The sharp peak at 1235 cm^{-1} reflects the formation of C-F covalent bonding, the chemical bond between fluorine and sp^3 hybridized carbon. The peak near 1140 cm^{-1} in FGO-I revealed the formation of the semi-ionic C-F bond between fluorine and sp^2 hybridized carbon, which was also found in the carbon fluorinated nanotube produced below 100°C. [20, 29] In FGO-II, the peak shifted to around 1100 cm^{-1}, indicating the formation of CF_x (x>1) in the structure. The presence of these unique peaks indicated the successful fluorination of GO after fluorination reaction by using XeF_2 gas for 1300 or 2700 minutes. A scheme of the reaction is included in Figure 3.11.

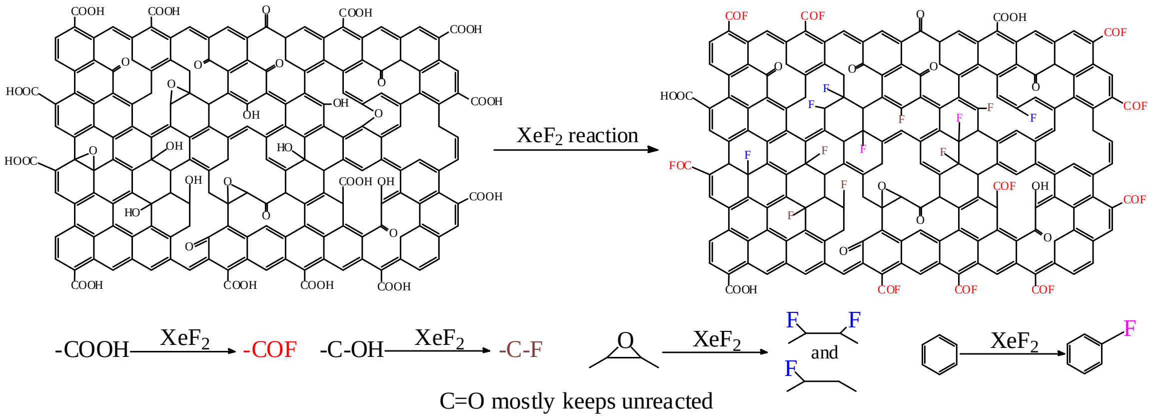

Figure 3.11 Scheme of reactions during the XeF_2 treatment.

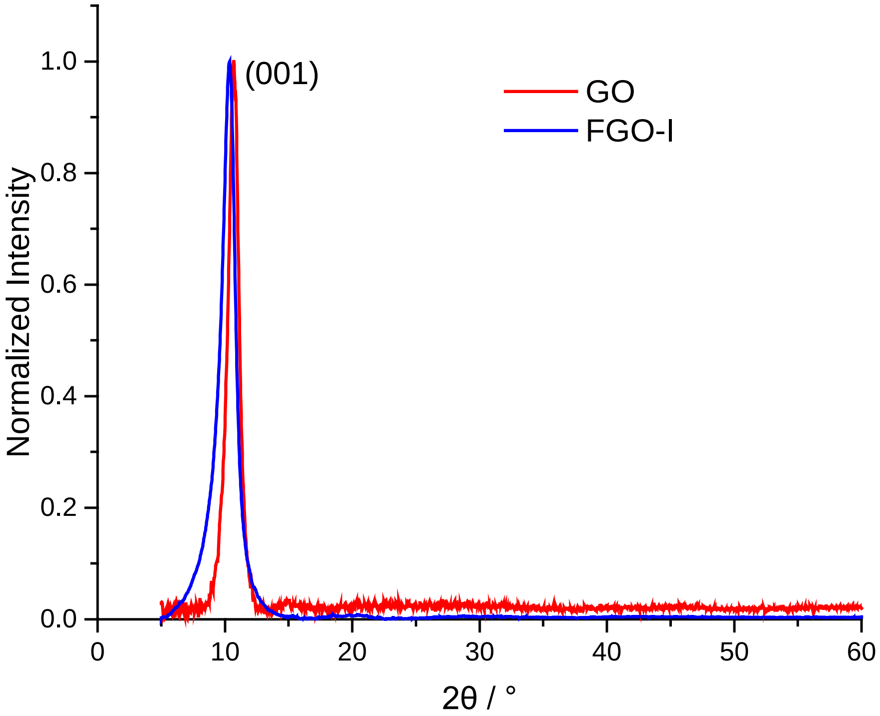

Figure 3.12 XRD patterns of GO and FGO-I.

Table 3.2 XRD data of GO and FGO-I.

Sample	Peak Angle(2θ)	d spacing (Å)	FWHM
GO	10.507	8.416	0.964
FGO-I	10.313	8.571	1.285

The XRD results of GO and FGO-I are shown in Figure 3.12 & Table 3.2. The XRD spectra of GO and FGO-I was measured in the range of 5° to 60° and both the samples shows a peak (001) at 2θ ~ 10.5°. Due to fluorination of GO, there is small change in the peak (001) value. It is postulated that oxygen-containing groups in the stacking were replaced by fluorine atoms, thereby changing the interlayer distance (d). It is also noted that the FWHM of FGO increased, an indication of a lower degree of crystallinity as compared to GO. Due to a small change in the interlayer distance (d), the majority of oxygen functional groups remained in the structure, suggesting only minor incorporation of fluorine atoms during the XeF_2 treatment of GO.

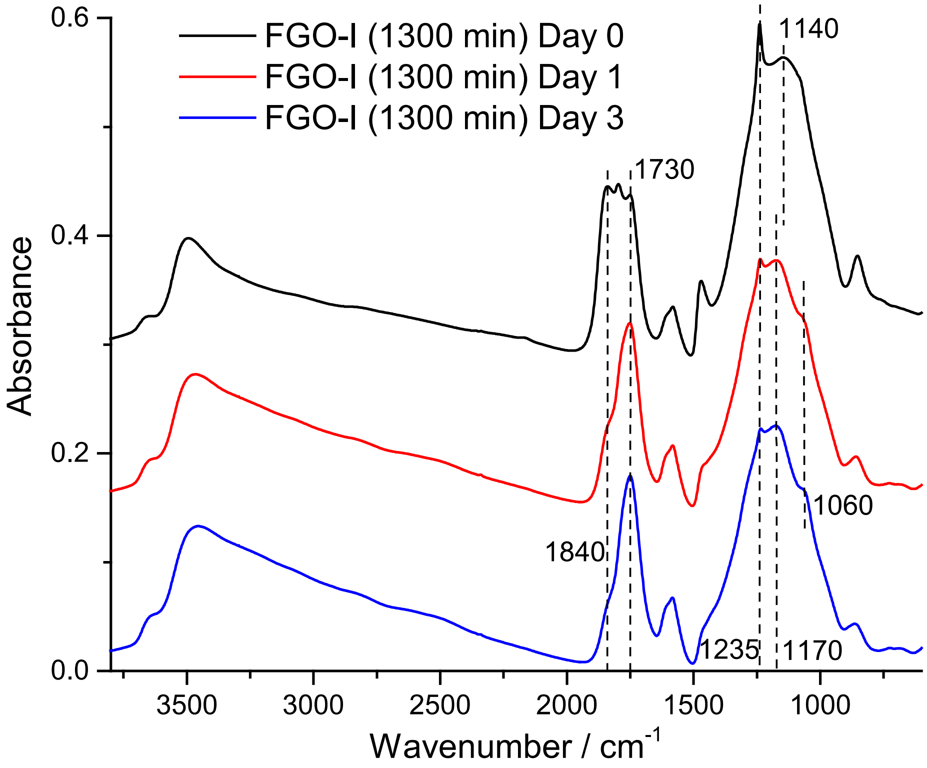

Figure 3.13 FTIR curves of GO and FGO-I (Reacted with XeF_2 for 1300 min) after storage in a desiccator.

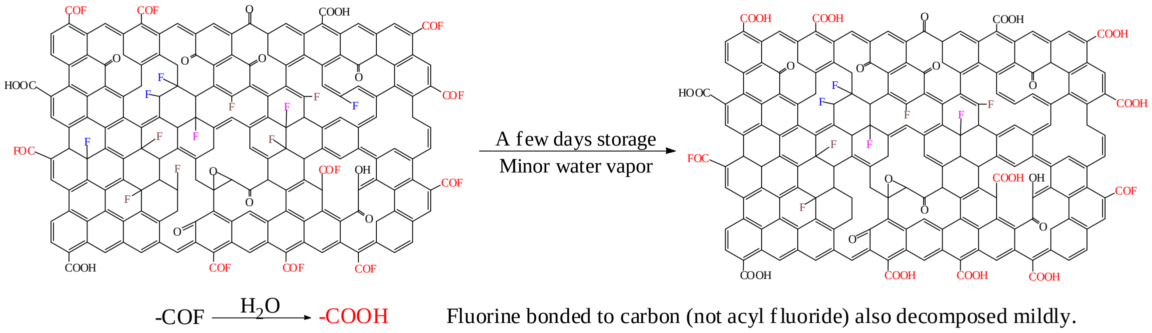

$-COF \xrightarrow{H_2O} -COOH$

Fluorine bonded to carbon (not acyl fluoride) also decomposed mildly.

Figure 3.14 Scheme of FGO material change during storage.

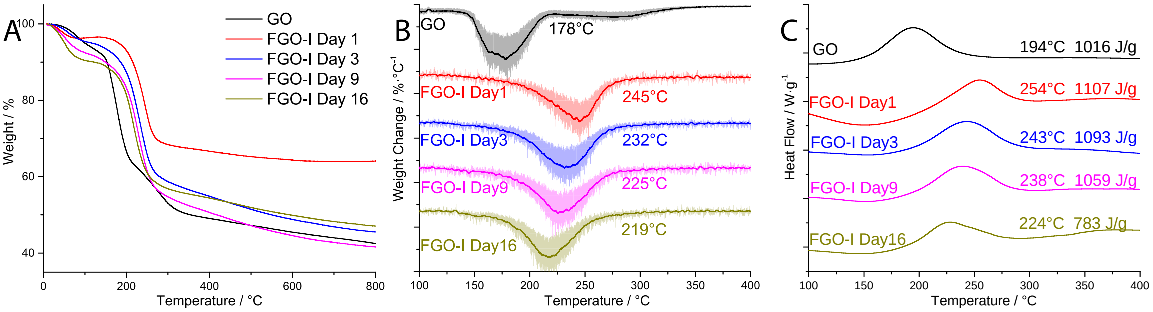

Figure 3.15 TGA (A), DTG (B) and DSC(C) curves of FGO-I for a storage duration of up to 16 days after synthesis. In figure B, half transparent background is the differential of TGA, while the solid curve represents the smoothed data. The temperature indicates the peak temperature of the smoothed line for each sample. Figure C shows DSC curves from GO and FGO samples after various storage times. The temperature shown above the DSC curves represents the peak of DSC curves, and the energy release is obtained from the integration of the heat flow peak. Upward is exothermic.

FTIR was also employed to investigate the stability in the FGO structure with time when stored in a desiccator environment (~15% humidity), as shown in Figure 3.13. After 3 days stored in the desiccator, the absorption band of C=O stretching in acyl fluoride (1840 cm^{-1}) was significantly reduced, remaining only as a small shoulder due to the hydrolysis reaction of acyl fluoride groups with free water in atmosphere (-COF + H_2O → -COOH + HF). The -OH absorption band from 3200 – 3700 cm^{-1} slightly increased due to the same process. Additionally, the sharp C-F covalent peak at 1235 cm^{-1} was reduced, and the C-F semi-ionic peak around 1140 cm^{-1} also shifted to around 1170 cm^{-1}, indicating the decomposition of some C-F bonds in the structure. This result corresponds with the results reported by Stine et al. that fluorine bonded with the basal plane of carbon decomposed with storage time. [30] A small shoulder also appeared at 1060 cm^{-1}, indicating the formation of more C-OH groups during storage. Therefore, after GO was fluorinated by XeF_2, reactions with residual atmospheric water vapor lead to a gradual loss of the fluorine functional groups and a return back to a structure similar to GO. The scheme of the material change during storage is included in Figure 3.14.

DSC-TGA was also carried out to measure the thermal stability of FGO samples with time. Results are shown in Figure 3.15. Neat GO paper was examined as a baseline. The GO paper decomposed exothermically from 150°C to 300°C, with a peak energy release at 178°C. Newly prepared FGO-I samples began losing mass at 245°C, while samples stored in a desiccator for 2 weeks began losing mass at 219°C, as shown in Figure 3.15B. The mass loss of GO and exothermal reactions were attributed to the decomposition process of oxygen-containing functional groups, including hydroxyl, epoxide, carbonyl and carboxyl groups. Figure 3.15B shows that the mass loss can be divided into two different stages. Stage I is from 150°C to around 210°C, represented by a peak in the differential thermal gravimetry (DTG) curve in Figure 3.15B, indicating the evaporation of trapped water and removal of labile oxygen functional groups such as epoxyl or hydroxyl groups in the basal plane of graphene. [46, 47] Stage II occurred from 210°C to about 300°C and reflected a slower mass loss. The removal of more stable oxygen functional groups, such as carboxyl and carbonyl groups, occurred in this stage. In the DTG curve of the FGO-I sample shortly after fluorination in Figure 3.15B (Day 1), the initiation of mass loss occurred at 210°C, indicating that most labile epoxyl and hydroxyl groups had been removed from the structure during XeF_2 treatment. After 16 days of storage, the decomposition temperature of FGO-I reduced to 219°C, indicating that some of the fluorinated groups decomposed during storage. Meanwhile, the temperature associated with peak energy release also decreased in FGO-I sample with storage time based on DSC results, shown in Figure 3.15C. The total energy release also decreased with storage, revealing that some fluorine functional groups were unstable at room temperature. The material reacted spontaneously and reached a state with lower energy. Note that a trend towards decreased decomposition temperature, reaction temperature, and energy loss are observed for intermediate days of desiccator storage. More detailed change in functional groups will be discussed below with FTIR results.

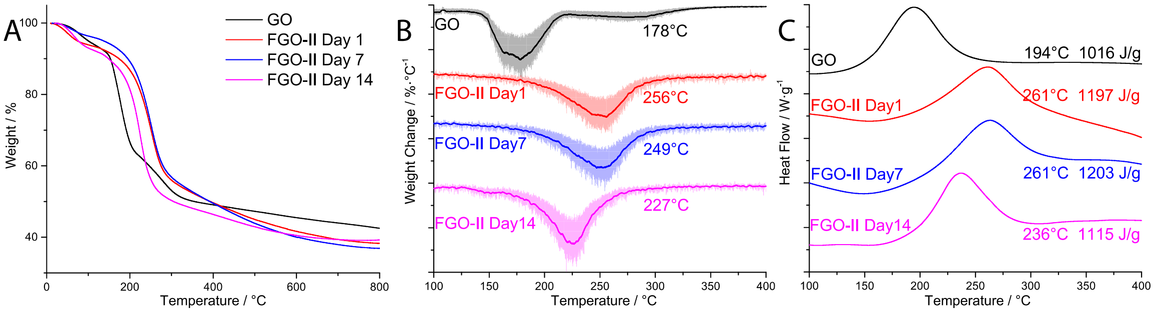

Figure 3.16 TGA (A), DTG (B) and DSC(C) curves of FGO-II in 2 weeks after synthesis. In figure B, the transparent background represents the unsmoothed differential TGA data, while the solid curves represent smoothed data. The temperature indicates the peak temperature of smoothed line of each sample. Figure C shows DSC curves from GO and FGO samples after various storage times. The temperature shown above the DSC curves represents the peak of DSC curves, and the energy release is obtained from the integration of heat flow peak. Upward is exothermic.

FGO-II showed similar DSC-TGA trends, as observed in Figure 3.16. The FGO-II sample contained a greater quantity of fluorine and produced a greater decomposition temperature compared to FGO-I at comparable storage times. The integrated energy release during decomposition, the peak temperature of mass loss and the peak temperature of heat release reduced significantly after 2 weeks of storage. It also confirmed that XeF_2-treated GO might return to a structure similar to GO during storage due to the reaction and decomposition of some fluorine functional groups. However, the DSC-TGA data after Day 1 and Day 7 of storage were very similar. This result is in contrast to those of FGO-I which showed a significant difference even after 3 days of storage. Therefore, increased fluorine content seems to have increased the stability of FGO to moisture.

Table 3.3 Composition of FGO-I after heating to different temperatures by SEM-EDS.

Temperature	Element content (Atomic)			Element Ratio	
	Carbon	Oxygen	Fluorine	C/O	F/O
No heating	51.5%	36.9%	11.0%	1.43	0.306
150°C	54.8%	37.6%	6.8%	1.43	0.180
300°C	68.5%	27.6%	2.4%	2.48	0.085
450°C	77.2%	20.6%	0.6%	3.74	0.027
600°C	83.4%	14.7%	0.4%	5.66	0.028

To further investigate FGO decomposition during heating, the elemental composition of FGO-I was measured by SEM-EDS after heating to 150°C, 300°C, 450°C, and 600°C and held isothermally for 5 minutes. The results are listed in Table 3.3. After 1300 minutes of XeF_2 treatment, the fluorine content was approximately 11 at. %. Upon heating to 150°C, and before the main decomposition starts (as identified by DSC-TGA), the fluorine content decreased to approximately 7%, implying that some fluorine species were extremely unstable and may be associated as intercalated fluorine molecules, such as HF, stabilized between GO sheets due to the intermolecular forces. Note that while the F/O ratio decreased, the C/O ratio remained stable when heated to 150°C, indicating the reduction of GO did not commence prior to 150°C. At higher temperatures, the C/O ratio increased as the oxygen functional groups in FGO reduced. At the same time, the fluorine content decreased at a faster rate than oxygen, as confirmed by the decreasing F/O ratio with temperature.

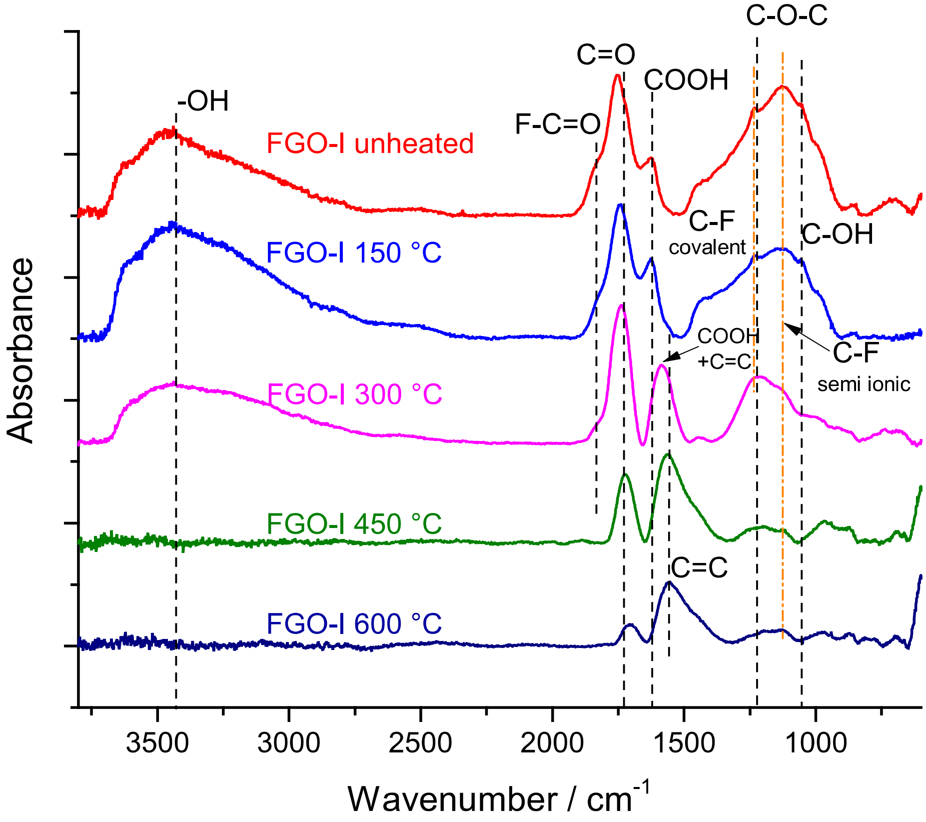

Figure 3.17 FTIR-ATR of FGO-I (by XeF_2 for 1300 min) after heating to different temperatures.

FTIR-ATR spectra on heated samples are shown in Figure 3.17. The change of different functional groups can be clearly seen. Acyl fluoride (F-C=O, shoulder at 1840 cm^{-1}) reduced after heating to 150°C, and disappeared at 300°C. The C-F covalent bond (1235 cm^{-1}, as denoted by the short orange line to the left of C-O-C peak in Figure 3.17) showed a small peak in unheated samples and those heated to 150°C but reduced after heating to 300°C and disappeared at higher temperatures. C-F semi-ionic bond (1140 cm^{-1}) also significantly reduced after heating to 300°C. After being heated to 600°C, all other peaks disappeared except for a small peak corresponding to semi-ionic C-F bond.

Therefore, both covalent and semi-ionic C-F bonds decomposed, and some of the stronger C-F covalent bond might transform to less stable C-F semi-ionic bond during the heating process.

Little change in oxygen functional groups was found between the unheated samples and those heated to 150°C. Hydroxyl groups (-OH, 3000 – 3700 cm^{-1}, C-OH, 1050 – 1060 cm^{-1}) were significantly reduced between 150 – 300°C and almost disappeared when heated to 450°C. A similar trend occurred for the peak of carbolic acid (-COOH, 1620 cm^{-1}). It overlapped with alkane bond (C=C, 1580 cm^{-1}) peak when the sample was heated to 300°C, giving a peak between 1580 and 1620 cm^{-1}. When the sample was heated to higher temperature (450 and 600°C), the peak of carbonyl groups (-C=O, 1730 cm^{-1}) and ether groups (C-O-C, 1220 cm^{-1}) decreased significantly, indicating their decomposition at elevated temperature.

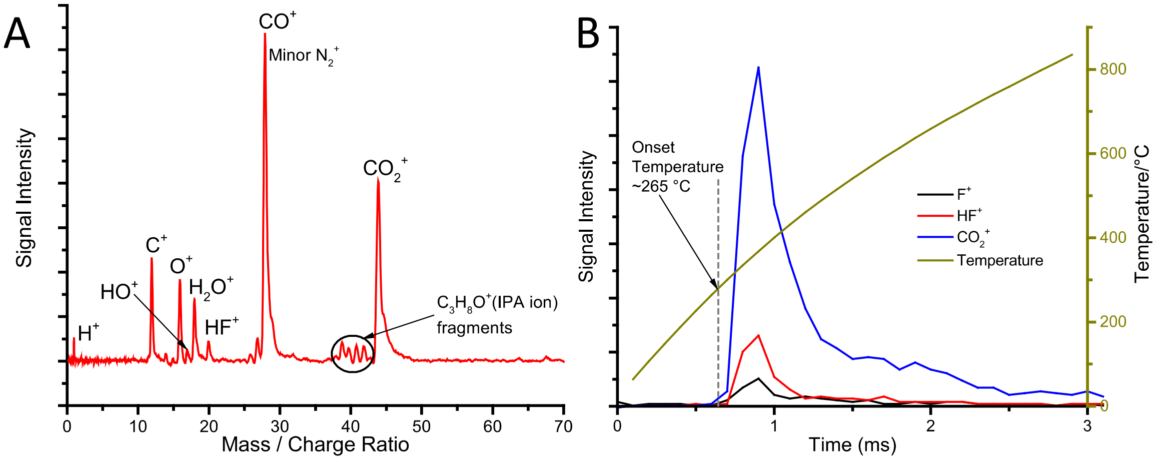

Figure 3.18 Integrated (A) and time-resolved (B) mass spectrometry results of FGO-I dispersed in IPA.

T-Jump TOFMS was employed to confirm the release of fluorine during the decomposition process found in DSC-TGA. FGO-I was dispersed in IPA under sonication right after XeF_2 fluorination to avoid any further contact with environmental moisture. The

HF^+ fluorine peak appeared in the integrated mass spectrum in Figure 3.18A, confirming the existence of fluorine in the XeF_2 treated sample. Note that H_2O^+, N_2^+ and NO^+ peaks represent unavoidable background signals. C^+, O^+, CO^+ and CO_2^+ arise from the decomposition GO and the oxygen functional groups. Additionally, the time-resolved intensity curve in Figure 3.18B clearly showed that the fluorine content was released simultaneously with CO_2^+. It is concluded that release of fluorine species occurs simultaneously with decomposition of GO, with an onset temperature of about 265 ± 50°C, consistent with the decomposition at 245°C found by the DTG and DSC results. It is interesting that mass loss started below 150°C in DSC-TGA, while the presence of the fluorine ion in mass spectrometry appeared above 250°C. It is reasonable to consider that some fluorine loss occurred during the sample preparation for mass spectrometry, especially the most loosely bound species that may escape at reduced temperatures.

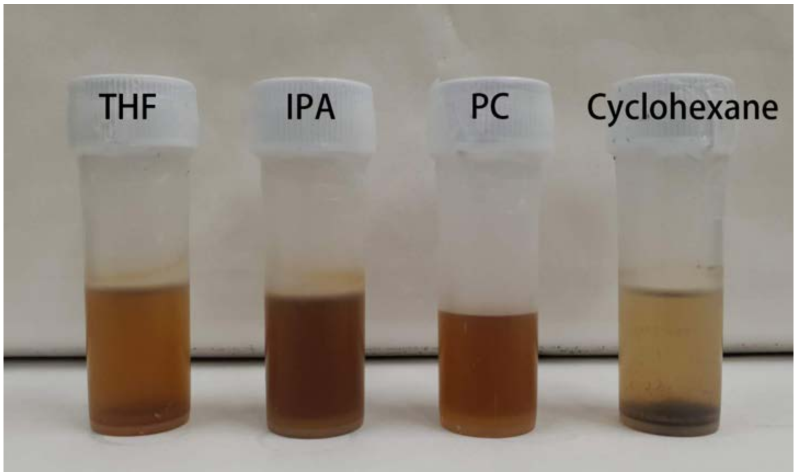

Figure 3.19 FGO dispersions in THF, IPA, PC and cyclohexane after 4 hours sonication at 2 mg / mL.

Due to the high fraction of oxygen functional groups retained after fluorination, the FGO samples can be dispersed in a variety of solvents under sonication, shown in Figure 3.19. The dispersing behavior of FGO was similar like that of GO, [48] which enhances its potential application by dispersing in different kinds of solvents. FTIR and SEM-EDS analysis of the vacuum-dried dispersions prepared in IPA, THF, propylene carbonate (PC), and cyclohexane were then obtained to determine the change in composition during sonication. All solvents were dried by molecular sieve before using. The results are shown in Figure 3.20 and Table 3.4. It is clear that extra C-H peaks showed up in all dried FGO dispersions as evidenced from 2800 – 3000 cm^{-1} in FTIR curves, which was absent in the FTIR curve of FGO-I, indicating that some suspension agent might be trapped or bonded in the dried sample. Moreover, the peak of acyl fluoride at 1840 cm^{-1} of FGO-I in Figure 3.10 almost disappeared, confirming the decomposition of acyl fluoride during sonication. Therefore, the fluorine species that loosely intercalated or bonded between graphene sheets escaped from the structure during the exfoliation of graphene under sonication. As a result, the fluorine content dropped from more than 10% in FGO-I to only 1 – 3.5% in these dried dispersions. The F/O ratio also dropped from 0.3 to only about 0.1. The remained fluorine content mostly existed in C-F covalent and semi-ionic bonds, which are thermally more stable.

Table 3.4 Element content (atomic) of vacuum dried FGO-I dispersions in THF, cyclohexane, IPA and PC, number in atomic.

Solvent	Carbon	Oxygen	Fluorine	F/O ratio
FGO-I before sonication	51.5%	36.9%	11.0%	0.306
IPA	64.6%	31.9%	3.5%	0.110
THF	78.7%	19.5%	1.8%	0.092
Cyclohexane	84.9%	13.9%	1.2%	0.085
PC	69.5%	28.4%	2.2%	0.076

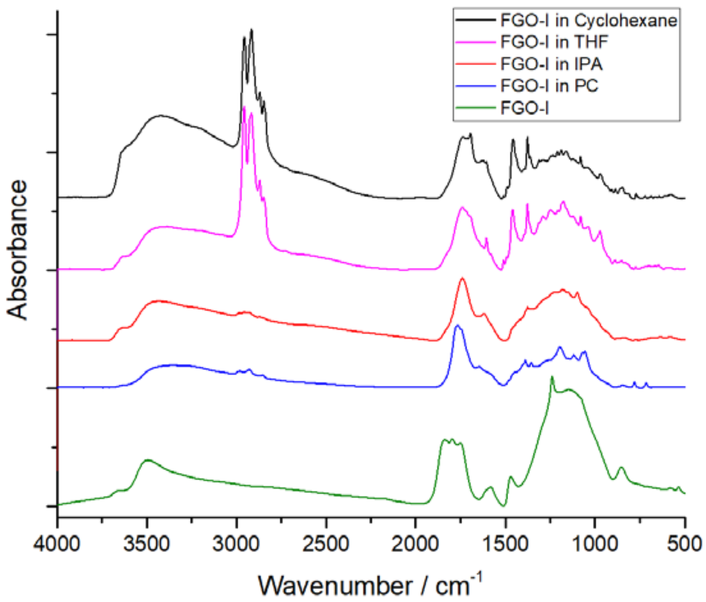

Figure 3.20 FTIR of vacuum dried FGO-I dispersions in THF, cyclohexane, IPA and PC.

These results indicate that XeF_2 can be employed as a means for the fluorination of GO to FGO while retaining a majority of oxygen functional groups. However, the fluorine content in the material degraded with time in the presence of even a relatively small quantity of water vapor (15% humidity at 25°C). Part of the fluorine content formed acyl fluoride and can be easily hydrolyzed with the moisture in atmosphere or can react with solvent during dispersing process for further utilization. Almost 40% of fluorine escaped from the material when heated to 150°C. Despite the loss of acyl fluoride during heating, some fluorine structures such as H-F molecules which are not strongly chemically bonded to graphene plane might exist in the structure. This fluorine content can be easily removed from the structure under heating to low temperature, during the exfoliation of graphene sheets under sonication, or even during storage. Therefore, fluorine showed significantly reduced stability when compared to oxygen in the FGO synthesized by GO with XeF_2.

3.6. Energetic application of FGO in FGO/Al/Bi_2O_3

Table 3.5 Energetic samples measured by DSC-TGA with different compositions. GR stands for graphene-rich, and FR stands for fuel-rich.

Sample Name and mass ratio	Mass (Total mass = 100 mg)			Remark
	GO/FGO	Al (80% active)	Bi_2O_3	
GO/Al – GR (70/30)	70 mg	30 mg	0	
FGO-I/Al – GR (70/30)	70 mg	30 mg	0	
GO/Al – FR (30/97)	23.5mg	76.5 mg	0	GO(FGO)/Al ratio same as in GO(FGO)/Al/Bi_2O_3.
FGO-I/Al – FR (30/97)	23.5 mg	76.5 mg	0	
GO/Al/Bi_2O_3 (30/97/473)	5 mg	16.2 mg	78.8 mg	5% GO(FGO) by mass. Equivalence ratio (ER) of Al/Bi_2O_3 = 1.4.
FGO-I/Al/Bi_2O_3 (30/97/473)	5 mg	16.2 mg	78.8 mg	
Al/Bi_2O_3 (97/473)	0	17 mg	83 mg	ER of Al/Bi_2O_3 = 1.4.

One of the potential applications of FGO is as a component in nanoenergetic formulations. Al nanoparticles are a common fuel and possesses a naturally formed inert Al_2O_3 shell on its surface, which protects the Al core from further oxidation under ambient conditions. Unfortunately, the shell also acts as a reaction-limiting barrier between fuel Al and oxidizer. Fluorine, however, may act to remove or weaken the Al_2O_3 shell and accelerate the reaction with solid state oxide (Al_2O_3 + "F" → AlF_3 + O, where "F" indicates a highly reactive fluorine species, and O indicates produced oxygen composites). [3] To investigate the role of FGO additives in nanoenergetic materials, DSC-TGA measurements were carried out on samples composed of GO, FGO, Al and Bi_2O_3, as summarized in Table 2. In these experiments, the relative mass of GO or FGO, Al, and

Bi_2O_3 were varied to better understand the role of FGO in the overall reactions. The introduction of Bi_2O_3 was motivated by conventional nanothermite composites that utilize a solid-state oxidizer to initiate the exothermic reaction with Al fuel. Please note that because only IPA was used as the suspension agent for FGO, the material could not facilitate good self-assembly like when DMF was used as the suspension agent for functionalized graphene. Therefore, all functionalized graphene/Al/Bi_2O_3 samples were directly dried after sonication without waiting for the occurrence of self-assembly.

A representative DSC curve of GO/Al – GR (Figure 3.21A, GR stands for graphene-rich) shows no significant reaction before melting of Al. The small exotherms between 500 – 620°C resulted from reaction between the Al core and generated OH species such as H_2O from GO, mainly from the decomposition of hydroxyl groups bonded in GO structure. These species were adsorbed on the amorphous alumina shell and reacted with Al when the core started to diffuse as the temperature was elevated above 500°C, giving the small exotherms observed. A sharp endotherm of Al melting is seen at 660°C, followed by the main exothermic reaction between Al and GO, indicating that Al primarily reacted in the liquid phase after it may readily flow out of the shell. When GO was replaced by FGO-I, the DSC indicated that the largest exothermic reaction occurred before the melting of Al. The main reaction peak between 610 to 660°C indicated that Al_2O_3 shell was weakened by the fluorine species generated from FGO-I decomposition. The expanding Al at elevated temperature was then allowed to diffuse out from the shell before reaching its melting point. The disappearance of the small exotherms between 500 – 620°C in FGO-I/Al – GR compared to GO/Al – GR was due to the removal of hydroxyl groups during fluorination. Al was not fully reacted before its melting, indicating that the fluorine and oxygen content in FGO-I was not sufficient to weaken or remove all alumina shells prior to Al melting. Some Al melted and then reacted with graphene. The total reaction energy between the two samples was similar (118 J/g for GO/Al -GR and 104 J/g for FGO-I/Al – GR), but the fraction of energy released before and after Al melting varied significantly between the two materials.

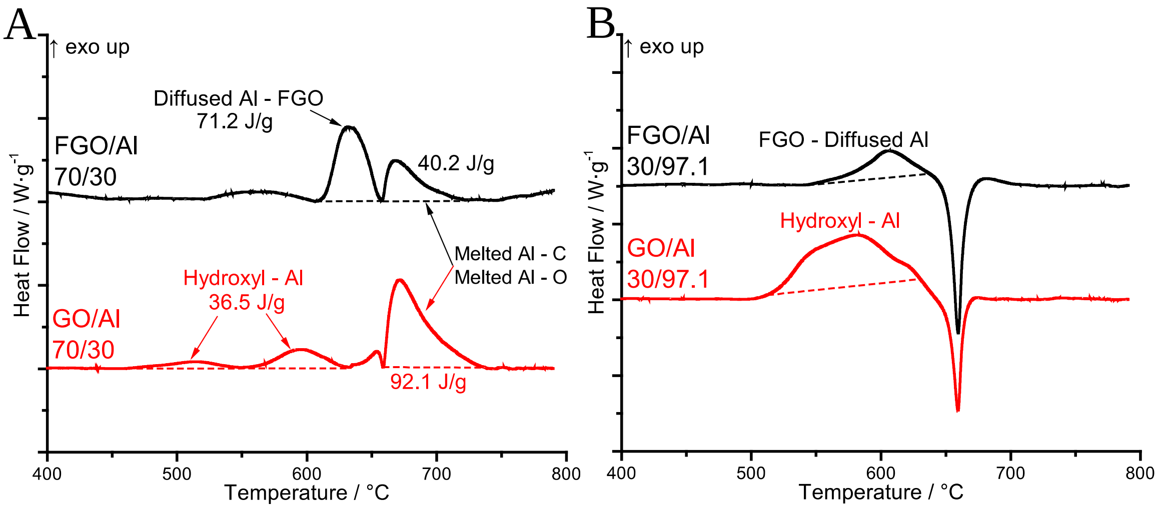

Figure 3.21 DSC results of GO/Al – GR and FGO-I/Al – GR(A), GO/Al – FR and FGO-I/Al – FR(B). Upward is exothermic.

As an additive in nanothermite composite, graphene or functionalized graphene is usually no more than 5% mass with Al and metal oxide, [42] or no more than 30% mass with Al only [49] to obtain optimized energetic performance. When assembling a composite of only GO/FGO and Al, the DSC of samples, with 23.5% FGO (GO) by mass, labeled GO/Al – FR and FGO-I/Al – FR (FR stands for fuel-rich), were analyzed, as shown in Figure 3.21B. The GO/Al – FR showed an exotherm between 520 – 600°C, as a result of the decomposed OH species penetrating the shell and reacting with the Al, similar to GO/Al – GR. Unlike in the sample with 70% of FGO (FGO-I/Al – GR) described previously, the fluorine content in the composite FGO-I/Al – FR was not enough to react extensively with diffusing Al after reacting with the alumina shell. Therefore, there was not a dominating exothermic reaction in DSC of FGO/Al-FR in Figure 3.21B like in Figure 3.21A (FGO/Al – GR) before Al melting. However, a small exotherm was observed around 610°C, which is close to the large exothermic peak in Figure 3.21A (FGO/Al – GR). This result indicated that the Al core was able to diffuse out from the shell easier and react with the FGO surrounding it before reaching melting, even the amount of FGO-I was only about 1/3 in mass compared to Al.

Based on a calculation in Chapter 3.8, the 3% fluorine in FGO by mass was not enough to react completely with the Al_2O_3 shell of Al in any of the samples listed in Table 3.5. It is notable, however, that the alumina shell does not need to be completely removed to facilitate enhanced reactions. Small pinholes or thinned walls could sufficiently accelerate the diffusion of the Al core out of the shell before its melting. As discussed above, 3% of fluorine in FGO in FGO-I/Al – FR was sufficient to react Al in the solid state. A similar scenario is present if a secondary oxidizer such as Bi_2O_3 was added to the FGO/Al composite. Partial removal or thinning of the Al_2O_3 shell by fluorine from FGO was sufficient to enable the Al/Bi_2O_3 reaction at a temperature at which Al is in the solid state.

Bi_2O_3 nanoparticles are commonly used in Al-based nanoenergetic composites due to its reaction and pressurization rate. [42, 50, 51] Introduction of Bi_2O_3 nanoparticles provided a robust solid-state oxidizer with which Al can react after escaping the Al_2O_3 encapsulating shell. Figure 3.22B shows the reaction heat of Al/Bi_2O_3 nanothermite with GO and FGO-I additives. In Al/Bi_2O_3 loose powder, the reaction initiated at 500°C due to the start of Al core diffusion out of the shell, peaked at around 615°C and was completed at about 700°C after the melting of Al. Neat Al/Bi_2O_3 mixtures are known to be inhomogeneous as a result of phase separation[42]. The low-temperature reaction likely occurred between surface contacted Al and Bi_2O_3 nanoparticles, while part of reaction occurred after the melting and free flow of Al. [50] When GO was added to the Al/Bi_2O_3 nanocomposite mixture, GO/Al/Bi_2O_3 showed the lowest onset exothermic temperature around 460°C, similar to that observed previously when testing GO/Al (70 – 30). Hydroxyl (OH) species released from GO reacted with diffused Al in the Al_2O_3 shell when the sample was heated to about 480°C. The local exothermic reactions further accelerated the diffusion and reaction of Al core. The total energy release of GO/Al/Bi_2O_3 was enhanced by approximately 20% compared to neat Al/Bi_2O_3 due to the reduced phase separation as a result of GO addition. The improved Al and Bi_2O_3 intermixing in the presence of GO reduced diffusion length scales for mass transport and the peak reaction temperature for the GO/Al/Bi_2O_3 compared to Al/Bi_2O_3. [42] After the first reaction, GO/Al/Bi_2O_3 showed a second reaction peaking at 626°C as Al reacted with Bi_2O_3 particles which were not in direct contact prior to reaction. It is notable that the melting peak of Al was observed in both Al/Bi_2O_3 loose powder and GO/Al/Bi_2O_3, indicating that part of the Al core remained unreacted prior the melting point of Al at 660°C. With the addition of FGO-I, the melting peak of Al was not observed, and the reaction was nearly completed before the melting temperature of Al. Because fluorine reacted with the alumina shells, solid state Al escaped from the Al_2O_3 shell and reacted with Bi_2O_3 nanoparticles at an onset temperature of 480°C and peak reaction temperature of 586°C, both prior to the onset of the Al melting temperature. Due to the absence of OH groups after XeF_2 fluorination, the reaction onset temperature of FGO-I/Al/Bi_2O_3 was greater than that of GO/Al/Bi_2O_3. However, the weakened Al_2O_3 shell provided by fluorine species lowered the onset temperature relative to Al/Bi_2O_3. Moreover, $FGO/Al/Bi_2O_3$ showed a total energy release of over 1100 J/g, which was 60% higher than Al/Bi_2O_3 loose powder and 45% higher than $GO/Al/Bi_2O_3$.

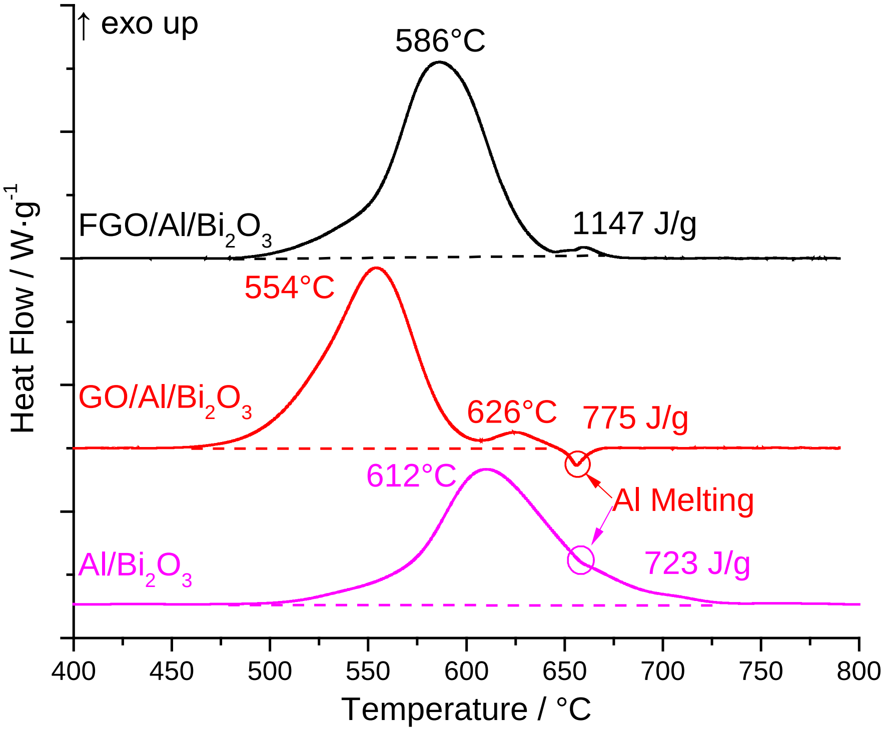

Figure 3.22 DSC results of FGO-I/Al/Bi_2O_3, $GO/Al/Bi_2O_3$ and Al/Bi_2O_3. Upward is exothermic.

3.7. Conclusion and future direction

Overall, different types of fluorinated graphene were synthesized and were shown to be good candidates for the removal of the alumina shell that natively exists on Al NP fuel. The enhanced reactivity was confirmed by the reduction of reaction temperature with Al NPs. However, all fluorinated graphene has its own disadvantage.

Fluorination of GO was achieved successfully using low-pressure processing in XeF_2 gas, and the resulting FGO was then incorporated in nanothermite composites to provide both a nanoparticle assembly scaffold and a source of reactive fluorinated species. The XeF_2 process retained the GO oxygen functional groups, enabling the easy dispersion of fluorinated GO in different solvents while also facilitating further chemical functionalization. The fluorine functional groups in the FGO, identified by FTIR, included acyl fluoride groups, carbon-fluorine covalent and semi-ionic bonds. The intercalated fluorine and highly reactive acyl fluoride in the structure were loosely bound and were reactive with atmospheric moisture, mild heating, or mild sonication. When FGO is introduced into a nanothermite composite, the fluorine species supplied by the FGO acted to etch the Al_2O_3 shell of Al nanoparticles at temperatures below the melting temperature of Al. Mass spectrometry measurements indicate that fluorine species were released at approximately 265°C, concurrent with the generation of CO_2^- from FGO decomposition. DSC measurements further showed a reduction in reaction temperature with the addition of FGO and that all Al reacted prior to the Al melting temperature in FGO/Al/Bi_2O_3 composites. Further, the all solid-state reaction between Al and Bi_2O_3 in the FGO/Al/Bi_2O_3 composites produced 58% greater energy release than Al/Bi_2O_3 loose powder. The increased energy release is attributed to both the presence of reactive fluorine species and the role of the FGO to act as an assembly template for Al and Bi_2O_3 nanoparticles to increase particle intimacy while reducing phase separation. The chemical functionalization of nanothermite assembly scaffold materials, including fluorinated GO, represents a new mechanism to control energetic material response. The loss of fluorine from the FGO during the energetic material production was critical, which is a significant disadvantage of producing FGO by using this method. FGO produced by other fluorination method, such as direct F_2 fluorination or HNO_3, HF oxidizing fluorinating method may help to produce FGO with stable and higher percentage of fluorine.

Fluorinated reduced graphene oxide was synthesized by GO and HF through hydrothermal process. However, in our condition, the fluorine loading was poor, and the reduced structure limited the self-assembly with Al NPs. To achieve higher fluorine percentage and good self-assembly with nanoenergetic particles, the synthesis of GO and fluorination hydrothermal process need to be tuned, and the dispersing methods need to be improved.

The same assembling problem also occurred on the sample of XeF_2 fluorinated commercial graphene. These materials may be applied in self-assembled nanothermite material if a better dispersing media (solvent) and dispersing method were applied.

3.8. Calculation of required fluorine content in nanothermite material

Consider 1000 mg of nanothermite composite FGO/Al/Bi_2O_3, where FGO occupied 5% of mass. Therefore, FGO represents 50 mg and Al/Bi_2O_3 is the remaining 950 mg. When equivalence ratio (ER) = 1.4, then Al nanoparticles comprise 162 mg, while Bi_2O_3 is 788 mg. The aluminum nanoparticles used in the current study contain 79% active Al. Therefore, the mass of Al_2O_3 is approximately 34.02 mg (21% of 162 mg). If Bi_2O_3 is not added to the composite, the total mass of FGO/Al nanoparticles is 212 mg (50 mg / 162 mg).

For an ideal reaction, it follows

$$Al_2O_3 + 6\,F \longrightarrow 2\,AlF_3 + 3\,O$$

In this case, the mass ratio between Al_2O_3 and F for this reaction to happen completely is

$$101.96 \text{ g/mol } (Al_2O_3) – 114 \text{ g/mol } (6 \text{ F})$$

In 212 mg of FGO/Al, the 34.02 mg (0.334 mmol) Al_2O_3 requires 38.04 mg (2.002 mmol) fluorine for complete fluorination, translating to a fluorine mass percentage in FGO to be 76.08% (38.04 mg fluorine in 50 mg FGO).

Similarly, in 1 g of FGO/Al/Bi_2O_3 (5% FGO) nanothermite, assuming fluorine completely reacted with Al_2O_3, fluorine also needs to reach a mass percentage 76.08% in FGO to completely remove the Al_2O_3 shell.

As a reference, the fluorine mass percentage in PTFE is 76.0%. PTFE has the highest fluorine mass percentage in carbon – fluorine composites since carbon skeleton is saturated by fluorine in PTFE. Therefore, the fluorine content in FGO (or FG) will not be as high as that in PTFE.

Therefore, 5% fluorinated graphene / fluorine graphene oxide additive in FG/Al/Bi_2O_3 or FGO/Al/Bi_2O_3 is insufficient to react with all alumina.

In our case, 3% fluorine in FGO after preparing the dispersion will not be able to completely remove the alumina shell. It can react with about 4% of the total alumina mass. This may be sufficient to create pinholes or thin the alumina shell such that Al may more readily diffuse from the shell at a temperature that is lower than the Al melting temperature.

3.9. Summary

This part of research focuses on the fluorination of graphene and its applications in self-assembly with energetic nanoparticles. We chose two different methods based on safety and accessibility of different synthesis routes. The HF – GO hydrothermal fluorination was expected to produce F-rGO with high fluorine loading. However, it did not work possibly due to the dedication of the process to minor environmental changes and the properties of the GO we use. Therefore, we turned to XeF_2 – GO/commercial graphene nanoplatelets reaction. The novel FGO produced by XeF_2 and GO showed very interesting chemical properties due to its high functionalized structure with both fluorine and oxygen atoms on the carbon structure. Its sensitivity to humidity limits its further application, but it is a crucial material for people to better understand the properties of graphene material with multiple functionalization. The fluorine that reminded in the assembled nanocomposite after sonication contributed to the weakening of Al_2O_3 shell and lowering of reaction temperature. The combustion behavior of the FGO/Al/Bi_2O_3 will be an interesting field to research. The biggest miss I made in this project may be the early excluding of XeF_2 – commercial graphene nanoplatelet reaction without further characterization. This material also shows significant fluorine peak in FTIR after correctly subtracting the background. It has the chance to be a more stable and better self-assembly substrate for nanoparticles, and further research should be taken on this material.

3.10. References

[1] L. Glavier *et al.*, "Nanoenergetics as pressure generator for nontoxic impact primers: Comparison of Al/Bi2O3, Al/CuO, Al/MoO3 nanothermites and Al/PTFE," *Combustion and Flame,* vol. 162, no. 5, pp. 1813-1820, 2015/05/01/ 2015.

[2] H. Wang, M. Rehwoldt, D. J. Kline, T. Wu, P. Wang, and M. R. Zachariah, "Comparison study of the ignition and combustion characteristics of directly-written Al/PVDF, Al/Viton and Al/THV composites," *Combustion and Flame,* vol. 201, pp. 181-186, 2019/03/01/ 2019.

[3] M. L. Pantoya and S. W. Dean, "The influence of alumina passivation on nano-Al/Teflon reactions," *Thermochimica Acta,* vol. 493, no. 1, pp. 109-110, 2009/09/10/ 2009.

[4] B. Chen *et al.*, "In Situ Characterization of Photothermal Nanoenergetic Combustion on a Plasmonic Microchip," *ACS Applied Materials & Interfaces,* vol. 10, no. 1, pp. 427-436, 2018/01/10 2018.

[5] V. Georgakilas *et al.*, "Functionalization of Graphene: Covalent and Non-Covalent Approaches, Derivatives and Applications," *Chemical Reviews,* vol. 112, no. 11, pp. 6156-6214, 2012/11/14 2012.

[6] O. Ruff and O. Bretschneider, "Die Reaktionsprodukte der verschiedenen Kohlenstoffformen mit Fluor II (Kohlenstoff-monofluorid)," *Zeitschrift für anorganische und allgemeine Chemie,* vol. 217, no. 1, pp. 1-18, 1934.

[7] A. M. Panich, "Nuclear magnetic resonance study of fluorine–graphite intercalation compounds and graphite fluorides," *Synthetic Metals,* vol. 100, no. 2, pp. 169-185, 1999/04/12/ 1999.

[8] W. Tiedemann, "Electrochemical Behavior of the Fluorographite Electrode in Nonaqueous Media," *Journal of The Electrochemical Society,* vol. 121, no. 10, pp. 1308-1311, October 1, 1974 1974.

[9] R. J. Lagow, R. B. Badachhape, J. L. Wood, and J. L. Margrave, "Some new synthetic approaches to graphite–fluorine chemistry," *Journal of the Chemical Society, Dalton Transactions,* 10.1039/DT9740001268 no. 12, pp. 1268-1273, 1974.

[10] W. Rüdorff, "Graphite Intercalation Compounds," in *Advances in Inorganic Chemistry and Radiochemistry,* vol. 1, H. J. Emeléus and A. G. Sharpe, Eds.: Academic Press, 1959, pp. 223-266.

[11] H. E. Sliney, "Graphite Fluoride (CFx)n—A New Solid Lubricant AU - Fusaro, Robert L," *A S L E Transactions,* vol. 13, no. 1, pp. 56-65, 1970/01/01 1970.

[12] X. Chia, A. Ambrosi, M. Otyepka, R. Zbořil, and M. Pumera, "Fluorographites (CFx)n Exhibit Improved Heterogeneous Electron-Transfer Rates with Increasing Level of Fluorination: Towards the Sensing of Biomolecules," *Chemistry – A European Journal,* vol. 20, no. 22, pp. 6665-6671, 2014.

[13] C. Delabarre, M. Dubois, J. Giraudet, K. Guérin, and A. Hamwi, "Electrochemical performance of low temperature fluorinated graphites used as cathode in primary lithium batteries," *Carbon,* vol. 44, no. 12, pp. 2543-2548, 2006/10/01/ 2006.

[14] S. Ebnesajjad, *Expanded PTFE Applications Handbook: Technology, Manufacturing and Applications*. Elsevier, 2016, p. 300.

[15] A. L. Logothetis, "Chemistry of fluorocarbon elastomers," *Progress in Polymer Science,* vol. 14, no. 2, pp. 251-296, 1989/01/01/ 1989.

[16] C. D. James and G. W. Franklin, "Fluorocarbon vinyl ether polymers," United Stated, 1967.

[17] R. Taylor *et al.*, "Nucleophilic substitution of fluorinated C60," *Journal of the Chemical Society, Chemical Communications,* 10.1039/C39920000665 no. 9, pp. 665-667, 1992.

[18] A. Hamwi, H. Alvergnat, S. Bonnamy, and F. Béguin, "Fluorination of carbon nanotubes," *Carbon,* vol. 35, no. 6, pp. 723-728, 1997/01/01/ 1997.

[19] E. T. Mickelson, C. B. Huffman, A. G. Rinzler, R. E. Smalley, R. H. Hauge, and J. L. Margrave, "Fluorination of single-wall carbon nanotubes," *Chemical Physics Letters,* vol. 296, no. 1, pp. 188-194, 1998/10/30/ 1998.

[20] M. Adamska and U. Narkiewicz, "Fluorination of Carbon Nanotubes − A Review," *Journal of Fluorine Chemistry,* vol. 200, pp. 179-189, 2017/08/01/ 2017.

[21] J. T. Robinson *et al.*, "Properties of Fluorinated Graphene Films," *Nano Letters,* vol. 10, no. 8, pp. 3001-3005, 2010/08/11 2010.

[22] X. Yang, X. Jia, and X. Ji, "Acid induced fluorinated graphene oxide," *RSC Advances,* 10.1039/C4RA13884H vol. 5, no. 13, pp. 9337-9340, 2015.

[23] A. K. Geim and K. S. Novoselov, "The rise of graphene," (in English), *Nature Materials,* Article vol. 6, no. 3, pp. 183-191, Mar 2007.

[24] K. P. Loh, Q. Bao, P. K. Ang, and J. Yang, "The chemistry of graphene," *Journal of Materials Chemistry,* 10.1039/B920539J vol. 20, no. 12, pp. 2277-2289, 2010.

[25] H. An *et al.*, "Hydrothermal preparation of fluorinated graphene hydrogel for high-performance supercapacitors," *Journal of Power Sources,* vol. 312, no. Supplement C, pp. 146-155, 2016/04/30/ 2016.

[26] S. Huang *et al.*, "Nitrogen and fluorine co-doped graphene as a high-performance anode material for lithium-ion batteries," *Journal of Materials Chemistry A,* 10.1039/C5TA06012E vol. 3, no. 46, pp. 23095-23105, 2015.

[27] N. Liaros, A. B. Bourlinos, R. Zboril, and S. Couris, "Fluoro-graphene: nonlinear optical properties," *Optics Express,* vol. 21, no. 18, pp. 21027-21038, 2013/09/09 2013.

[28] F. Withers, M. Dubois, and A. K. Savchenko, "Electron properties of fluorinated single-layer graphene transistors," *Physical Review B*, vol. 82, no. 7, p. 073403, 08/06/ 2010.

[29] W. Feng, P. Long, Y. Feng, and Y. Li, "Two-Dimensional Fluorinated Graphene: Synthesis, Structures, Properties and Applications," *Advanced Science,* vol. 3, no. 7, p. 1500413, 2016/07/01 2016.

[30] R. Stine, W.-K. Lee, K. E. Whitener, J. T. Robinson, and P. E. Sheehan, "Chemical Stability of Graphene Fluoride Produced by Exposure to XeF2," *Nano Letters,* vol. 13, no. 9, pp. 4311-4316, 2013/09/11 2013.

[31] Y.-Y. Yu, B. H. Kang, Y. D. Lee, S. B. Lee, and B.-K. Ju, "Effect of fluorine plasma treatment with chemically reduced graphene oxide thin films as hole transport layer in organic solar cells," *Applied Surface Science,* vol. 287, pp. 91-96, 2013/12/15/ 2013.

[32] S. B. Bon *et al.*, "Plasma Fluorination of Chemically Derived Graphene Sheets and Subsequent Modification With Butylamine," *Chemistry of Materials,* vol. 21, no. 14, pp. 3433-3438, 2009/07/28 2009.

[33] K. Tahara, T. Iwasaki, A. Matsutani, and M. Hatano, "Effect of radical fluorination on mono- and bi-layer graphene in Ar/F2 plasma," *Applied Physics Letters,* vol. 101, no. 16, p. 163105, 2012/10/15 2012.

[34] Z. Wang *et al.*, "Synthesis of fluorinated graphene with tunable degree of fluorination," *Carbon,* vol. 50, no. 15, pp. 5403-5410, 2012/12/01/ 2012.

[35] K. Samanta *et al.*, "Highly hydrophilic and insulating fluorinated reduced graphene oxide," *Chemical Communications,* 10.1039/C3CC45376F vol. 49, no. 79, pp. 8991-8993, 2013.

[36] P. Gong *et al.*, "Photochemical synthesis of fluorinated graphene via a simultaneous fluorination and reduction route," *RSC Advances,* 10.1039/C3RA22029J vol. 3, no. 18, pp. 6327-6330, 2013.

[37] M. Dubois *et al.*, "Thermal exfoliation of fluorinated graphite," *Carbon,* vol. 77, pp. 688-704, 2014/10/01/ 2014.

[38] C. Sun, Y. Feng, Y. Li, C. Qin, Q. Zhang, and W. Feng, "Solvothermally exfoliated fluorographene for high-performance lithium primary batteries," *Nanoscale,* 10.1039/C3NR04609E vol. 6, no. 5, pp. 2634-2641, 2014.

[39] X. Wang *et al.*, "High-Yield Production of Highly Fluorinated Graphene by Direct Heating Fluorination of Graphene-oxide," *ACS Applied Materials & Interfaces,* vol. 5, no. 17, pp. 8294-8299, 2013/09/11 2013.

[40] Y. X. Xu, K. X. Sheng, C. Li, and G. Q. Shi, "Self-Assembled Graphene Hydrogel via a One-Step Hydrothermal Process," *Acs Nano,* vol. 4, no. 7, pp. 4324-4330, Jul 2010.

[41] J. G. S. Moo, B. Khezri, R. D. Webster, and M. Pumera, "Graphene Oxides Prepared by Hummers', Hofmann's, and Staudenmaier's Methods: Dramatic Influences on Heavy-Metal-Ion Adsorption," *ChemPhysChem,* vol. 15, no. 14, pp. 2922-2929, 2014/10/06 2014.

[42] R. Thiruvengadathan *et al.*, "A Versatile Self-Assembly Approach toward High Performance Nanoenergetic Composite Using Functionalized Graphene," *Langmuir,* vol. 30, no. 22, pp. 6556-6564, Jun 2014.

[43] G. Jian, L. Zhou, N. W. Piekiel, and M. R. Zachariah, "Low Effective Activation Energies for Oxygen Release from Metal Oxides: Evidence for Mass-Transfer Limits at High Heating Rates," *ChemPhysChem,* vol. 15, no. 8, pp. 1666-1672, 2014/06/06 2014.

[44] A. P. Kharitonov, "Practical applications of the direct fluorination of polymers," *Journal of Fluorine Chemistry,* vol. 103, no. 2, pp. 123-127, 2000/04/24/ 2000.

[45] W. Zhang *et al.*, "Comparative Study of SWCNT Fluorination by Atomic and Molecular Fluorine," *Chemistry of Materials,* vol. 24, no. 10, pp. 1744-1751, 2012/05/22 2012.

[46] S. Park, J. An, J. R. Potts, A. Velamakanni, S. Murali, and R. S. Ruoff, "Hydrazine-reduction of graphite- and graphene oxide," *Carbon,* vol. 49, no. 9, pp. 3019-3023, 2011/08/01/ 2011.

[47] M. P. Araújo, O. S. G. P. Soares, A. J. S. Fernandes, M. F. R. Pereira, and C. Freire, "Tuning the surface chemistry of graphene flakes: new strategies for selective oxidation," *RSC Advances,* 10.1039/C6RA28868E vol. 7, no. 23, pp. 14290-14301, 2017.

[48] J. I. Paredes, S. Villar-Rodil, A. Martinez-Alonso, and J. M. D. Tascon, "Graphene oxide dispersions in organic solvents," (in English), *Langmuir,* Article vol. 24, no. 19, pp. 10560-10564, Oct 2008.

[49] Y. Jiang *et al.*, "Energetic Performance of Optically Activated Aluminum/Graphene Oxide Composites," *ACS Nano,* vol. 12, no. 11, pp. 11366-11375, 2018/11/27 2018.

[50] A. Wang *et al.*, "Reactive nanoenergetic graphene aerogel synthesized by one-step chemical reduction," *Combustion and Flame,* vol. 196, pp. 400-406, 2018/10/01/ 2018.

[51] R. Thiruvengadathan *et al.*, "Enhanced Combustion Characteristics of Bismuth Trioxide-Aluminum Nanocomposites Prepared through Graphene Oxide Directed Self-Assembly," *Propellants Explosives Pyrotechnics,* vol. 40, no. 5, pp. 729-734, Oct 2015.

Chapter 4

Iodinated Reduced Graphene Oxide (I-rGO) and its Application in Self-Assembled Nanoenergetic Materials

4.1. Introduction

In addition to fluorine, another halogen element, iodine, has been identified a good candidate as the oxidizer in Al-based nanothermite material. Although iodine is not as electronegative as oxygen, it can weaken the alumina shell by forming Al-O-I bond on it. [1] The reactions between Al_2O_3 and highly reactive I_xO_y fragments from the decomposition of iodine oxidizer are mostly exothermic and give negative change in Gibbs free energy, indicating that these reactions are spontaneous. [2] Therefore, different kinds of iodine oxide and iodic acid have been adopted to synthesize nanothermite composites with aluminum nanoparticles, such as I_2O_5, I_4O_9, HI_3O_8 and HIO_3. [3-6] Pre-ignition exothermic reactions were observed in Al/I_2O_5 nanothermite during slow heating in DSC-TGA at 310°C, much lower than the melting point of Al or the normal reaction temperature range between Al and oxidizer nanoparticles, indicating the strong reaction between alumina shell and the iodine oxidizer. [1] Additionally, iodine is well-known for its excellent biocidal properties and neutralization effect. [7, 8] Therefore, the high temperature generated during the reaction of energetic material and the vaporized iodine at that temperature can efficiently neutralize bacteria or even deal with bioweapons. [4, 9] Both iodine oxidizer and iodine can be utilized as iodine source in iodine biocidal nanothermite materials. [10, 11]

Iodinated graphene has drawn people's interest in the recent years vastly due to its potential as catalyst, [12] lithium ion battery electrodes, [13] and semiconductors. [14] Moreover, both as halogenated graphene, the relatively weaker C-I bond compared to covalent and semi-ionic C-F bond in conventional fluorinated graphene allows iodinated graphene not only for the chance of further modification or for reversible halogen storage, [15] but also as a flame retardant [16] or bio-inhibitor. [4, 17] Iodinated graphene sheets may be synthesized at room temperature or elevated temperature by immersing GO in hydroiodic acid (HI),[18] or by introducing iodine vapor at elevated temperature.[19] The application of iodinated graphene may be expanded if it is functionalized further and modified to create iodinated graphene composites. These iodinated graphene composites can serve as a carrier for particles [20] or provide a mechanism for self-assembly with different nanoparticles. [21]

Therefore, iodinated graphene has a promising potential as the self-assembly scaffold for nanoenergetic materials and provide biocidal iodine during the energetic reaction.

4.2. Synthesis

The iodination process utilized the as-prepared GO paper and hydroiodic acid (57 wt%, not stabilized or stabilized by 1.5% H_3PO_2, Sigma Aldrich, St Louis, MO) at room temperature. In a typical synthesis process, 30 mg of GO paper was immersed into 15 mL HI acid in a 50 mL centrifuge tube. After 1 hour of reaction at room temperature, the iodinated rGO paper was removed from HI and washed by methanol / DI water ($V_{methanol}/V_{water} = 1.0$) twice, then by DI water repeatedly to remove all residual acid. The final product was dried under vacuum overnight at room temperature. Commercially available HI solutions are categorized as stabilized HI and non-stabilized HI. Note that I^- in the non-stabilized HI solution will be oxidized spontaneously by the oxygen in atmosphere and form polyiodides I_3^- and I_5^-, showing a color of dark brown. Stabilized HI contains H_3PO_2 as a reducer to stabilize I^-. Therefore, the stabilized HI shows a light-yellow color. To distinguish between materials produced between stabilized and non-stabilized HI, I-rGO produced by stabilized HI will be referred to as I-rGO-S, while I-rGO produced by non-stabilized HI will be referred to as I-rGO-NS.

The application of I-rGO in solution-based assembly relies on the ability to disperse I-rGO into a solvent with minimal loss of iodine content. The dispersion of I-rGO in organic solvents was conducted by cutting I-rGO sheets into small pieces (~3 mm by 3 mm) and placing them in different solvents at a concentration of 1.0 mg / mL. The mixtures were then treated by either sonication or mechanical vortexing for 4 hours. Dimethylformamide (DMF, Fisher Scientific), iso-propyne alcohol (IPA, Fisher Scientific) and cyclohexane (Sigma Aldrich) were used as dispersive media.

To prepare the I-rGO/Al and I-rGO/Al/Bi_2O_3 self-assembled nanothermite structures, I-rGO-S was first dispersed in DMF at 1 mg / mL for 4 hours to form a homogeneous dispersion in the sonic bath. Simultaneously, Al and Bi_2O_3 were separately dispersed in IPA using sonication. I-rGO-S / DMF was then mixed with Al / IPA and sonicated for 1 hour. Finally, Bi_2O_3 / IPA was added to the solution and sonicated for another hour. The homogeneous mixture was then left overnight for self-assembly. After the self-assembled I-rGO/Al and I-rGO/Al/Bi_2O_3 precipitated from the dispersion, the supernatant was discarded, and the precipitation was washed by IPA 4 times and dried under vacuum to obtain the final product.

Different characterization methods were used to measure the structural, elemental and energetic properties of I-rGO, including SEM-EDS, Raman spectrum, XRD, DSC-TGA, and ESD sensitivity test.

4.3. Structural analysis of I-rGO

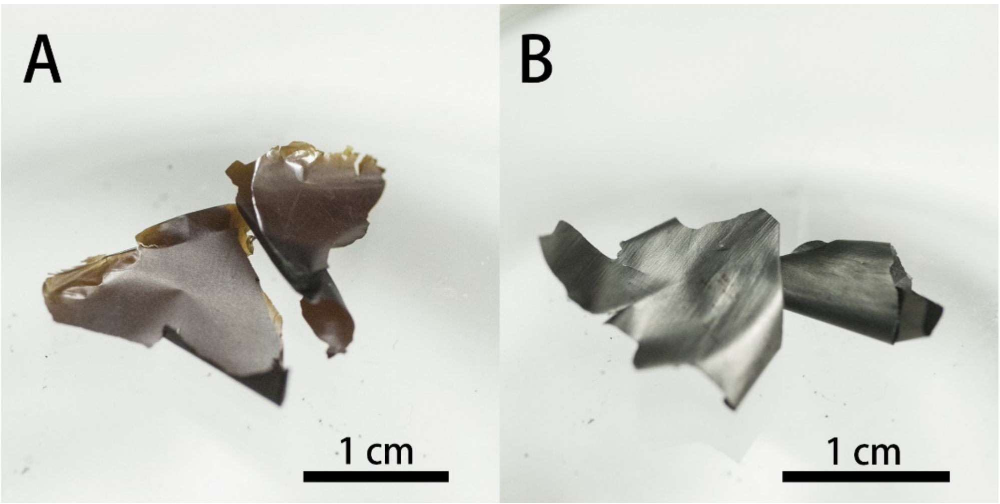

Figure 4.1 Photographs of GO sheet (left) and I-rGO sheet (right).

After reaction with hydroiodic acid, graphene oxide sheets were not only iodinated but also reduced by HI, forming iodinated reduced graphene oxide (I-rGO). As shown in Figure 4.1, the I-rGO sheet exhibited a silver, shiny metallic color, significantly different in appearance than the original graphene oxide sheet, which was dark brown. The increased reflectivity was representative of a chemically reduced GO structure. The resistance of the GO sheet was too large to be measured by the four-probe system (>50 MΩ/sq). However, after reacting with HI, the sheet resistance of the I-rGO sheets decreased greatly to ~30 Ω/sq, due to the chemical reduction of GO and the chemical doping of iodine in the structure of I-rGO.[18] XRD results in Figure 4.2 and Table 4.1 revealed differences in crystallization for graphite, GO and I-rGO. After oxidation, the lattice distance between carbon layers was significantly increased due to the large amount of oxygen functional groups residing on the surface of graphene sheets. Graphite showed a characteristic 2θ peak at 26.5°, correlating to a distance of 0.336 nm between lattices, while the graphitic peak of the functionalized graphene layers of the graphene oxide shifted to 11.8°, increasing the distance between the lattice planes to 0.749 nm. After GO was reduced by HI, the graphitic peak shifted to 24.0° (0.370 nm lattice distance) for both I-rGO-S and I-rGO-NS due to the removal of most of the oxygen functional groups.[13] Graphite exhibited the smallest full-width-at-half-maximum (FWHM) of 0.46° due to its pristine crystal structure. Meanwhile, GO (1.28°) and I-rGO (4.63° for I-rGO-S, 1.96° for I-rGO-NS) showed much larger FWHM for the graphitic peak, indicating the disordered structure due to the presence of defects in the structure after oxidation and reduction.[22]

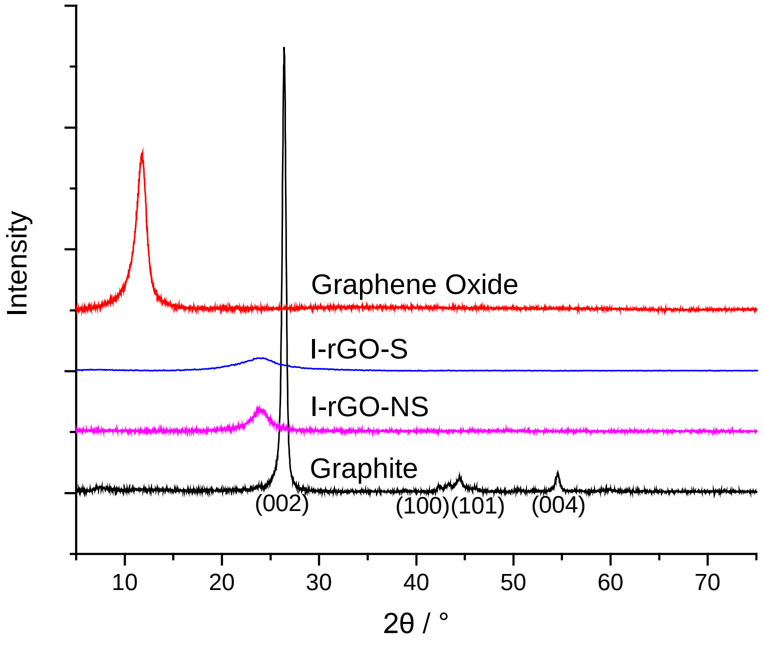

Figure 4.2 XRD plots of graphite (raw material for GO), GO and I-rGO.

Table 4.1 Detailed XRD data of graphite, graphene oxide and iodinated reduced graphene oxide.

Sample	Peak position (2θ)	d spacing	FWHM
Graphite	26.5°	0.336 nm	0.46°
Graphene oxide	11.8°	0.749 nm	1.28°
I-rGO-S	24.0°	0.370 nm	4.63°
I-rGO-NS	24.0°	0.370 nm	1.96°

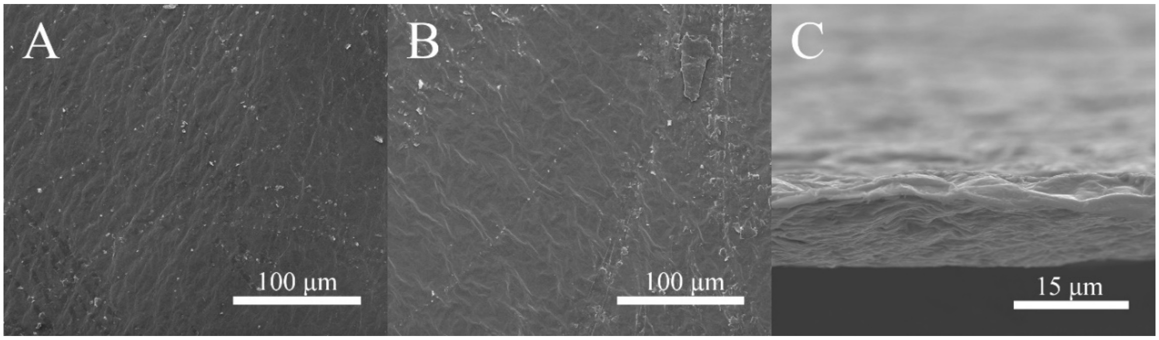

Figure 4.3 SEM pictures of I-rGO surface prepared by stabilized HI (A), non-stabilized HI (B), cross-section view (C) of I-rGO prepared by stabilized HI.

The microscale structure of I-rGO paper observed in SEM is shown in Figure 4.3. The I-rGO papers produced by both stabilized HI (Figure 4.3A) and non-stabilized HI (Figure 4.3B) showed a smooth and homogeneous surface. Some characteristic wrinkles appeared due to the high number of defects in the structure of I-rGO. The cross-sectional view of the paper (Figure 4.3C) clearly indicated the layered structure of I-rGO after the reduction. The reduced graphene oxide layers are closely stacked together, with a thickness of approximately 10 μm.

As shown in Table 4.2, EDS analysis showed that I-rGO synthesized by stabilized and non-stabilized HI demonstrated similar C/O ratios but significantly different iodine content. In non-stabilized HI, iodine ions were oxidized by the air during processing and formed polyiodide ions including I_3^- and I_5^-, which could intercalate into graphene sheets after iodination. [23] While in stabilized HI, H_3PO_2 was added as a reducer in the solution to avoid the formation of polyiodide ions. Iodination and reduction of graphene oxide occurred simultaneously since iodine ions (I^-) acted as both a dopant and a reducer. I-rGO-S was more reduced (C/O ratio of 7.40) than I-rGO-NS (C/O ratio of 6.65) due to the higher concentration of highly reductive I^-. The iodine represented a 10 ~ 25% mass percentage in the final I-rGO product, corresponding to an atomic ratio of 1-3%. The observed atomic percentage of iodine was much lower than fluorinated graphene oxide, due to a much weaker carbon-iodine bond compared to the carbon-fluorine bond. The significant difference of iodine percentage between I-rGO-S and I-rGO-NS resulted from different iodine species, which is further confirmed by Raman spectroscopy.

Table 4.2 EDS elemental analysis results of GO and I-rGO.

Element	I-rGO by stabilized HI		I-rGO by non-stabilized HI	
	Mass pct.	Atomic pct.	Mass pct.	Atomic pct.
Carbon	75.15±6.06%	86.91±7.01%	62.49±5.10%	84.16±6.87%
Oxygen	13.51±1.33%	11.74±1.16%	12.52±1.20%	12.66±1.21%
Iodine	11.34±1.15%	1.25±0.13%	24.99±2.36%	3.18±0.30%

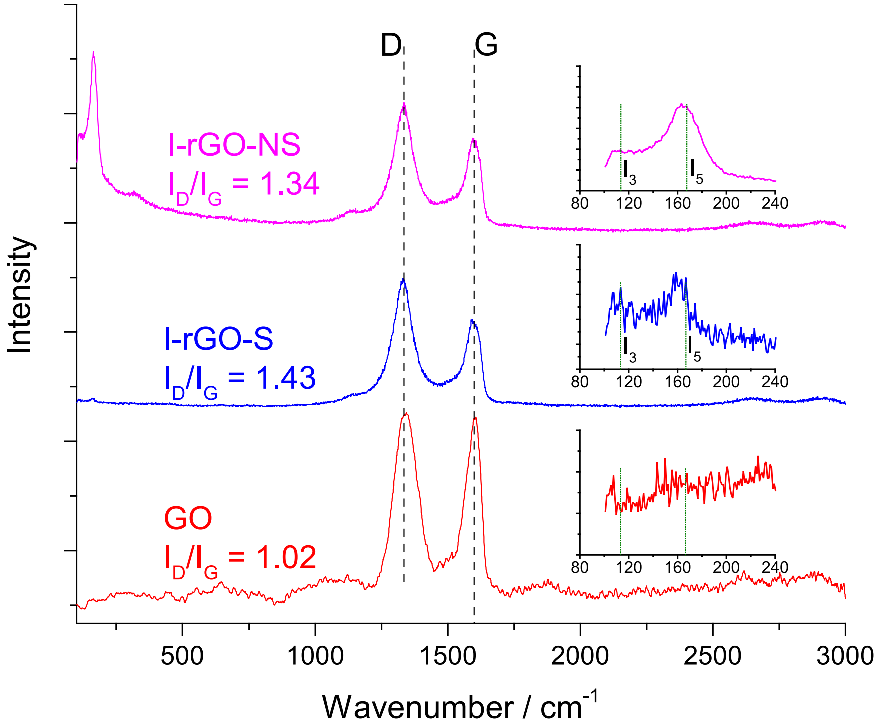

Figure 4.4 Raman spectrum of GO and I-rGO.

The stable states of iodine in iodine-doped graphene include I_1, I_3 and I_5. [24] These polyiodides (I_3 and I_5) are Raman active, facilitating compositional characterization using Raman spectroscopy. [25] The Raman spectrum of GO and I-rGO are shown in Figure 4.4. A strong D-peak (defects in graphene samples) and G-peak (carbon-carbon stretch) were found in all samples. The increased I_D/I_G ratio from GO (1.02) to I-rGO samples (1.43 for I-rGO-S and 1.34 for I-rGO-NS) indicates that additional defects were generated on the graphene lattice after the reduction and iodination. The strong signals in the low wavenumber region represent polyiodide ions, including the stretching bands of I_3^- at 113 cm^{-1} and of I_5^- at 166 cm^{-1}. These peaks were dominant in I-rGO-NS, giving an I_{I_5}/I_G ratio of 1.86, which can be utilized as an indicator of polyiodide content in I-rGO. However, in contrast, the peaks of polyiodide in I-rGO-S were small, with an I_{I_5}/I_G ratio of only 0.06. The difference in the signal intensity of polyiodide groups indicated the iodine contents in I-rGO-S and I-rGO-NS were significantly different. When non-stabilized HI was applied as the reducer for GO, polyiodide ions intercalated between graphene sheets during the reduction process and were retained within the structure after the sample was dried. [26] When stabilized HI was utilized to reduce GO, the I_2 and polyiodides formed from the redox reaction between iodine ion (I^-) and GO would be easily reduced to iodine ions (I^-) by the H_3PO_2 in the solution. This is further confirmed by the observed color change within the solution during process. The solution initially turned dark within a few minutes after GO was added, but it changed to light yellow after 1 hour when the reaction was completed. Therefore, in I-rGO-S, the iodine content mostly consisted of single iodine atoms bonded to graphene sheets, while iodine content in I-rGO-NS contributed large quantities of polyiodides that bonded to or intercalated between graphene sheets in addition to iodine atoms. [16, 27]

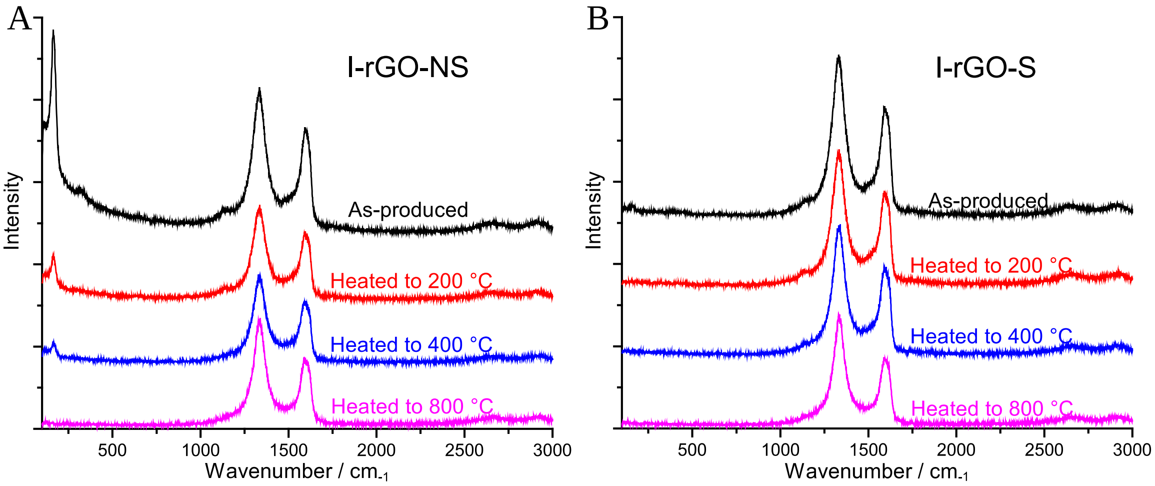

Figure 4.5 Raman spectrum of I-rGO-NS (left) and I-rGO-S (right) after heating to different temperatures.

Table 4.3 Raman and EDS results of GO and I-rGO after heated to different temperatures.

Material	Temperature	EDS (Mass pct.)			Iodine atomic pct.	Raman	
		Carbon	Oxygen	Iodine		I_D/I_G	I_{I_5}/I_G
I-rGO-S	25 (As prepared)	75.15%	13.51%	11.34%	1.24%	1.43	0.06
	200	79.25%	13.16%	7.54%	0.79%	1.42	/
	400	83.5%	9.28%	7.22%	0.75%	1.47	/
	800	92.62%	4.46%	2.88%	0.28%	1.58	/
I-rGO-NS	25 (As prepared)	62.49%	12.52%	24.99%	3.18%	1.34	1.86
	200	71.14%	12.05%	16.76%	1.94%	1.37	0.68
	400	78.82%	9.46%	11.5%	1.25%	1.41	0.39
	800	89.14%	4.4%	6.46%	0.66%	1.57	/

The thermal stability of I-rGO was analyzed by TGA analysis, as shown in Figure 4.6. The element composition of I-rGO was also measured by EDS after terminating the TGA process at different peak temperatures (200°C, 400°C, 800°C), as shown in Table 4.3 and Figure 4.6. The EDS measurements facilitated a correlation between TGA mass loss and compositional changes within the I-rGO samples. I-rGO-S showed a smooth weight loss during the heating process, with no sharp drops. The total weight loss was 26% at 800°C, mostly from the loss of iodine and oxygen functional groups. The loss of iodine occurred over the duration of the heating process, even below 200°C, while the loss of oxygen mainly occurred at higher temperatures. Since the removal of labile oxygen functional groups, such as epoxyl and hydroxyl groups, occurs at temperatures between

100 ~ 210°C, [28-30] the minor oxygen change observed for I-rGO samples heated to 200°C indicates that most epoxyl and hydroxyl groups were reduced or replaced by iodine during the reaction. The small polyiodide peak in Raman spectra of I-rGO-S was lost after heating to only 200°C, indicating an unstable nature of polyiodide in the I-rGO structure. Less than 20% of the iodine remained in I-rGO-S after heating to 800°C. The I-rGO-NS samples exhibited a sharp weight loss from 85 to 200°C, as half of the original iodine was lost from the structure. The loss of unstable polyiodide species with only mild heating was confirmed by a drastic decrease of I_{I_5}/I_G observed in Raman spectrum results (Figure 4.5). However, in contrast to I-rGO-S, the I_5^- in Raman spectrum of I-rGO-NS remained observable even as the sample was heated to 400°C. I_D/I_G of both I-rGO-S and I-rGO-NS showed similar increasing trends with heating, indicating the appearance of more defects in the graphene structure appeared from the thermal decomposition.

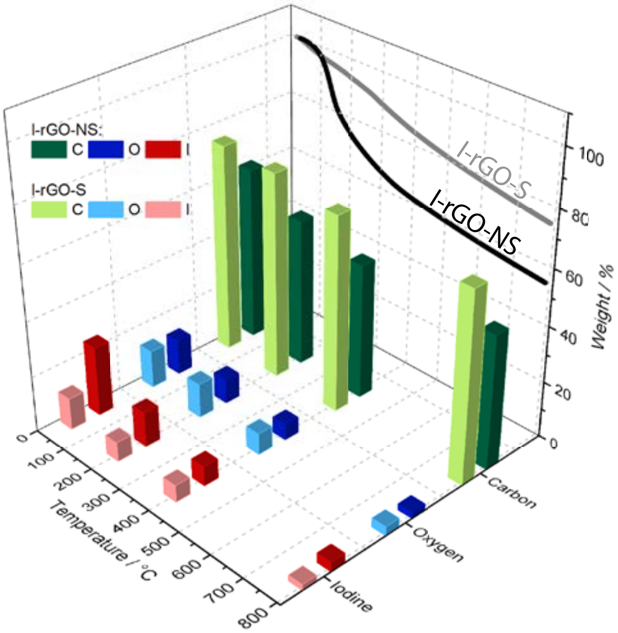

Figure 4.6 TGA results (left axis) and composition compared to original mass (right axis) of I-rGO-S and I-rGO-NS.

The ability of I-rGO to be dispersed in different solvents while retaining functionalization is foundational for making I-rGO-based composites in solution. I-rGO has a highly reduced graphene structure. Additionally, the iodine content has a very similar electronegativity compared to carbon and forms a very weakly polar C-I bond. Therefore, unlike GO which can form hydrogen bond and strong polar interactions with the solvent, [31] I-rGO could not establish strong intermolecular interaction with most organic solvents, leading to its relatively poor dispersity. We tried to disperse I-rGO in different solvents, including DMF, iso-propanol (IPA) and cyclohexane using a sonication bath for 4 hours. As a reference, the I-rGO sheets were also placed in these solvents and vortexed for 4 hours. Pictures of the mixtures are shown in Figure 4.7. Figure 4.7A demonstrates that the solution's color changed significantly for I-rGO-NS mixtures, even without sonication to exfoliate the graphene layers. DMF, IPA and cyclohexane can all dissolve the polyiodide from the structure of I-rGO-NS without exfoliating the graphene sheets under mild vortexing. Iodine in I-rGO-S was not dissolved by IPA or cyclohexane because iodine was mostly in the form of single atom, which were bonded to the graphene sheets. However, DMF could still dissolve iodine from I-rGO-S to some degree, as observed by the color change in Figure 4.7A. When the I-rGO / suspension agent mixtures were sonicated, a color change between suspension agent was observed. Cyclohexane did not support the dispersion of either I-rGO-S or I-rGO-NS. Most I-rGO sheets precipitated to the bottom of the vial. The darker purple color for I-rGO-NS / cyclohexane in Figure 4.7B and C indicated that significant quantities of iodine were dissolved in cyclohexane. IPA could partially disperse I-rGO-S (some pieces remained on the bottom of the vial), but it could not disperse I-rGO-NS at all. The sonication of I-rGO-NS in IPA or cyclohexane liberated more iodine than vortexing, as observed in the color of the supernatant. DMF was found to be the best solvent among the three to disperse I-rGO. Both I-rGO-S and I-rGO-NS can be exfoliated in DMF using sonication. The I-rGO-S / DMF dispersion was stable for several days, but I-rGO-NS precipitated out after resting for 1 hour.

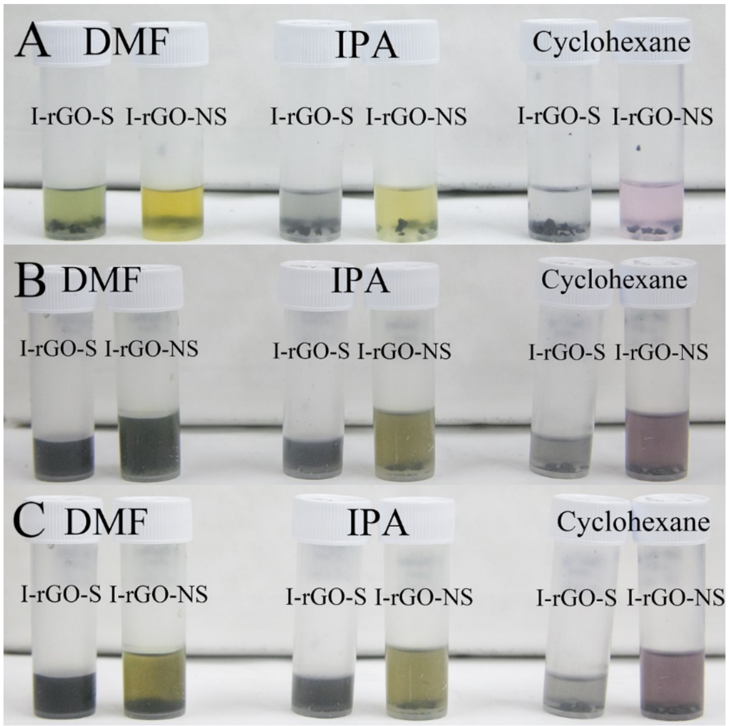

Figure 4.7 Pictures of I-rGO in different solvents after vortexing (A), immediately after sonication (B) and 1 hour after sonication (C).

To understand the loss of iodine during dispersion of the material in different solvents, the I-rGO/solvent products shown in Figure 4.7 were dried under vacuum at room temperature after discarding the supernatant. Raman spectroscopy and EDS analysis were then carried out on the dried I-rGO material, with the results summarized in Table 4.4. The iodine content varied significantly after vortexing and sonication in different solvents. When I-rGO was immersed in IPA and cyclohexane without sonication, the mass percentage of iodine in both I-rGO-S and I-rGO-NS did not change significantly. The

Raman intensity of polyiodide also did not change significantly, indicating both IPA and cyclohexane could not dissolve iodine from the I-rGO structure without exfoliating the graphene sheets. When sonication was applied to the material to exfoliate the graphene structure, the difference between IPA and cyclohexane appeared. The iodine content by mass was reduced from ~25% to ~15% for I-rGO-NS in IPA and cyclohexane after sonication, indicating that nearly half the iodine escaped from the structure of I-rGO into the solvent during exfoliation. However, the iodine content did not change as significantly for I-rGO-S in IPA and cyclohexane after sonication, indicating the bonded atomic iodine remained stable in the structure after partial exfoliation. Therefore, the loss of iodine for I-rGO-NS in IPA and cyclohexane after sonication was mostly due to the loss of polyiodide from the structure. Sonication of I-rGO in IPA caused slightly more loss of iodine than in cyclohexane due to the increased exfoliation in IPA. DMF, by contrast, caused significant loss of iodine when dispersing I-rGO-NS, even without sonication, indicating that DMF was able to dissolve iodine from I-rGO-NS without exfoliating the graphene sheets. More importantly, both I-rGO-S and I-rGO-NS showed similar iodine content after sonication or vortexing, indicating the “stable” iodine in both I-rGO-S and I-rGO-NS were in similar form, probably atomic iodine bonded to graphene layer. This is confirmed by the absence of polyiodide peak in Raman spectrum. In summary, I-rGO was not easily dispersed in IPA and cyclohexane. I-rGO-S was well dispersed in DMF but dispersing I-rGO-NS was not as effective and led to significant loss of polyiodides from the structure.

Table 4.4 Iodine content (by mass) and I_{I_5}/I_G ratio in Raman of I-rGO after dispersing in different solvents.

Material	Solvent	EDS (Mass pct.)			
		Carbon	Oxygen	Iodine	Nitrogen
I-rGO-S Vortex	DMF	75.92%	13.31%	9.33%	1.44%
	IPA	76.44%	14.04%	9.06%	/
	Cyclohexane	81.18%	11.83%	6.90%	/
I-rGO-S Sonication	DMF	76.43%	13.89%	8.44%	1.23%
	IPA	79.59%	13.10%	7.07%	/
	Cyclohexane	80.99%	12.04%	6.97%	/
I-rGO-NS Vortex	DMF	65.50%	13.66%	18.31%	3.02%
	IPA	66.67%	13.72%	19.56%	/
	Cyclohexane	68.16%	12.45%	18.93%	/
I-rGO-NS Sonication	DMF	68.62%	14.82%	14.74%	1.83%
	IPA	68.53%	13.95%	15.93%	/
	Cyclohexane	80.68%	8.02%	11.13%	/

4.4. Energetic application of I-rGO in I-rGO/Al/Bi_2O_3

Dispersions of I-rGO in DMF were next examined as the basis for the self-assembly of nanothermite composites. I-rGO-S was selected as the scaffold material onto which Al and Bi_2O_3 nanoparticles would self-assembly to form binary I-rGO-S/Al or ternary I-rGO-S/Al/Bi_2O_3 nanothermite composites. The energetic properties of these assembled materials were then examined. The I-rGO-S / DMF dispersions were mixed with Al / IPA and Bi_2O_3 / IPA dispersions and allowed to self-assemble in solution. The nanoparticles assembled onto the surface of the I-rGO sheets and precipitated within a few hours, leaving a clear supernatant.

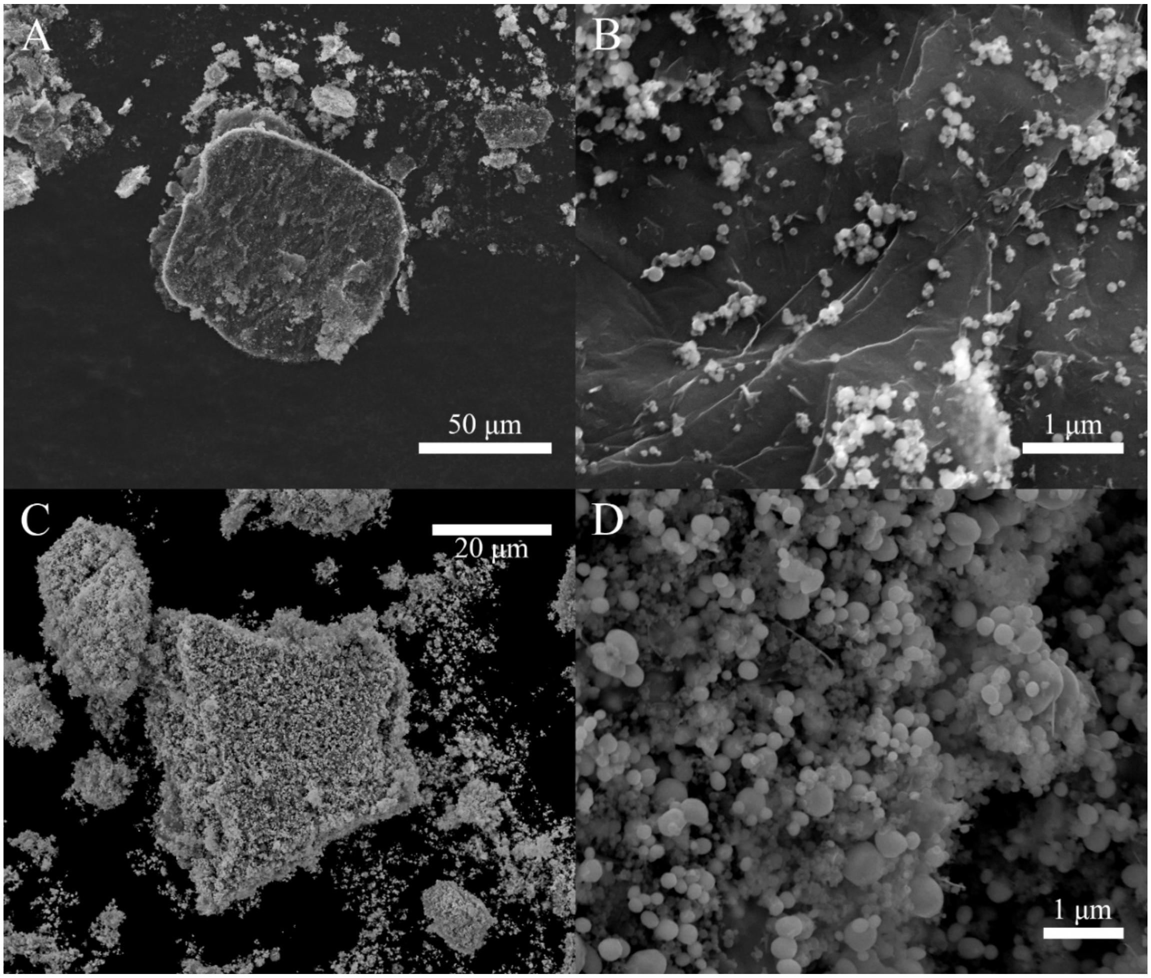

Figure 4.8 SEM pictures of I-rGO-S/Al (A, B) and I-rGO (7.5%)/Al/Bi_2O_3 (C, D).

SEM micrographs of the self-assembled I-rGO-S/Al and I-rGO-S/Al/Bi_2O_3 nanocomposites are shown in Figure 4.8. The dimensions of I-rGO was were on the order of a few microns to tens of microns after sonication, as seen from Figure 4.8A and Figure 4.8C. Al nanoparticles decorated onto the surface of dispersed I-rGO sheets with no significant agglomeration after self-assembly, as observed in Figure 4.8B. A similar result was found for the I-rGO-S/Al/Bi_2O_3 self-assembled structure, as shown in Figure 4.8C and D. Al and Bi_2O_3 nanoparticles were self-assembled on the surface of I-rGO sheets, leading to a homogeneous mixture between fuel and oxidizer of nanothermite with no phase separation. Decorated sheets then assembled layer-by-layer to form a dense structure of particle-decorated sheets, similar to the self-assembled GO/Al/Bi_2O_3 found in our previous work. [21]

DSC was used to measure the energy release of I-rGO-S/Al and I-rGO-S/Al/Bi_2O_3 self-assembled composites with varying mass percentages of I-rGO, as shown in Figure 4.9. A self-assembled GO/Al sample (containing no iodine) was used as a control. The GO/Al sample exhibited a small (26 J/g), extended exothermic peak from 450 to 600°C due to the reaction between the Al core and the decomposed -OH groups absorbed on the Al_2O_3. A small endothermic peak indicated Al melting occurred at 660°C. After melting, Al could readily flow and react with carbon and oxygen in the GO, resulting in an additional (90 J/g) exothermic reaction.

By contrast, the I-rGO-S/Al (70-30) sample (indicating 70% I-rGO by mass), produced a significant exothermic reaction (676 J/g) prior to Al melting, with a peak reaction temperature of ~585°C. The decomposed I-rGO released free iodine, which could then react with the alumina surface of Al nanoparticles, forming an Al-O-I bridge bond. [1] The Al-I-O bond modified the original alumina structure, creating a hollow or weakened area for the Al core to exit easily through the alumina shell before reaching its melting point. Note that no endothermic Al melting peak was observed for the I-rGO-S/Al (70/30) sample. When the I-rGO content was dominant (70% in mass), the Al core was almost all reacted with I-rGO before melting ($Al + O \rightarrow Al_2O_3, Al + I \rightarrow AlI_3$, oxygen and iodine indicate decomposed fragments from I-rGO), leaving a very small Al melting peak. A 676 J/g energy release, without any additional oxidizer was observed, indicating the alumina shell was sufficiently removed to allow Al to react with iodine species prior to melting. As the relative Al content increased, the iodine content in I-rGO was insufficient to remove the Al_2O_3 shell and react with Al core completely, and large Al melting endothermic peaks were observed for the I-rGO-S/Al 50/50 and 30/70 samples. Another exothermic peak was found after the melting of Al, indicating that melted Al reacted with the surrounding carbon in I-rGO.

The energy release from Al/Bi_2O_3 nanothermite composites was next examined. The equivalence ratio, Φ, between reactive Al and Bi_2O_3 in all samples was maintained at 1.6, calculated as

$$\Phi = \frac{[n(fuel)/n(oxidizer)]_{actual}}{[n(fuel)/n(oxidizer)]_{stoichiometry}}$$

where *n* represents the number of mols of fuel or oxidizer, the subscript “actual” represents the experimental value, and the subscript “stoichiometry” represents the ideal value for complete combustion. Only Bi_2O_3 was included as an oxidizer for calculations. Including iodine as an oxidizer would result in only a 0.01 change in the equivalence ratio, due to its low atomic fraction. The DSC curves of Al/Bi_2O_3 powder, $GO/Al/Bi_2O_3$ (5% GO in total mass) assembled composite, and I-rGO-S/Al/Bi_2O_3 (5%, 7.5%, 10% I-rGO in total mass) assembled composites are plotted in Figure 4.9B. For randomly mixed Al/Bi_2O_3 nanothermite powder, the reaction occurred between 510 and 715°C. The main reaction peaked at 615°C, and a total energy release was 735 J/g was observed. The self-assembled $GO/Al/Bi_2O_3$ structure produced an energy release of 1220 J/g, more than 65% higher than the randomly mixed Al/Bi_2O_3. As important, the initiation temperature of the exothermic reaction was reduced to ~470°C as a result of reduced phase separation and a decreased diffusion distance of the nanoparticles. A significant exothermic reaction occurred after the melting of Al in GO/Al/Bi_2O_3, however, indicating that some agglomeration of Al NPs still existed in the sample and remained unreacted until it could melt and flow in the material.

The I-rGO-S/Al/Bi_2O_3 composites produced a total exothermal energy from 1270 to 1326 J/g. While the total energy release is only slightly greater than that observed from GO/Al/Bi_2O_3 composites, the reaction profile with temperature is quite different. Most of the energy released from the I-rGO-S/Al/Bi_2O_3 composites (1234 – 1263 J/g) occurred between 400 – 660°C, with only a small energy release (36-63 J/g) occurring above 660°C. Therefore, most of the Al core reacted in the solid state. The initial reaction temperature for I-rGO-S/Al/Bi_2O_3 was 440°C, significantly lower than 470°C observed for GO/Al/Bi_2O_3 and 510°C for Al/Bi_2O_3. For all concentrations of I-rGO, a dominant exothermic peak was observed at 555°C, much lower than that for GO/Al/Bi_2O_3 and Al/Bi_2O_3. Our hypothesis is that this significant change in reaction temperature is attributed to the iodine reacting with and weakening the alumina shell of Al nanoparticles, thereby enabling the Al core to diffuse and react with the outside oxidizer at a relatively low temperature. In addition, an exothermic shoulder from 605 ~ 655°C was present in I-rGO(5%)/Al/Bi_2O_3, which was reduced for I-rGO(7.5%)/Al/Bi_2O_3 and absent for I-rGO(10%)/Al/Bi_2O_3. This finding indicated that the increased quantity of I-rGO in the composite more fully reacted with the Al_2O_3 shell at lower temperatures, enabling greater energy release at lower temperature. Further increasing the I-rGO in the composite past 10% would generate unnecessary dead mass in the material; therefore, 5~10% I-rGO in I-rGO-

$S/Al/Bi_2O_3$ is sufficient to provide a robust self-assembly template, while supplying sufficient reactive iodine to facilitate full reaction with the alumina shell.

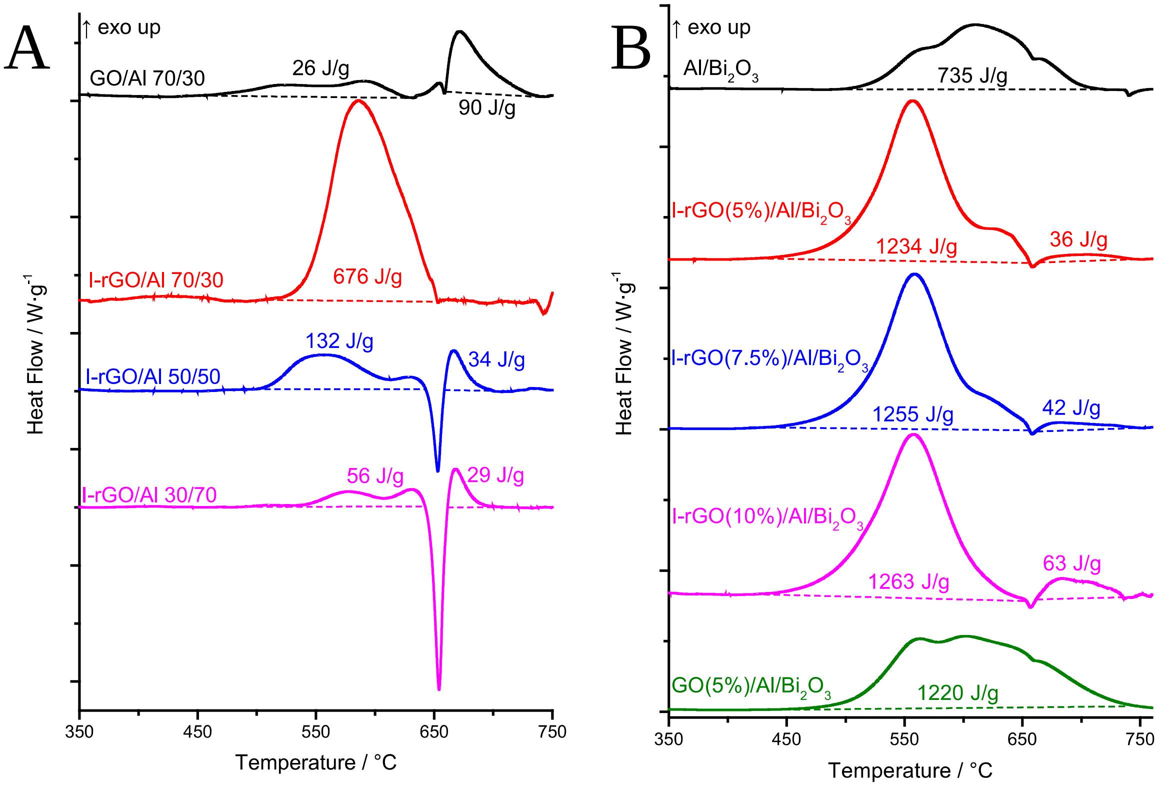

Figure 4.9 DSC curves of I-rGO-S/Al compared to GO/Al (A), and I-rGO-S/Al/ Bi_2O_3 compared to Al/ Bi_2O_3 and GO/Al/ Bi_2O_3 (B).

Considering the superior electrical conductivity of the I-rGO, it is expected that the self-assembled I-rGO/Al/Bi_2O_3 also exhibited better resistance to electrical static discharge. It was measured that the I-rGO(7.5%)/Al/Bi_2O_3 had an ignition threshold of 1.00 mJ, which is 3 orders higher than neat Al/Bi_2O_3 [32] and even slightly higher than the freeze-dried rGO/Al/Bi_2O_3 gel as described in chapter 2. In rGO/Al/Bi_2O_3 gel, the rGO was not well reduced, with a C/O atomic ratio ~2.74, and had 5% in the total mass of the gel. However, here in I-rGO/Al/Bi_2O_3, the C/O ratio was at ~7.40, and had 7.5% in the total mass, providing a better conductivity throughout the sample even without the gel structure. Therefore, I-rGO/Al/Bi_2O_3 exhibited better ESD resistance.

4.5. Comparison between FGO and I-rGO in functionalized graphene/Al/Bi_2O_3 nanoenergetic composite

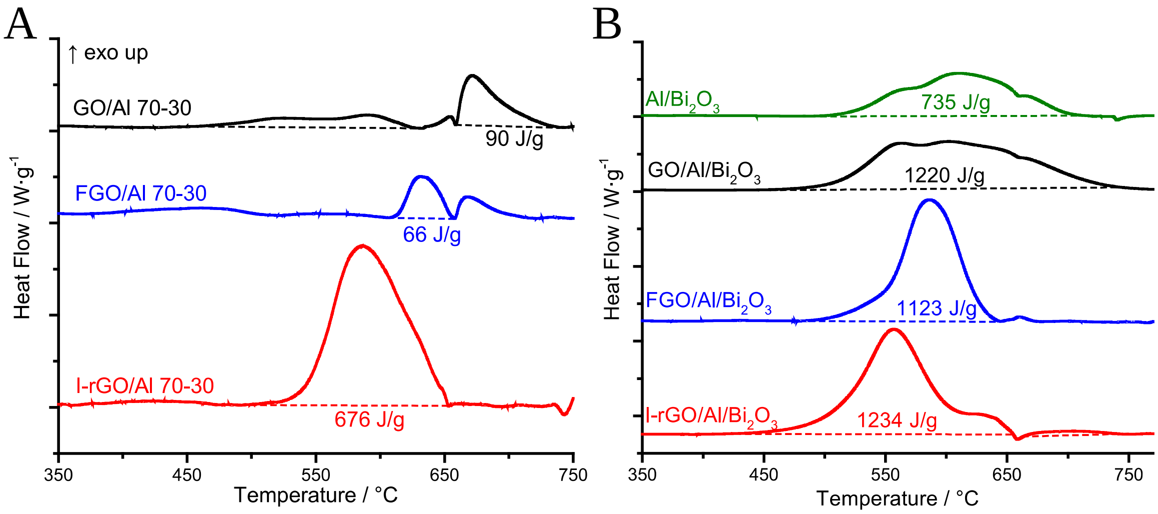

Figure 4.10 DSC results of GO/Al, FGO/Al, I-rGO/Al at 70/30 mass ratio (A), and Al/Bi_2O_3, GO(5%)/Al/Bi_2O_3, FGO(5%)/Al/Bi_2O_3, I-rGO(5%)/Al/Bi_2O_3 (B).

Table 4.5 Summarization of reaction results of I-rGO and FGO in nanoenergetic materials. Functionalized graphene materials (GO, FGO, I-rGO) occupied 5% of total mass of nanoenergetic composites are compared. The temperatures are referred to the main exothermic reaction.

Material	Onset temperature	Peak temperature	Termination temperature	Energy release
GO/Al (70-30)	660°C	670°C	730°C	90 J/g
FGO/Al (70-30)	610°C	635°C	655°C	66 J/g
I-rGO-S/Al (70-30)	520°C	585°C	655°C	676 J/g
Al/Bi_2O_3	510°C	615°C	715°C	735 J/g

GO(5%)/Al/Bi_2O_3	470°C	600°C	740°C	1220 J/g
FGO(5%)/Al/Bi_2O_3	490°C	586°C	645°C	1123 J/g
I-rGO(5%)/Al/Bi_2O_3	440°C	555°C	655°C	1234 J/g

Both iodinated reduced graphene oxide and fluorinated graphene oxide reduced the onset and peak reaction temperatures when mixed with Al or when applied as additive in Al/Bi_2O_3 nanothermite. The DSC results of all samples are also shown in Figure 4.10. However, there are some critical differences between FGO and I-rGO, as shown in Table 4.5.

As discussed above, in traditional Al/Bi_2O_3 loose powder and self-assembled GO/Al/Bi_2O_3, the energetic reaction continued until 715°C and 740°C, much higher than the melting temperature of Al. It revealed that part of the Al core remained unreacted when melting, probably protected by the alumina shell. However, in FGO/Al/Bi_2O_3 and I-rGO/Al/Bi_2O_3, the main reaction terminated before the melting of Al, indicating most Al was already reacted before reaching Al melting temperature. Therefore, the addition of halogen elements in graphene weakened the alumina shell by the reactions shown in Figure 4.11. The self-assembled structure in FGO/Al/Bi_2O_3 and I-rGO/Al/Bi_2O_3 also resulted in significantly enhanced energetic release, similar to GO/Al/Bi_2O_3, due in part to the reduced phase separation and diffusion length.

It is commonly recognized that fluorine is more electronegative than iodine. However, the reaction initiation temperature of FGO/Al was 90°C higher than I-rGO-S/Al, and the energy release of FGO/Al was less than 10% that of I-rGO-S/Al. These differences are attributed to variations in the quantity of halogen atoms within the two structures and to the differences in bonding between FGO and I-rGO structures. I-rGO-S retained a majority of its iodine species after ultrasonic dispersion in DMF solvent, whereas most fluorine functional groups, such as acyl fluoride groups, decomposed in solvent during the FGO sonication process. Further, I-rGO-S released iodine throughout the DSC heating process and a large portion of iodine was released between 400 to 800°C, whereas more than 95% of fluorine in FGO was lost before reaching 450°C.

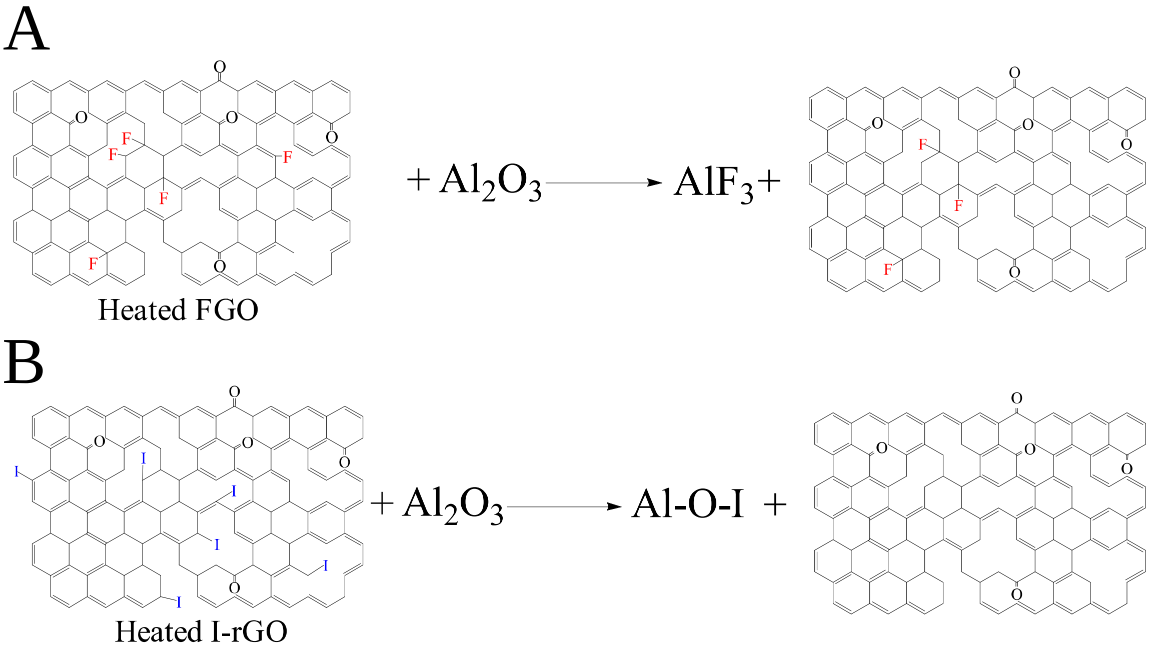

Figure 4.11 Reactions of alumina shell removal in FGO/Al, FGO/Al/Bi2O3 (A) and I-rGO/Al, I-rGO/Al/Bi2O3 (B). Fluorine in FGO was stably bonded as C-F covalent and semi-ionic bond, which could not be released easily during heating, while the week C-I bond in I-rGO enabled iodine to release easily from the structure. The reaction is not balanced.

For assembled I-rGO-S/Al and I-rGO-S/Al/Bi_2O_3 composites, iodine was released throughout the DSC heating process and weakened the alumina shell. However, after assembly and heating, the remaining fluorine in FGO/Al and FGO/Al/Bi_2O_3 was most likely contained in stable covalent and semi-ionic C-F bonds [30] and could not easily react with the alumina shell, as shown in Figure 4.11. Because of the reduced abundance of fluorine and the chemical stability of the fluorine within the FGO, the reaction in FGO/Al and FGO/Al/Bi_2O_3 initiated at a higher temperature than similar I-rGO composites. The presence of either halogen in an assembled Al/Bi_2O_3 composite was sufficient to well react the Al fuel in its solid state.

4.6. Conclusion and future direction

Iodinated reduced graphene oxide (I-rGO) was synthesized and applied as a self-assembly template with Al and Bi_2O_3 nanoparticles. I-rGO was synthesized by direct reduction of GO using both H_3PO_2 stabilized and non-stabilized hydroiodic acid (HI). The products contained distinctly different iodine species by using different HI. I-rGO-S (produced by stabilized HI) contained a lower amount of iodine, mostly in the form of single iodine atoms, while I-rGO-NS (produced by non-stabilized HI) contained a greater specific mass of iodine in the form of atomic iodine and polyiodides. The polyiodides in I-rGO were less stable than atomic iodine in I-rGO under heating and exfoliating of graphene layers in organic solvents. The ability to disperse and exfoliate I-rGO papers in different solvents was positively correlated with the mass loss of iodine during sonication. Nevertheless, I-rGO was successfully utilized as a scaffold for the solution-based self-assembly of I-rGO/Al and I-rGO/Al/Bi_2O_3 composites. In addition, the I-rGO/Al provided reactive iodine species which reacted with and weakened the alumina shell surrounding Al NP fuel at low temperatures. DSC results showed that significant exothermic reaction is possible by heating I-rGO/Al without additional oxidizer. Furthermore, the I-rGO/Al/Bi_2O_3 self-assembled composite exhibited a 70% greater energy release than randomly mixed Al/Bi_2O_3 powder due to the ordered structure and reduced diffusion distance induced by the high-density NP assembly on the I-rGO surface. More importantly, the reactive iodine species provided by the I-rGO scaffold at low temperature, reacted with the inert alumina shell of Al nanoparticles, significantly reducing the temperature of the of I-rGO/Al/Bi_2O_3 energetic reaction compared to self-assembled GO/Al/Bi_2O_3.

The release of iodine species in terms of biocidal applications was not specifically examined here. Future work may investigate synthesizing the nanoenergetic material with even higher iodine percentage to evaluate capability of the iodine byproducts as a biocidal agent during the combustive energetic reaction. Additionally, other methods for synthesizing iodinated graphene, such as hydrothermal process and I_2 iodination process, can also be taken into consideration.

4.7. Summary

This part of research focuses on the iodination of graphene and its applications in self-assembly with energetic nanoparticles. Researchers have conducted some research on the properties of iodinated graphene, while no study was conducted on its stability nor using that material for nanoenergetic applications. The research is meaningful to better understand the properties of iodine species in graphene structure. The most significant difficulty I had during researching this material was the loss of iodine during sonication before the assembly with nanoparticles. The I-rGO was synthesized directly from large pieces of GO sheets, while the large piece of the I-rGO sheets could not be dispersed into solvents easily. It was improved by cutting the large I-rGO sheets into small pieces, which significantly accelerated the dispersing process of I-rGO in solvent. This I-rGO is far from a “perfect” material to be applied in nanoenergetic material. Its iodine content is low, and its loss of iodine is severe during the sonication and assembly. More and better iodination process will be developed and be used for better iodinated graphene – nanoenergetic composites.

Other than nanoenergetics, the self-assembled nanocomposites formed by iodinated graphene and different nanoparticles may be used in different applications, such as for electrodes and catalysts.

4.8. References

[1] O. Mulamba and M. Pantoya, "Exothermic surface reactions in alumina–aluminum shell–core nanoparticles with iodine oxide decomposition fragments," *Journal of Nanoparticle Research,* journal article vol. 16, no. 3, p. 2310, February 22 2014.

[2] C. W. Farley, M. L. Pantoya, M. Losada, and S. Chaudhuri, "Linking molecular level chemistry to macroscopic combustion behavior for nano-energetic materials with halogen containing oxides," *The Journal of Chemical Physics,* vol. 139, no. 7, p. 074701, 2013.

[3] T. Wu, X. Wang, P. Y. Zavalij, J. B. DeLisio, H. Wang, and M. R. Zachariah, "Performance of iodine oxides/iodic acids as oxidizers in thermite systems," *Combustion and Flame,* vol. 191, pp. 335-342, 2018/05/01/ 2018.

[4] T. Wu, X. Wang, J. B. DeLisio, S. Holdren, and M. R. Zachariah, "Carbon addition lowers initiation and iodine release temperatures from iodine oxide-based biocidal energetic materials," *Carbon,* vol. 130, pp. 410-415, 2018/04/01/ 2018.

[5] K. S. Martirosyan, L. Wang, and D. Luss, "Development of nanoenergetic materials based on Al/I2O5 system," *Nanotech,* vol. 2, p. 4, 2010.

[6] D. K. Smith, M. L. Pantoya, J. S. Parkey, and M. Kesmez, "Reaction Kinetics and Combustion Dynamics of I(4)O(9)and Aluminum Mixtures," *Journal of Visualized Experiments : JoVE,* no. 117, p. 54661, 11/07 2016.

[7] T. Wu, A. SyBing, X. Wang, and M. R. Zachariah, "Aerosol synthesis of phase pure iodine/iodic biocide microparticles," *Journal of Materials Research,* vol. 32, no. 4, pp. 890-896, 2017.

[8] C. He, J. Zhang, and J. n. M. Shreeve, "Dense Iodine-Rich Compounds with Low Detonation Pressures as Biocidal Agents," *Chemistry – A European Journal,* vol. 19, no. 23, pp. 7503-7509, 2013/06/03 2013.

[9] B. R. Clark and M. L. Pantoya, "The aluminium and iodine pentoxide reaction for the destruction of spore forming bacteria," *Physical Chemistry Chemical Physics,* 10.1039/C0CP00473A vol. 12, no. 39, pp. 12653-12657, 2010.

[10] H. Wang, J. B. DeLisio, G. Jian, W. Zhou, and M. R. Zachariah, "Electrospray formation and combustion characteristics of iodine-containing Al/CuO nanothermite microparticles," *Combustion and Flame,* vol. 162, no. 7, pp. 2823-2829, 2015/07/01/ 2015.

[11] Y. Aly *et al.*, "Iodine-containing aluminum-based fuels for inactivation of bioaerosols," *Combustion and Flame,* vol. 161, no. 1, pp. 303-310, 2014/01/01/ 2014.

[12] Z. Yao, H. Nie, Z. Yang, X. Zhou, Z. Liu, and S. Huang, "Catalyst-free synthesis of iodine-doped graphenevia a facile thermal annealing process and its use for electrocatalytic oxygen reduction in an alkaline medium," *Chemical Communications,* 10.1039/C2CC16192C vol. 48, no. 7, pp. 1027-1029, 2012.

[13] Y. Zhan *et al.*, "Iodine doped graphene as anode material for lithium ion battery," *Carbon,* vol. 94, pp. 1-8, 2015/11/01/ 2015.

[14] Z. Wang, W. Wang, M. Wang, X. Meng, and J. Li, "P-type reduced graphene oxide membranes induced by iodine doping," *Journal of Materials Science,* vol. 48, no. 5, pp. 2284-2289, 2013/03/01 2013.

[15] W. Feng, P. Long, Y. Feng, and Y. Li, "Two-Dimensional Fluorinated Graphene: Synthesis, Structures, Properties and Applications," *Advanced Science,* vol. 3, no. 7, p. 1500413, 2016/07/01 2016.

[16] P. Simek, K. Klimova, D. Sedmidubsky, O. Jankovsky, M. Pumera, and Z. Sofer, "Towards graphene iodide: iodination of graphite oxide," *Nanoscale,* 10.1039/C4NR05219F vol. 7, no. 1, pp. 261-270, 2015.

[17] S. Some *et al.*, "Graphene-Iodine Nanocomposites: Highly Potent Bacterial Inhibitors that are Bio-compatible with Human Cells," *Scientific Reports,* Article vol. 6, p. 20015, 02/04/online 2016.

[18] S. Pei, J. Zhao, J. Du, W. Ren, and H.-M. Cheng, "Direct reduction of graphene oxide films into highly conductive and flexible graphene films by hydrohalic acids," *Carbon,* vol. 48, no. 15, pp. 4466-4474, 2010/12/01/ 2010.

[19] P. H. Ling, Š. Petr, S. Zdeněk, and P. Martin, "Halogenation of Graphene with Chlorine, Bromine, or Iodine by Exfoliation in a Halogen Atmosphere," *Chemistry – A European Journal,* vol. 19, no. 8, pp. 2655-2662, 2013.

[20] N. Ye, Y. Xie, P. Shi, T. Gao, and J. Ma, "Synthesis of magnetite/graphene oxide/chitosan composite and its application for protein adsorption," *Materials Science and Engineering: C,* vol. 45, pp. 8-14, 2014/12/01/ 2014.

[21] R. Thiruvengadathan *et al.*, "A Versatile Self-Assembly Approach toward High Performance Nanoenergetic Composite Using Functionalized Graphene," *Langmuir,* vol. 30, no. 22, pp. 6556-6564, Jun 2014.

[22] N. Soin, S. S. Roy, C. O'Kane, J. A. D. McLaughlin, T. H. Lim, and C. J. D. Hetherington, "Exploring the fundamental effects of deposition time on the microstructure of graphene nanoflakes by Raman scattering and X-ray diffraction," *CrystEngComm,* 10.1039/C0CE00285B vol. 13, no. 1, pp. 312-318, 2011.

[23] G. Kalita, K. Wakita, M. Takahashi, and M. Umeno, "Iodine doping in solid precursor-based CVD growth graphene film," *Journal of Materials Chemistry,* 10.1039/C1JM13268G vol. 21, no. 39, pp. 15209-15213, 2011.

[24] R. A. Hoyt, E. M. Remillard, E. D. Cubuk, C. D. Vecitis, and E. Kaxiras, "Polyiodide-Doped Graphene," *The Journal of Physical Chemistry C,* vol. 121, no. 1, pp. 609-615, 2017/01/12 2017.

[25] N. Jung, A. C. Crowther, N. Kim, P. Kim, and L. Brus, "Raman Enhancement on Graphene: Adsorbed and Intercalated Molecular Species," *ACS Nano,* vol. 4, no. 11, pp. 7005-7013, 2010/11/23 2010.

[26] G. Lalwani, J. L. Sundararaj, K. Schaefer, T. Button, and B. Sitharaman, "Synthesis, characterization, in vitro phantom imaging, and cytotoxicity of a novel graphene-based multimodal magnetic resonance imaging-X-ray computed tomography contrast agent," *Journal of Materials Chemistry B,* 10.1039/C4TB00326H vol. 2, no. 22, pp. 3519-3530, 2014.

[27] D. Tristant, P. Puech, and I. C. Gerber, "Theoretical study of polyiodide formation and stability on monolayer and bilayer graphene," *Physical Chemistry Chemical Physics,* 10.1039/C5CP04594K vol. 17, no. 44, pp. 30045-30051, 2015.

[28] S. Park, J. An, J. R. Potts, A. Velamakanni, S. Murali, and R. S. Ruoff, "Hydrazine-reduction of graphite- and graphene oxide," *Carbon,* vol. 49, no. 9, pp. 3019-3023, 2011/08/01/ 2011.

[29] M. P. Araújo, O. S. G. P. Soares, A. J. S. Fernandes, M. F. R. Pereira, and C. Freire, "Tuning the surface chemistry of graphene flakes: new strategies for selective oxidation," *RSC Advances,* 10.1039/C6RA28868E vol. 7, no. 23, pp. 14290-14301, 2017.

[30] A. Wang *et al.*, "Synthesis, characterization and nanoenergetic utilizations of fluorine, oxygen co-functionalized graphene by one-step XeF2 exposure," *Combustion and Flame,* vol. 215, pp. 324-332, 2020/05/01/ 2020.

[31] J. Dai, G. Wang, L. Ma, and C. Wu, "Study on the surface energies and dispersibility of graphene oxide and its derivatives," *Journal of Materials Science,* vol. 50, no. 11, pp. 3895-3907, 2015/06/01 2015.

[32] J. A. Puszynski, C. J. Bulian, and J. J. Swiatkiewicz, "Processing and Ignition Characteristics of Aluminum-Bismuth Trioxide Nanothermite System," *Journal of Propulsion and Power,* vol. 23, no. 4, pp. 698-706, 2007/07/01 2007.

Chapter 5 Conclusions

5.1. Conclusions

Different types of functional graphene were synthesized and utilized in self-assembled functional graphene/Al/Bi_2O_3 nanoenergetic materials.

Table 5.1 Summary of different functionalized graphene assisted self-assembled nanoenergetic material towards the critical problems of nanothermite. (√ stands for problem solved, × stands for problem not solved, ? stands for not confirmed from current results)

Material	Phase separation	Al reactive sintering	Scalability / ESD sensitivity	Inert Al_2O_3 shell
rGO/Al/Bi_2O_3 gel	√	√	√	×
FGO/Al/Bi_2O_3	?	?	×	√
I-rGO/Al/Bi_2O_3	√	√	√	√

The novel gelation process of rGO in PC by using EDA as reducer and gelling agent provided a perfect platform for Al and Bi_2O_3 to form macroscale structure without loss of, but with increased energetic performance. The well-dispersed mixture and folded rGO sheets formed during synthesis prevented the phase separation and agglomeration of same nanoparticles but formed well-ordered clusters of reactive nanothermite mixture in microscale. The multi-functional 2D assembly scaffolds provide a means to boost the energy density and decrease the temperature of peak reaction for nanothermite materials. Not only was the magnitude of energy release from isothermal reaction enhanced, but the linear combustion propagation speed was also doubled due to the distinct confined and porous structure, which differentiates this rGO/Al/Bi_2O_3 aerogel from other macroscale energetic mixtures. The highly conductive scaffold improved the ESD threshold for igniting this energetic material. This process is suitable for synthesizing macro-sized and large-scale energetic gel, and for safely handling and storage.

Two different types of halogenated graphene, fluorinated graphene oxide and iodinated reduced graphene oxide, were synthesized, studied in terms of their stability, and utilized in energetic material. Fluorinated graphene oxide was produced by direct XeF_2 gas fluorination graphene oxide sheets, which contained both fluorine and oxygen functional groups. FGO was found to degrade slowly in atmosphere due to its unstable functional groups such as acyl fluoride. It also reacts with the suspension agent and lose significant amount of fluorine groups during dispersing and preparing energetic materials. However, the remained covalently and semi-ionically bonded fluorine in C-F bonds survived in the synthesis method and provided enough active fluorine to weaken the alumina shell during the energetic reaction, lowering the main reaction temperature and make it an all-solid-state reaction. I-rGO contained iodine in different forms, determined by the HI used for synthesis. Polyiodides were found to be unstable while single atom iodine bonded to graphene lattice was stable after sonication and assembly with nanoenergetic particles. The released iodine also helped to weaken the alumina shell of Al nanoparticles and reduce the reaction temperature of the nanoenergetic composite. Both FGO and I-rGO assisted self-assembled functionalized graphene/Al/Bi_2O_3 appeared over 50% more energy release than neat Al/Bi_2O_3 powder. However, compared to the stronger C-F bond in FGO/Al/Bi_2O_3, the weaker C-I bond in I-rGO/Al/Bi_2O_3 enabled a better release of halogen during the heating process and a better weakening of the alumina shell. More importantly, the outstanding electrical conductivity of I-rGO increased the threshold of electrostatic discharge ignition energy for I-rGO/Al/Bi_2O_3, which made it more suitable for safely handling and storage of nanothermite material and could provide outstanding energy release.

5.2. Future Expectations

There are multiple further researches that can be taken for all these three different kinds of materials and other types of functionalized graphene or 2D materials.

Oxidizers with different formula and nanoscale morphologies can be applied in the gel to understand the relative mechanical and energetic characteristics. The synthesis method was flexible so that different needs can be met. Additionally, 3D printing of the aerogel can be developed to form a printable energetic structure with designable shape and size.

Fluorinated graphene can be considered to be synthesized from different methods. Ideally, a stable oxygen, fluorine co-functionalized graphene with good stability and ability to exfoliate and disperse in organic suspension agent will be the perfect candidate for nanoenergetic applications. It might be approached by using F_2 gas as the fluorination agent, but with proper and sufficient protection. The hydrothermal and XeF_2/commercial graphene can also be optimized to produce good self-assembly substrate for nanoenergetic particles since I-rGO proved that reduced graphene oxide is also suitable to play this role.

Further research of iodinated reduced graphene oxide with Al nanothermite can be focused on its application as biocidal material. Compared to using iodine oxides and oxidizer, using iodinated graphene provides much better ESD safety, and more control in iodine amount. The cost of using I-rGO was also lower due to the low I-rGO usage and flexibility in choice of metal oxide.

The flexible functionalization of graphene may also enable further applications beyond the materials mentioned in this dissertation. Chlorinated or brominated graphene, or iodine, oxide co-functionalized graphene may also be used as additive in nanothermite mixtures to help remove the alumina shell of Al nanoparticles. Furthermore, halogenated macroscale functionalized graphene/Al/MO_x aerogel may be designed and synthesized to overcome all problems at the same time.

Different types of materials, especially 2D or 3D materials, may also be considered into the self-assembly of nanoenergetic materials. These materials can either be the oxidizer itself or additive. The ideal material in the desired self-assembled nanoenergetic material should help to remove the alumina shell and provide a conductive scaffold. For example, some conductive metal oxyfluoride materials have been developed and may be used as the oxidizer, which may help to solve both the problem of alumina shell and scalability at the same time.

Self-assembly is probably the most promising method of the bottom-up fabrication process from nanomaterials to large devices. The self-assembly process can be driven by electrostatic force, hydrogen bonding, π-π interactions, Van der Waals interactions, or even chemical reaction, leading to the formation of an ordered structure with cycled building blocks. Scientists have yet been able to fully understand and build up the complete mechanism map of self-assembly, but it is definitely worthy for researchers to devote themselves in this field to develop more functional materials for numerous exciting applications.

Publications and Presentations

Journal publications

1. **Reactive nanoenergetic graphene aerogel synthesized by one-step chemical reduction**

Anqi Wang, Sangho Bok, Rajagopalan Thiruvengadathan, Keshab Gangopadhyay, Jacob A McFarland, Matthew R Maschmann, Shubhra Gangopadhyay
Combustion and Flame, **2018**, Volume 196, 400-406.

2. **Synthesis, characterization and nanoenergetic utilizations of fluorine, oxygen co-functionalized graphene by one-step XeF2 exposure**

Anqi Wang, Sangho Bok, Cherian Joseph Mathai, Rajagopalan Thiruvengadathan, Charles M Darr, H Chen, Michael R Zachariah, Keshab Gangopadhyay, Jacob A McFarland, Matthew R Maschmann, Shubhra Gangopadhyay
Combustion and Flame, **2020**, Volume 215, 324-332.

3. **On the stability study of iodinated reduced graphene oxide and its application in self-assembled nanothermite composites** (under review)

Anqi Wang, Sangho Bok, Cherian Joseph Mathai, Keshab Gangopadhyay, Jacob A McFarland, Matthew R Maschmann, Shubhra Gangopadhyay
ACS Applied Materials and Interfaces, under review.

4. **Combustion of aluminum nanoparticles and exfoliated 2D molybdenum trioxide composites**

Naadaa Zakiyyan, Anqi Wang, Rajagopalan Thiruvengadathan, Clay Staley, Joseph Mathai, Keshab Gangopadhyay, Matthew R Maschmann, Shubhra Gangopadhyay
Combustion and Flame, **2018**, Volume 187, 1-10.

Conference presentations

1. Synthesis and characterization of a 3D-macroscale RGO/Al/Bi_2O_3 nanoenergetic organogel (Oral Personally)

Anqi Wang, Sangho Bok, Rajagopalan Thiruvengadathan, Cherian Joseph Mathai, Syed Barizuddin, Keshab Gangopadhyay, Matthew M. Maschmann, Shubhra Gangopadhyay
MRS Fall meeting 2017, Boston, MA.

VITA

Anqi Wang was born on May 15, 1991 in Suzhou, Jiangsu Province, China. He graduated from Suzhou high school in 2009 and enrolled in chemistry at Nanjing University. He graduated with a BS of science in chemistry in 2013. In 2016, he started the PhD program under the advisement of Dr. Shubhra Gangopadhyay. His research interests focus on the synthesis, characterization, and applications of self-assembled composites of functionalized graphene and nanoenergetic materials.